

Rik Lodevicus Elizabeth Maria Ubaghs

# **Exploring neurovascular coupling through simultaneous functional Magnetic Resonance Imaging and microscopy**





Diss. ETH No. 29359

# **Exploring neurovascular coupling through simultaneous functional Magnetic Resonance Imaging and microscopy**

A dissertation submitted to attain the degree of

DOCTOR OF SCIENCES of ETH ZURICH

(Dr. sc. ETH Zurich)

presented by

Rik Lodevicus Elizabeth Maria Ubaghs

M.Sc., University of Amsterdam

born on 08.11.1990, citizen of the Netherlands

accepted on the recommendation of

Prof. Dr. Benjamin Grewe, examiner

Prof. Dr. Mehmet Fatih Yanik, co-examiner

Prof. Dr. Valerio Zerbi, co-examiner

Prof. Dr. Daniel Razansky, co-examiner

2023

Rik Lodevicus Elizabeth Maria Ubaghs: *Exploring neurovascular coupling through simultaneous functional Magnetic Resonance Imaging and microscopy*, © 2023

doi: 10.3929/ethz-b-000627509



## Abstract

Functional Magnetic Resonance Imaging (fMRI) promises a way to non-invasively measure brain activity with an unprecedented spatial coverage and resolution. However, the most widely used fMRI contrasts, such as the Blood Oxygen Level Dependent (BOLD) signal, measures the local hemodynamic response as a proxy for neural activity. The exact relationship between local neural activity and hemodynamics remains a topic of discussion due to the complex interactions involved in the coupling between neurons and the vasculature. To gain a more comprehensive understanding of the neurovascular relationship, we designed a novel experimental paradigm that allows us to measure simultaneous microscopic single-neuron calcium activity and BOLD fMRI in awake animals.

Through the use of combined microscope fMRI, we were able to observe the calcium activity of layer 2/3 neurons in the somatosensory barrel fields (SSp-bfd) during whisker stimulation, while concurrently acquiring the whole brain BOLD fMRI signal. The simultaneous recordings allowed us to explore the activity of the brain across spatial scales. First, we examined the interaction between individual cells in the SSp-bfd and the local BOLD fMRI response. We used the spatial component of the microscope recordings to determine the relative distance between the neurons and the vascular structure, and examined whether the proximity between neurons and the vasculature was related to the hemodynamic response. Using a linear regression based decoding approach, we found two distinct populations of cells that were different in their location and activity pattern.

Second, we leveraged the spatial coverage of whole brain BOLD fMRI to relate the activity from anatomically defined regions involved in whisking behavior to the local neural activity in the SSp-bfd. We used a linear regression based decoding approach to determine the degree of information contained within different brain regions about the local neural population. Our results demonstrate that different areas hold different levels of information relevant to the local neural activity in the SSp-bfd. In addition, we showed that properties of the whisker system, such as laterality and connectivity, could be reconstructed through the combined microscope fMRI approach.

Collectively, these results provide robust empirical evidence for the application of combined microscope fMRI in probing cross-scale brain activity. Furthermore, the experiments presented in this thesis highlights the benefit of incorporating complementary neuroimaging methods to improve our understanding of brain functions across scales.

Keywords: Microscopy, Calcium imaging, functional Magnetic Resonance Imaging, Blood-Oxygen Level Dependent signal, Neurovascular coupling, Microscope fMRI.

## Zusammenfassung

Das funktionelle Magnetic Resonance Imaging (fMRI) verspricht einen Weg zur nicht-invasiven Messung der Gehirnaktivität mit einer bisher unerreichten räumlichen Abdeckung und Auflösung. Die am häufigsten verwendeten fMRI Kontraste, wie zum Beispiel das Blood Oxygen Level Dependent (BOLD) Signal, messen jedoch die lokale hämodynamische Reaktion als Proxy für die neuronale Aktivität. Die genaue Beziehung zwischen der lokalen neuronalen Aktivität und der Hämodynamik bleibt aufgrund der komplexen Wechselwirkungen, die bei der Kopplung zwischen Neuronen und Blutgefäßen auftreten, ein Diskussionsthema. Um ein umfassenderes Verständnis der neurovaskulären Beziehung zu erlangen, haben wir ein neues experimentelles Paradigma entwickelt, das die gleichzeitige Erfassung der mikroskopischen Kalzium Aktivität einzelner Neuronen und der BOLD fMRI bei wachen Tieren ermöglicht.

Durch den Einsatz von kombinierter mikroskopischer fMRI konnten wir die Kalzium Aktivität von Neuronen der Schicht 2/3 in den somatosensorischen Barrel-Feldern (SSp-bfd) während der Stimulation mit dem Schnurrhaar beobachten und gleichzeitig das BOLD fMRI-Signal des gesamten Gehirns erfassen. Die simultanen Aufzeichnungen ermöglichten es uns, die Aktivität des Gehirns über räumliche Skalen hinweg zu untersuchen. Zunächst untersuchten wir die Interaktion zwischen einzelnen Zellen im SSp-bfd und der lokalen BOLD fMRI Reaktion. Wir nutzten die räumliche Komponente der Mikroskopaufnahmen, um den relativen Abstand zwischen den Neuronen und der vaskulären Struktur zu bestimmen, und untersuchten, ob die Nähe zwischen den Neuronen und der Vaskulatur mit der hämodynamischen Reaktion zusammenhängt. Mithilfe eines auf linearer Regression basierenden Dekodierung Ansatzes haben wir zwei unterschiedliche Zellpopulationen gefunden, die sich in ihrer Lage und ihrem Aktivitätsmuster unterscheiden.

Zweitens nutzten wir die räumliche Abdeckung der BOLD fMRI des gesamten Gehirns, um die Aktivität von anatomisch definierten Regionen, die am Schnurrhaar-Verhalten beteiligt sind, mit der lokalen neuronalen Aktivität im SSp-bfd in Beziehung zu setzen. Wir verwenden einen auf linearer Regression basierenden Dekodierung Ansatz, um den Informationsgehalt der verschiedenen Gehirnregionen über die lokale neuronale Population zu bestimmen. Unsere Ergebnisse zeigen, dass verschiedene Regionen unterschiedliche Informationsmengen über die lokale neuronale Aktivität im SSp-bfd enthalten. Darüber hinaus konnten wir zeigen, dass Eigenschaften des Schnurrhaar-Systems, wie die Lateralität und Konnektivität, durch den kombinierten Mikroskop fMRI Ansatz rekonstruiert werden können.



Insgesamt liefern diese Ergebnisse robuste empirische Beweise für die Anwendung von kombinierten Mikroskop fMRI bei der Untersuchung von skalenübergreifender Hirnaktivität. Darüber hinaus unterstreichen die in dieser Arbeit vorgestellten Experimente den Nutzen der Einbeziehung komplementärer Neuroimaging-Methoden, um unser Verständnis von skalenübergreifenden Hirnfunktionen zu verbessern.

Schlüsselwörter: Mikroskopie, Kalzium-Imaging, funktionelle Magnetic Resonance Imaging, Blood-Oxygen Level Dependent Signal, neurovaskuläre Kopplung, Mikroskop fMRI.

## Samenvatting

Functionele Magnetische Resonantie Beeldvorming (fMRI) belooft een manier om de hersenactiviteit non-invasief te meten met een ongekeerde ruimtelijke dekking en resolutie. De meest gebruikte fMRI-contrasten, zoals het Blood-Oxygen Level Dependent (BOLD) signaal, meten echter de lokale hemodynamische respons als een proxy voor neuronale activiteit. De exacte relatie tussen lokale neuronale activiteit en hemodynamica blijft een onderwerp van discussie vanwege de complexe interacties die betrokken zijn bij de koppeling tussen neuronen en de bloedvaten. Om een beter begrip van de neurovasculaire relatie te verkrijgen, hebben we een nieuw experimenteel paradigma ontworpen dat ons in staat stelt om gelijktijdige microscopische calcium activiteit van individuele neuronen en BOLD fMRI te meten in wakkere dieren.

Door het gebruik van gecombineerde microscoop-fMRI konden we de calcium activiteit van laag 2/3 neuronen in de somatosensorische gebied (SSp-bfd) tijdens snorharen stimulatie observeren, terwijl we tegelijkertijd het BOLD fMRI signaal van de hele hersenen vastlegden. De gelijktijdige opnames stelden ons in staat om de activiteit van de hersenen op verschillende spatiale niveaus te verkennen. Eerst onderzochten we de interactie tussen individuele cellen in de SSp-bfd en de lokale BOLD fMRI respons. We gebruikten de ruimtelijke component van de microscoop opnames om de relatieve afstand tussen de neuronen en de vasculaire structuur te bepalen, en onderzochten of de nabijheid tussen neuronen en de bloedvaten verband hield met de hemodynamische respons. Met behulp van een op lineaire regressie gebaseerde decodering methode vonden we twee verschillende populaties cellen die verschillen in hun locatie en activiteitenpatroon.

Ten tweede maakten we gebruik van de ruimtelijke dekking van de BOLD-fMRI metingen om de activiteit van anatomisch gedefinieerde gebieden die betrokken zijn bij snorharen stimulatie te relateren aan de lokale neuronale activiteit in de SSp-bfd. We gebruikten een op lineaire regressie gebaseerde decodering methode om het niveau van informatie te bepalen die verschillende hersengebieden bevatten over de lokale neuronale populatie. Onze resultaten tonen aan dat verschillende gebieden verschillende niveaus van informatie bevatten die relevant is voor de lokale neuronale activiteit in de SSp-bfd. Bovendien toonden we aan dat eigenschappen van het snorhaar systeem, zoals lateraliteit en connectiviteit, konden worden gereconstrueerd via de gecombineerde microscoop fMRI benadering.

Samengevoegd bieden deze resultaten robuust empirisch bewijs voor de toepassing van gecombineerde microscoop fMRI bij het onderzoeken van hersenactiviteit op verschillende schalen. Bovendien benadrukken de in dit proefschrift gepresenteerde experimenten het voordeel van het opnemen van aanvullende neuroimaging methoden om ons begrip van hersenfuncties te verbeteren.

Trefwoorden: Microscopie, Calcium Imaging, functionele Magnetische Resonantie Beeldvorming, Blood-Oxygen Level Dependent signaal, Neurovasculaire koppeling, Microscopie fMRI.

## Acknowledgements

First, I want to thank my thesis supervisor, Prof. Benjamin Grewe, for the support and supervision during this project. Thanks for making me into an independent researcher and allowing me to follow my own path with this project. It enabled me to develop many skills (some I didn't even know I needed) that I will use throughout the rest of my lifetime.

Second, I want to thank Prof. Valerio Zerbi for always finding the time to answer my questions. Thanks for guiding me through this project, and especially for telling me exactly what I needed to hear when I got stuck because of my own stubbornness.

I also want to thank Prof. Mehmet Fatih Yanik and the neurotechnology lab for providing me with valuable feedback on the project, and especially for trusting us with the MRI. The years of trying to get the perfect image out of this machine have taught me more about the (mostly) scientific process than any course ever could.

I would also like to thank Prof. Daniel Razansky for acting as my co-examiner, and for providing us with feedback about our experiments.

Next, I want to thank the Grewe lab for the countless discussions. I want to give a special thanks to Roman Boehringer and Harald Dermutz for being the driving force behind every aspect of this project (really everything...). You both taught me so much, and without your guidance I don't think this project would have ever ended.

A very deep thank you to all the friends I made along the way. Without your support (and coffee breaks!) I would have never had the endurance to get through this project. I especially want to thank Corinna Lorenz, Pau Vilimelis Aceituno, and Markus Marks for always finding the time to help me when I needed it.

I also want to thank my family for the encouragement throughout the years, and the support they showed when I left The Netherlands to start my journey in Switzerland.

*Ik wil ook mijn familie bedanken voor de aanmoediging door de jaren heen en de steun die ze toonden toen ik Nederland verliet om mijn reis in Zwitserland te beginnen.*

Finally, I want to give a deep thanks to my partner Amy Weng who has supported me through the worst times, and celebrated with me during the best. I would not have been able to do this without your unlimited support (and ability to listen to me go on and on... and on... about this project).

Thank you.



# Contents

<b>General introduction.....</b>	<b>1</b>
1.1 Physical principles of Magnetic Resonance.....	2
1.1.1 The Nuclear Magnetic Resonance effect.....	2
1.1.2 T1, T2, and T2* relaxation.....	4
1.2 Acquisition principles of MRI imaging and reconstruction.....	5
1.2.1 Gradient Echo.....	5
1.2.2 Spatial encoding.....	5
1.2.3 Slice encoding.....	5
1.2.4 Within slice localization and K-space.....	6
1.3 The Blood-Oxygen Level Dependent (BOLD) contrast.....	7
1.4 Neurovascular coupling.....	7
1.5 Neurophysiological optical imaging techniques.....	9
1.5.1 Neural calcium dynamics.....	9
1.5.2 Calcium indicators.....	10
1.5.3 Fluorescence microscopy.....	12
1.6 Technological advances to reconcile fMRI and neural signaling.....	12
<b>Methods.....</b>	<b>14</b>
2.1 Surgical procedures and validation.....	14
2.1.1 Surgical procedures.....	14
2.1.2 Validation of imaging methodology and location.....	16
2.2 Imaging procedures and awake animal fMRI.....	18
2.2.1 Functional and structural MRI imaging parameters.....	18
2.2.2 Calcium imaging parameters.....	18
2.3 Behavioral setup for combined Microscopy-fMRI in awake animals.....	19
2.3.1 Habituation protocol.....	19
2.3.2 Stimulation protocol.....	20
2.3.3 Behavioral apparatus.....	21
2.4 Data preprocessing.....	23
2.4.1 MRI data preprocessing.....	24
2.4.2 Preprocessing of calcium imaging data.....	25
<b>MRI compatible fluorescence microscope.....</b>	<b>27</b>
3.1 Optical design.....	27
3.2 Mechanical design.....	30
<b>Combined microscope fMRI.....</b>	<b>33</b>
4.1 Awake animal functional Magnetic Resonance Imaging.....	33
4.2 Combined microscopic calcium imaging and BOLD fMRI.....	35
4.2.1 Neural and BOLD fMRI responses during whisker stimulation.....	35

4.2.2 Local interactions between SSp-bdf neurons and BOLD fMRI.....	38
4.2.3 The influence of global hemodynamics on the local neural response.....	43
4.3 Single neuron microscopy and cell specificity.....	46
<b>General discussion.....</b>	<b>49</b>
5.1 Brain interactions across scales in awake animals.....	49
5.2 The promise of combined microscopic calcium imaging and BOLD fMRI.....	52
5.3 Limitations of combined microscopic calcium imaging and BOLD fMRI.....	56
5.4 Future prospects of microscopic calcium imaging in BOLD fMRI research.....	59
5.5 Conclusions.....	61
<b>Bibliography.....</b>	<b>62</b>
<b>Appendix.....</b>	<b>72</b>





# Chapter 1

## General introduction

The brain consists of billions of massively interconnected neurons arranged across local circuits and global systems. To explore the neural mechanisms underlying complex cognitive and behavioral functions, neuroscientists have developed a whole spectrum of methods to observe the activity patterns that are generated across the brain.

Traditionally, scientists have used electrical recordings to collect information from the nervous system. The earliest account of an electrical recording of a neuron dates back to 1928, when Edgar Adrian described the recording of electrical discharges in nerve fibers using a Lippman electrometer [1]. Since then the methods to acquire neural signals have progressed significantly, with new technological developments making it possible to record increasing amounts of neural data from the brain [2], [3].

The arrival of functional Magnetic Resonance Imaging (fMRI) in the 1990s [4], [5] promised a new look into the brain on a scale that was never before possible [6]. In addition, it would allow us to acquire brain data without the need for invasive implants. The progress of MRI has been impressive, modern MRI machines can resolve activity in the range of 1 to 3 millimeters in humans, with a temporal resolution of around 700 milliseconds to 2.5 seconds, and can reach sub millimeter voxel<sup>1</sup> size in small rodents. However, the source specificity has been a matter of debate since the first fMRI experiments.

Most contemporary use of fMRI has focussed on the acquisition of brain activity through the blood-oxygen level dependent (BOLD) response. This fMRI contrast relies on the ratio of oxygenated and deoxygenated blood as an indirect approximation of the metabolic need in a local neural circuit. The relationship between the neural response and the metabolic need is mediated by the local vasculature, which has led several research groups to investigate neurovascular coupling in order to better understand the BOLD signal [7], [8], [9], [10], [11]. However, even though significant progress has been made in understanding neurovascular coupling, there are still a considerable amount of ambiguities about the relationship between neural activity and the hemodynamic response.

---

<sup>1</sup> A voxel is a three-dimensional pixel or a volumetric pixel, which numerically represents a value in a three-dimensional grid. The term "voxel" is a combination of "volume" and "pixel."

## 2 Chapter 1. General introduction

---

In this thesis we introduce a novel paradigm that allows us to investigate the relationship between neural activity and the hemodynamic response in awake animals. To this end, we designed an MRI compatible microscope setup that allows us to simultaneously measure calcium-based neural activity and BOLD fMRI in awake mice. In this chapter, we will first introduce the fundamentals of MRI acquisition and microscopy (Chapter 1). In the second part, we will introduce the MRI compatible microscope and experimental procedures we developed for combined microscope fMRI imaging in awake animals (Chapter 2 and 3). Finally, we will describe findings from our combined microscope fMRI experiments (Chapter 4), and place the results into a broader scientific context (Chapter 5).

### 1.1 Physical principles of Magnetic Resonance

MRI is a versatile neuroimaging method that allows researchers to measure both brain function and structure. One of the issues with combining microscopy and fMRI is the introduction of magnetically susceptible elements into the main magnetic field of the MRI machine. This problem is two-fold because not only is the homogeneity of the main magnetic field important for the quality of the MRI signal, the magnetic fields and gradients also exclude the use of certain materials with a strong magnetic susceptibility (ie. certain metals and lenses) inside the MRI machine. To optimize the design of the MRI compatible microscope and the complementary actuators, it is therefore important to understand the underlying principles of magnetic resonance.

#### 1.1.1 The Nuclear Magnetic Resonance effect

In MRI, images are generated based on the magnetic properties of certain atomic nuclei within a volume of tissue [12]. Due to its high natural abundance, one of the preferred nuclei for MRI is hydrogen ( $^1\text{H}$ ). In fact, an estimated ~80% of the brain is made up of hydrogen [13].

The atomic nucleus of  $^1\text{H}$  is composed of a single proton and electron. In the  $^1\text{H}$  atom, the charged electron moves in a circle along the axis of the spin, producing a magnetic moment ( $\mu$ , ie. the magnetic strength and orientation of the particle; **Fig. 1.1a**). The magnetic moment of a single  $^1\text{H}$  atom cannot be measured by an MRI machine. Instead we use net magnetization ( $M$ ), which is defined as the sum over all magnetic moments divided by the volume, assuming the volume has a sufficiently large number of protons but is small enough that external fields can be considered constant over time.

The net magnetization can be viewed as a vector with two components relative to the externally applied field. In MRI, the external field consists of a strong superconducting electromagnet ( $B_0$ ) that is static in both the spatial and temporal domain. The two components consist of the longitudinal component directed parallel to the external field,

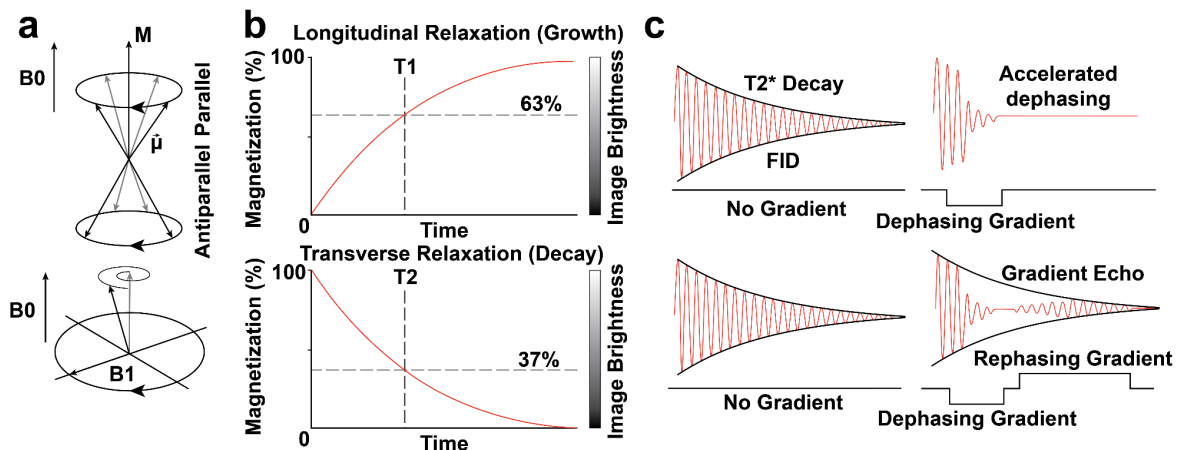


**Figure 1.1. Principles of Magnetic Resonance Imaging [10]** | a) Precession movement of the magnetic vector around the static magnetic field ( $B_0$ ) during equilibrium (top) and stimulation with a magnetic gradient ( $B_1$ ; bottom). b) Longitudinal and transverse relaxation curves with the corresponding time constants and indicator of the corresponding image brightness level. c) Free induction decay (FID) following gradient echo formation using a dephasing and rephasing gradient.

and the transverse component which is perpendicular to the external field (**Fig. 1.1a**). In a natural state (outside the external field), the magnetic moments of  $^1\text{H}$  atoms are oriented randomly, resulting in no overall net magnetization. However, exposure to the  $B_0$  field results in two effects. First, every magnetic moment originating from a nucleus experiences torque in a static magnetic field, causing them to realign parallel to the external field. This means that  $^1\text{H}$  atoms align with the external field in either a parallel (low energy state) or antiparallel (high energy state) fashion (**Fig. 1.1a**). This process is called longitudinal magnetization, and it has a net positive effect on the longitudinal component of the magnetization [14]. In general, a large portion of the protons align parallel versus antiparallel in the direction of the  $B_0$  field, leading to magnetization in the direction of the external field. Second, exposing the  $^1\text{H}$  atoms to the external field results in spontaneous precession around the field vector with a frequency stated by the Larmor equation:

$$\omega_0 = \gamma \cdot B_0$$

Here  $\omega_0$  denotes the Larmor frequency,  $\gamma$  the gyromagnetic ratio (42.57 MHz/Tesla for  $^1\text{H}$  nuclei) and  $B_0$  the primary field. According to the Larmor equation, the frequency changes depending on the strength of the external field and gyromagnetic ratio.

To perturb the net magnetization vector, we can use a radiofrequency (RF) field ( $B_1$ ; **Fig. 1.1a**). The most efficient way to tip the net magnetisation in the transverse plane is by introducing a RF field with the same Larmor/precession frequency as  $^1\text{H}$  atoms (on-resonant condition). The angle between the field vector and the net magnetization vector after applying the RF field is called the Flip Angle ( $\alpha$ ), and is determined by the strength and duration of the  $B_1$ .

### 1.1.2 $T_1$ , $T_2$ , and $T_2^*$ relaxation

Applying the B1 field has two effects on net magnetization. First, it flips a portion of the  $^1\text{H}$  atoms from the low energy to the high energy state, which results in a decrease in longitudinal magnetization. Second, protons become synchronized and start to precess in phase. The net decrease in longitudinal magnetization, combined with synchronized precessing of the nuclei means that the magnetization vector turns towards the transverse plane. Once the B1 field is turned off, the net magnetization will revert back to its original state in a process called relaxation.

There are two types of relaxation corresponding to the two components of the net magnetization vector. First,  $T_1$  relaxation (spin lattice relaxation) defines how fast the longitudinal magnetization reverts back to the original state as more  $^1\text{H}$  nuclei return to their parallel state due to energy transfer from the spin to the lattice. This process results in an exponential increase in the net magnetization of the volume which can be described by the time constant  $T_1$ . The time constant  $T_1$  describes how long it takes for the longitudinal magnetization to restore to 63% of the original magnetization before the activation of the B1 field (**Fig. 1.1b**). Interestingly, different tissue types have different  $T_1$  time constants depending on their biological composition. These different  $T_1$  time constants can be used to differentiate the composition of a certain voxel, which can be used to reconstruct structural images of the brain. In addition,  $T_2$  relaxation (spin spin relaxation) describes the exponential decay of the phase coherence. The time constant  $T_2$  describes the duration of the decay of magnetization in the transverse direction to 37% of the magnetization before the application of the B1 field (**Fig. 1.1b**). However,  $T_2$  relaxation is sensitive to local inhomogeneities in the magnetic field. This is due to the fact that dephasing of  $^1\text{H}$  spins depends on the interaction between local particles, and can occur faster when other magnetically charged sources are nearby. The combined effect of  $T_2$  and the local inhomogeneities are called  $T_2^*$ . However, it is possible to program the pulse sequence to minimize the effect of local inhomogeneities to get closer to the intrinsic  $T_2^*$ . Alternatively, it is also possible to emphasize the effects of local inhomogeneities. This is important for the Blood-Oxygen Level Dependent (BOLD) contrast, and will be discussed in more depth in **section 1.3**.

The relaxation of the spin system can be read out by a RF coil through free induction decay (FID; **Fig. 1.1c**). The FID originates from the reverting of the net magnetic vector to the parallel and dephased state which induces an electric signal that can be detected by the coil. The signal oscillates in sinusoidal fashion near the Larmor frequency (due to local inhomogeneities), and shows an exponential decay that is proportional to the  $T_2^*$  decay.

## 1.2 Acquisition principles of MRI imaging and reconstruction

The MRI signal can be estimated through the FID signal that results from the precessing  $^1\text{H}$  atoms returning to their original alignment with the magnetic field. However, the first part of the FID signal usually has to be omitted due to signal localization steps occurring at the beginning of the FID (excitation phase), meaning that a significant portion of the information is discarded. To retrieve this information, a second excitation step is used to produce an echo of the signal in the first excitation phase. Several techniques have been proposed to produce this echo, including spin echo, gradient echo, and stimulated echo. Here we will focus on gradient echo methods which serve as the basis for the  $T_2^*$ -weighted gradient-echo echo-planar imaging pulse sequence (GE-EPI) used to measure the BOLD fMRI signal in this thesis.

### 1.2.1 Gradient Echo

A gradient echo constitutes a manipulation of the FID designed to optimize the signal and in turn decrease the necessary time to achieve a readout. To generate a gradient echo (**Fig. 1.1c**), two gradients are applied to the sample. Gradients are spatially linear, additional magnetic fields that are applied along the x, y, and z axes of the main magnetic field. In the case of gradient echo sequences, two gradients are used. First, a dephasing gradient field is applied across the tissue. The dephasing results in a calibrated change in the local magnetic field, which alters the Larmor frequency across the tissue, and causes accelerated dephasing of the FID due to  $T_2^*$  decay (**Fig. 1.1c**). After dephasing of the FID, a rephasing gradient is applied with the opposite polarity. This, in turn, reverses the phase scrambling and generates an echo when the magnetic moments of the rephasing and dephasing gradients are equal [15]. The advantages of using gradient echo over for example spin echo sequences is the fast readout speed due to the omission of a 180 degrees pulse. In addition, it has been shown that gradient echo fMRI is less sensitive to motion artifacts than other imaging methods, which makes it easier to acquire data from subjects that demonstrate relatively high amounts of motion such as awake animals.

### 1.2.2 Spatial encoding

The previous description of signal acquisition is agnostic to the location of the signal. However, to create a meaningful image of the brain, spatial information is needed during three-dimensional reconstruction.

### 1.2.3 Slice encoding

Structural and functional MRI involve the construction of a three-dimensional image from a set of two-dimensional slices. To encode the spatial information about the two-dimensional slices, we first apply a gradient along the z-axis. By applying a linear

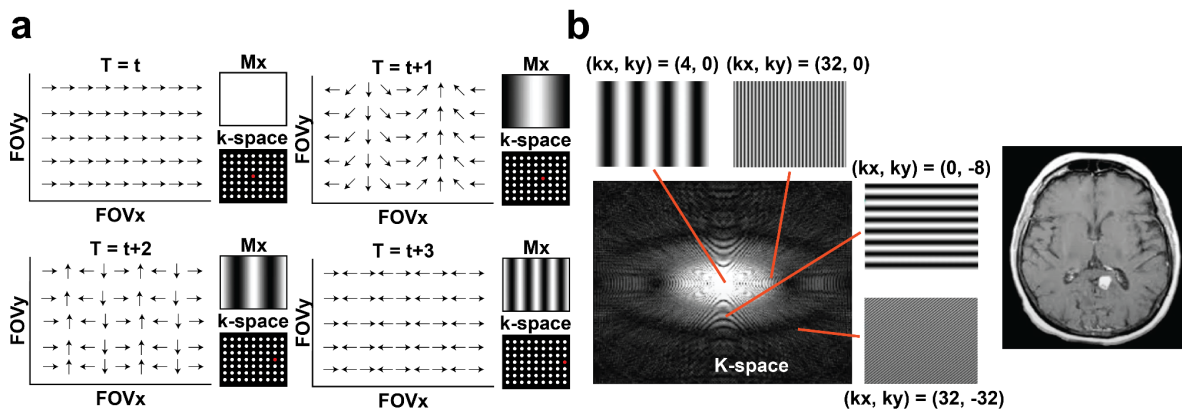


**Figure 1.2. Localization and k-space | a)** Spin frequency and the resulting Fourier basis functions over time within a gradient. **b)** Visual representation of k-space and the basis functions at each spatial location. Performing the inverse Fourier transformation on the k-space image results in the intensity image of a brain slice as shown on the right [10].

gradient, the information about the location along the z-axis becomes encoded in the Larmor frequency associated with the position along the gradient. We can apply an RF pulse with a bandwidth dependent on the frequency range of the desired slice thickness to flip only the  $^1\text{H}$  nuclei in the area of interest into the transverse plane, meaning that the signal we acquire will be confined to a two-dimensional slice. This process can be repeated for different ranges of the Larmor frequency to select sequential slices along the gradient.

### 1.2.4 Within slice localization and K-space

Slice encoding reduces the localization problem from three dimensions to two dimensions. To encode the spatial location within the two-dimensional slice, additional gradients are imposed on the sample. Every point within a slice can be represented along two axes, meaning that two gradients are needed to encode the complete spatial information.

It can be shown that imposing two distinct gradients over a two dimensional slice is equal to performing a Fourier Transformation over the magnitude of the slice. This process can be described as the winding of spins into Fourier basis functions over time along the gradient axes (see **Fig. 1.2a** for a visual representation). In short, for spins in a resting magnetic field ( $B_0$ ), the net magnetization is formed along the axis of the magnet. However, when a gradient is turned on, the spins either increase or decrease their resonance frequency depending on their location along the gradient. This results in spins leading or lagging as compared to the spins in the middle of the gradient, which is generally kept at the same level as the base magnetic field. The readout of the spins along the gradient can be represented as two dimensional oscillation patterns, or Fourier basis functions. Over time, the increase in spin frequency results in more desynchronization between the rows of spins along the gradient. This means that the

---

windings of the resulting oscillation pattern increases over time, providing the image with higher frequency spatial resolution (**Fig. 1.2a**).

In MRI, these Fourier basis functions are read out in discrete time, and are encoded in two dimensional k-space, which provides a representation of the spatial frequency domain of an image after a Fourier transform (**Fig. 1.2b**). In two dimensional k-space, every datapoint along two axes ( $K_x$ ,  $K_y$ ) represents the coefficients for a set of Fourier basis functions that can be combined additively through an inverse Fourier transformation to provide the slice image (**Fig. 1.2b**).

### 1.3 The Blood-Oxygen Level Dependent (BOLD) contrast

One of the most widely used functional MRI contrasts is called the Blood-Oxygen Level Dependent (BOLD) contrast. The BOLD contrast measures the change in regional blood oxy- and deoxygenated hemoglobin levels, and acts as a readout of the local neural activity through a process called neurovascular coupling (described in 1.1.4).

Hemoglobin is a protein that exists in red blood cells, and is responsible for transporting oxygen from the lungs throughout the body. Hemoglobin consists of four polypeptide chains, each of which are bound to a red pigment heme molecule. The heme molecule binds oxygen to a ferrous iron ion at its center for a total of four oxygen molecules per hemoglobin protein. The binding of oxygen is cooperative, leading to a conformational process that facilitates the binding of oxygen at other heme sites. Finally, the formation of the oxyhemoglobin complex is reversible depending on the partial pressure of the present oxygen in the local medium. This means that oxygen binds mainly in the lungs where oxygen levels are high, and dissociates in tissue where the levels are low.

Hemoglobin that is bound with oxygen has no unpaired electrons, meaning it is slightly diamagnetic. In contrast, deoxyhemoglobin contains four unpaired electrons exposed at each iron center, which causes the hemoglobin to become strongly paramagnetic. Due to the paramagnetic properties of deoxyhemoglobin, a local susceptibility gradient is created in the magnetic field, which leads to distortions that suppress the MRI signal. As a result, the regional  $T_2$  and  $T_2^*$  relaxation times decrease as the local deoxyhemoglobin increases. This means that brain regions with more oxyhemoglobin will have a higher signal in BOLD images [5].

### 1.4 Neurovascular coupling

As explained in the previous section, fMRI uses the BOLD contrast as a quantification of neural activity. The BOLD contrast allows us to measure the ratio of oxygenated to deoxygenated hemoglobin in the blood within a voxel. It is important to note that this is an indirect measurement of the underlying neural activity mediated by a coupling transformation between neurons and the vasculature. Neurovascular coupling is a

complex and crucial mechanism that matches the local energy demand of the neural circuit with the supply of energy substrates from the blood [7]. Under conditions when the brain is at rest, the cerebral blood flow (CBF) reaches a steady state between oxygen uptake by the local neural circuit and the supply in the bloodstream. However, during periods of high cognitive load, the activation of the local neural circuits results in a local increase in the metabolic demand for oxygen and nutrients. The vasculature reacts by increasing the CBF in a response termed functional hyperemia. This increase in the CBF in turn causes an increase in the local cerebral blood volume (CBV) [16]–[19]. The increased CBF and CBV results in a larger portion of blood flowing into the region, diluting the local concentration of deoxyhemoglobin. This increases the ratio towards a higher amount of diamagnetic oxygenated hemoglobin in the blood, and a decrease in local magnetic distortions and decay of the T2\* signal. Finally, after reaching the peak, the BOLD signal decreases to a value usually below baseline level. This post-activation undershoot is believed to be the result of a combination of reduced blood flow due to less neural activation, and an increase in the blood volume due to the initial activity.

Early work into the neural processes underlying the BOLD response has shown that the BOLD signal corresponds relatively well to the local field potential (LFP; [8]). The LFP measures the aggregate signal from a group of neurons that are spatially located close to an electrode [8]–[11], [17], and has been argued to reflect the integrated post-synaptic activity and local neural processing [20]. In addition, studies have also shown that negative BOLD inflections could be observed in regions that showed an increase in inhibitory GABAergic activations [21]. These findings have led researchers to conclude that the BOLD response is closely related to local signal integration and neural processing of neurons, and that inhibition leads to a decrease in excitatory activation which is responsible for negative inflections in the BOLD signal [22]–[26]. Within this framework, mostly excitatory neurons play a role in initiating functional hyperemia, while inhibitory activity mostly scales the local excitatory response. This view can be reduced to a linear interpretation of the influence of neural activity on the BOLD signal, meaning that excitatory neural activity scales proportionally with the observed BOLD response. Although this allows for a straightforward interpretation of cognitive functions through BOLD neuroimaging studies, evidence from multiple experiments indicate that this assertion does not hold true in all circumstances. [27]–[31].

The interpretation of the BOLD response as the result of mostly local net excitatory activity can misrepresent certain biological phenomena such as neuromodulation, heterogeneous neural cell populations, and arousal states [27]. For example, cortical circuits consist of both excitatory and inhibitory neurons, and it has been shown that many subgroups of inhibitory neurons have processes that can directly increase or modify local blood vessels [32]–[34], as well as influence cortical hemodynamics on a larger spatial scale as measured by BOLD fMRI [35]–[40]. To better understand the



complexities underlying the formation of the BOLD response, researchers have explored several factors that contribute to neurovascular coupling by leveraging the spatial and temporal resolution of methods that directly measure neural activity.

## **1.5 Neurophysiological optical imaging techniques**

In contrast to fMRI, neurophysiological methods focus on measuring the direct activity of a subset of neurons with a high spatial and temporal resolution. In this section, we will describe calcium imaging, which is a fluorescence microscopy method that measures neural activity through calcium levels within the cell. We will first introduce the concepts behind using cellular calcium levels as a readout for neural activity. In addition, we will describe how calcium levels are visualized through genetically encoded calcium indicators, and how the resulting fluorescence from calcium indicators is imaged in awake mice.

### **1.5.1 Neural calcium dynamics**

Neurons in the brain communicate through the propagation of electrical signals. When a neuron is activated, it transitions from rest to a depolarized state through a process called the action potential [41]. During the resting phase, the neuron maintains a potential of -70 mV due to differences in ion permeability over the cell membrane (a phospholipid bilayer separating the cytosol from the extracellular space). The negative potential inside the cell is maintained by leaky channels and the sodium-potassium pump.

Leaky channels allow for the selective free flow of sodium and potassium ions across the membrane. During rest, there is more potassium within the neuron as compared to the extracellular space. Due to the chemical gradient, the potassium ions are attracted to the extracellular space. However, at the same time, the negative electrical potential in the extracellular space repels potassium, leading to an equilibrium between the two forces. Contrary to potassium, the sodium and chloride concentrations are higher in the extracellular space, meaning that these ions are attracted to the inside of the cellular space. To retain the concentration gradient of sodium and potassium ions inside and outside the cell, and maintain the membrane potential at the -70 mV equilibrium, a cross-membrane sodium-potassium pump exchanges three sodium ions from the inside of the cell with two potassium ions from the extracellular space. This process requires energy that is obtained through a hydrolysis reaction of ATP ( $\text{ATP} + \text{H}_2\text{O} \rightarrow \text{ADP} + \text{P}_i + \text{free energy}$ ). However, neurons do not function in isolation, and are connected to other neurons through synaptic connections. This means that the depolarization of a cell can have an effect on the membrane potential of another cell when they share a connection.

Through the activation of synaptic connections on the dendritic input zones of neurons, afferent cells can become potentiated. This increase in the membrane potential results in the opening of voltage gated sodium channels, causing sodium ions to flow into the cells. The increase of sodium ions inside the cell in turn leads to depolarization. Once the cell becomes depolarized, and reaches the threshold of -55 mV, the action potential is initiated and the neuron potential spikes to 30 mV. During this process, voltage gated potassium channels open, which leads to an outflow of potassium, repolarizing the cell below the resting potential (**Fig. 1.3a**; the undershoot). Finally, the sodium-potassium pump restores the concentration gradient of sodium and potassium ions inside and outside the cell and the cell returns to the resting potential.

Interestingly, the action potential is also coupled to a large and rapid increase in the intracellular calcium concentration. The large difference between intracellular (50-100 nM) and extracellular ( $\pm 1.2$  mM) calcium concentration creates a large inward driving force for calcium, which can enter the cell through voltage-gated calcium channels [42]. Estimates have shown that the increase in free calcium in cortical pyramidal neurons ranges from 150 to 300 nM [43]. Due to the fast calcium influx, calcium transients typically display a sharp increase during action potentials. This sharp increase is usually followed by a slow exponential decay due to calcium buffering and the slow extrusion of calcium from the cytosol [44]. Note that the relative dynamics of calcium are directly related to the electrical potentiation of the neuron. However, while both the action potential and calcium response involve changes in the electrical properties of the cell membrane, the action potential is a rapid, all-or-nothing event due to the thresholded reaction of the voltage gated channels. In contrast, the calcium response consists of a more graded process due to the fact that voltage gated calcium channels can become activated during the subthreshold potentiation of a cell. In addition, due to the delay in the opening of voltage gated calcium channels as a response to electric potentiation, there is a slight delay between the action potential and the calcium response of a cell. Finally, the slow exponential decay due to calcium buffering, expands the duration of the calcium response as compared to the action potential. Combined, this means that the calcium signal consists of a relatively slow, graded response as compared to the action potential.

### 1.5.2 Calcium indicators

Calcium imaging takes advantage of the relationship between the action potential and the calcium response through the use of genetically encoded calcium indicators (GECIs; **Fig. 1.3b**) such as the Green Calcium-modulated Protein (GCaMP) [45]. The GCaMP complex is a protein that changes its reflective properties when it binds calcium, and consists of three key domains; an M13 domain, a calmodulin (CaM) domain, and a chromophore called the green fluorescent protein (GFP) domain at the center. When the surrounding calcium concentration is low, the GFP exists in a protonated state. This means that a proton is added to the amino acid residues of GFP,

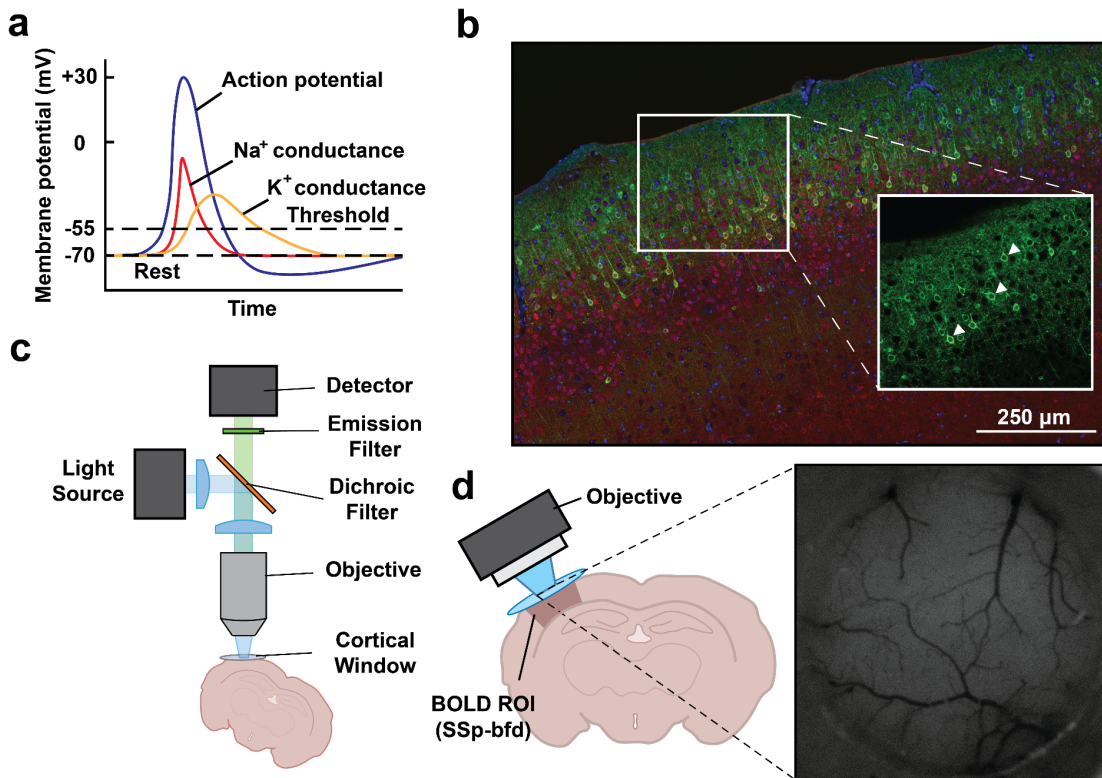


**Figure 1.3. Principles of fluorescence microscopy | a)** Schematic of an action potential and the corresponding sodium and potassium conductances. **b)** Brain slice of the mouse with GCaMP expression in layer 2/3 neurons shown in green. **c)** Schematic of a single-photon fluorescence microscope including the objective, dichroic filter, emission filter, light source, and detector. **d)** Example of an implanted cortical window as viewed through a fluorescence microscope.

resulting in a conjugated acid. However, when calcium binds to the CaM domain, it undergoes a conformational change. This change leads to a tighter bind between the CaM and the M13 domain, which prevents nearby water molecules from accessing the chromophore. This in turn deprotonates the GFP chromophore which transforms the fluorescent properties of GFP to be closer to its native properties. In other words, when calcium binds to the CaM domain, the structural change of the complex allows GFP to fluoresce green shifted light with a peak excitation wavelength at  $\pm 480$  nm and peak emission wavelength at  $\pm 510$  nm. This results in a green observable light when the action potential is coupled with an influx of calcium.

Finally, there are several strategies available to introduce genetically encoded calcium indicators (GECIs) such as GCaMP into neural cells [46][47]. First, viral vectors can be engineered to contain genetic material that codes for specific GECI proteins, as well as genetic material that allows the virus to infect specific subtypes of neural cells. The viral vector can be injected into the brain tissue through local injection where it infects the target neurons. Consequently, the infected cells incorporate the genetic material into the DNA of the neurons, leading to the local synthesis and expression of GECI proteins. Second, GECIs can be expressed through the introduction of foreign DNA

constructs into the fertilized eggs of a target animal through exposure to viral vectors or direct genome editing [48]. The transgenic offspring from the modified eggs will express GECs in the specified cells, allowing for the visualization of their calcium levels using fluorescent microscopy.

### 1.5.3 Fluorescence microscopy

Several optical microscopy designs are used to image the observable light resulting from the calcium influx into the cell. Within the scope of this thesis we will focus on single-photon microscopy. However, for a review of multi-photon microscopy, please see [49] and [50].

In most cases of single-photon calcium imaging, a fluorescence microscope is used (**Fig. 1.3c**). A fluorescence microscope is similar to a conventional light microscope, with several added features to enhance the capabilities of the microscope. During fluorescence microscopy, the specimen is illuminated with light that is matched to the specific excitation spectrum of the fluorophore (GCaMP =  $480 \pm 30$  nm) through a spectral emission filter. When the excitation light radiates the sample, the electrons in the fluorophore are excited to a higher energy level. In response, the excited fluorophore emits a lower energy photon with a longer wavelength. The resulting fluorescence light can then be separated from the background radiation through an emission filter that is specifically designed to match the emission spectrum. Most fluorescence microscopes use the same light path to both excite and detect the emission of the fluorophore (epifluorescence microscopy). This makes it easier to illuminate the sample because it is no longer necessary to have an additional light source close to the sample. To achieve this, a dichroic beamsplitter is placed at a 45 degrees angle in the imaging path. The dichroic beamsplitter reflects photons in the excitation range but passes photons in the emission range, resulting in the introduction of the excitation light in the light path of the microscope.

Using a microscope to observe the brain requires visual access to the area of interest. One possible way of gaining access is by surgically implanting a thin sheet of glass over the area of interest (**Fig. 1.3d**) [51] or through a gradient index (GRIN) lens that can be implanted to access deeper structures in the brain [52]. According to several studies, this method allows for imaging over long periods of time with high optical clarity [53]. In addition, recent findings have also shown that it is possible to measure BOLD fMRI in a mouse implanted with a cortical window without inducing noticeable artifacts [54].

## 1.6 Technological advances to reconcile fMRI and neural signaling

As described throughout this chapter there are a multitude of factors that have an effect on the interaction between neural circuits and the vasculature. Therefore, a more

comprehensive description of neurovascular coupling is crucial for the interpretation of the BOLD signal. This description of the BOLD signal should not be limited to local excitatory neurons, but also include different inhibitory neural subtypes, astrocytes, and vascular cells (pericytes, vascular smooth muscle and endothelial cells). In recent years, a large effort has been made to progress our understanding of neurovascular coupling and the BOLD signal. A particularly promising avenue of research has emerged through the integration of calcium-imaging based optical methods and fMRI.

The earliest and most commonly used *in vivo* combined approach is the use of sequential fMRI and calcium imaging within the same subject [54]. This approach allows researchers to link neural activation acquired using optical calcium imaging with the BOLD signal from the sequential fMRI experiment. However, it only allows for the comparison between averaged responses, and does not account for variation between sessions, experimental conditions or the mental state of the subject during the recording. In order to address these challenges, multiple research groups have developed techniques to concurrently measure BOLD fMRI and calcium-based fiber photometry in anesthetized rodents [55]–[57]. Early results from these studies have already demonstrated that the BOLD signal is not only the consequence of local neural processing, but also reflects slow oscillating calcium waves induced by glial cell activity [55]. These results emphasize the complexity of interactions between the local circuitry and intracranial vasculature [58]–[60].

Expanding on the technological advances possible through combined fiber photometry fMRI, [61] developed a multi-fiber bundle that was able to record the simultaneous activity of mesoscale calcium activity across the cortex and BOLD fMRI, demonstrating the power of combining optical imaging and fMRI. However, fiber-based recordings can only provide a coarse average measurement of the local calcium activity, grouping together synaptic, dendritic, and neural signals. To overcome this challenge, we developed a novel combined imaging approach that integrates an MRI compatible microscope with BOLD fMRI. This approach allows us to simultaneously image the calcium activity of genetically defined neurons and BOLD fMRI in awake mice. Having access to the simultaneous single local neural activity and BOLD fMRI could result in a better understanding of the neurovascular dynamics underlying BOLD fMRI, and lead to an improved interpretation of the neural activity underlying the BOLD fMRI activity of humans in both health and disease.

## Chapter 2

### Methods

In this chapter, we will introduce the experimental and surgical procedures used in the awake animal, combined microscope fMRI experiments. The approach and protocols described in this chapter form the basis for the acquisition and processing of all datasets presented in this thesis.

#### 2.1 Surgical procedures and validation

The quality of the cortical implant is fundamental to calcium imaging and fMRI experiments. However, the factors contributing to the quality of the implant are different, and sometimes incompatible, for both experimental modalities. Therefore it is important to find a balanced solution, resulting in the optimal data quality for both methods. In this section, we will elaborate on the surgical approach we developed for combined microscope fMRI experiments. In addition, we will provide results from the validation steps that were taken to ensure the accuracy and quality of the procedures.

All procedures were authorized by the veterinary office of the Canton Zurich, Switzerland, and are in agreement with the guidelines published in the European Communities Council Directive of November 24, 1986 (86/609/EEC).

##### 2.1.1 Surgical procedures

During combined microscope fMRI experiments, we encountered multiple challenges stemming from both the constraints of BOLD fMRI and calcium imaging experiments. In this section, we will provide a description of the necessary preparations, as well as precautions, needed for combined microscope fMRI experiments.

**Animals.** The main experiments were performed using six Rasgrf2-2A-dCre [62] mice crossbred with Ai148D (25-35 g; Jackson Laboratory), between four and six months old at the time of experiments. Animals expressed the calcium indicator GCaMP6m [63], which was transgenically induced in excitatory neurons across layer 2/3 of the cortex. Transgenic mouse lines do not require the injection of a viral vector through a craniotomy. This significantly reduces the complexity of the surgery, while simultaneously providing high quality optical recordings.

In addition to the main experiments, we investigated the feasibility of imaging inhibitory neurons using the MRI compatible microscope. Experiments were performed using

---

three Sst-IRES-Cre mice injected with ssAAV-9/2-hSyn1-dlox-jGCaMP8s(rev)-dlox-WPRE-SV40p(A) by means of a microinjector (Microinjection Syringe Pump, World Precision Instruments). This procedure introduced GCaMP8s into the somatostatin positive inhibitory neurons in the SSp-bfd.

All animals were housed in individually ventilated cages (IVC) and kept on a 12/12 hour light cycle (light from 7:00 am to 7:00 pm). Animals were also provided with unlimited access to food and water. After transfer from the breeding to the animal holding facilities, mice were given two weeks to acclimatize to the new environment before surgery. After surgery, mice were individually housed for the duration of the experiments.

**Anesthesia.** For all procedures, mice received preemptive buprenorphine (Bupaq, Streuli; 0.1 mg/Kg) 30 minutes prior to anesthesia. Anesthesia was induced with 3% Isoflurane and maintained using 0.5-1.5% during surgery. After the mouse was installed in the stereotaxic frame (Kopf Instruments), hair was removed around the planned incision using dilapidation cream. During the whole surgical procedure, mice received 95% medical O<sub>2</sub> (Pangas, Conoxia) through a face mask, while body temperature was kept at 37 degrees Celsius using a temperature controller and a heating pad.

**Cortical implant.** Before resection of the cranium the scalp was desensitized using a combination of Lidocaine and epinephrine (Lidocain-Epinepherin, Streuli Pharma AG). After the scalp was removed, the skull surface was cleared of soft tissue and debris. To ensure the stability of the implant, the skull surface was increased by applying a thin layer of phosphoric acid gel (etching gel; DMG Dental-Material GmbH). Excess blood and other fluids were carefully removed and a thin layer of Scotchbond universal adhesive (Scotchbond, 3M) was applied to stabilize the exposed skull. Scotchbond was tested and found to have a negligible effect on BOLD fMRI signal-to-noise ratio, while providing the strength needed to ensure stable calcium and fMRI recordings in awake mice (**Fig. 2.1a**).

To gain optical access to the cortex, a craniotomy was performed over the region of interest (SSp-bfd, AP = 2.0 mm, LR = 3.0 mm). The craniotomy was sealed with a single borosilicate glass cranial window (3 mm diameter) to enable long term recordings of the SSp-bfd (for a detailed description, see [51]). After the cortical window was fixed in place using UV and moisture-curable adhesive (Loctite 4305, Henkel), a head constraint (Polyether ether ketone, PEEK; **Fig. 2.1b**) was placed around the window and attached with Scotchbond. The head constraint was custom designed to submerge the cortical window in D<sub>2</sub>O (D-content 99.9%; Sigma–Aldrich) during imaging. This was necessary to avoid artifacts due to large differences in magnetic susceptibility of the material and the surrounding (ie. brain to air transition; **Fig. 2.1c**).

**Analgesia.** Three days following the surgical procedure, animals were provided with analgesic treatment. Animals received subcutaneous Buprenorphine (Bupaq; Streuli,

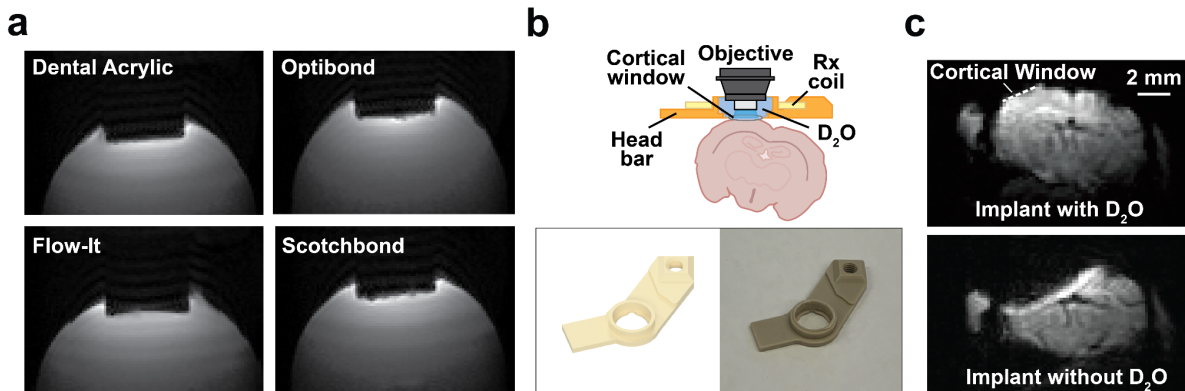


**Figure 2.1. Head implant and artefacts | a)** Artefacts were minimal for most of the tested glues, except for warping effects in the case of Flow-It. The small susceptibility artifacts in the case of Scotchbond and Optibond were found to be caused by entrapped air. **b)** Overview of the implant including the head constraint, RF receive coil (Rx Coil), and the microscope objective (top). Bottom panel shows a rendering and picture of the PEEK head constraint **c)** BOLD fMRI image of the same mouse with the MR compatible head implant. Notice the strong distortions in the absence of D<sub>2</sub>O.

0.1 mg/Kg) every 6 h during the light day cycle and in the drinking water (Bupaq; Streuli, 0.01mg/mL) during the dark night cycle. In addition, Carprofen (Rimadyl; Zoetis, 4 mg/Kg) was administered subcutaneously every 12 h to prevent inflammation.

### 2.1.2 Validation of imaging methodology and location

**Perfusion.** After completion of experiments animals were administered terminal anesthesia with Pentobarbital (Esconarkon; Streuli, 200 mg/Kg). Subsequently, mice were perfused transcardially with PBS followed by 4% paraformaldehyde (PFA), and brain tissue was carefully removed. After post-fixation for 24-48 hours in 4% PFA, 50  $\mu$ m thick coronal slices were acquired using a Vibratome (VT1000 S; Leica) and stored in PBS.

**Verification of cell type.** Standard immunofluorescence protocols were used to stain inhibitory and excitatory neurons. Slides were incubated overnight at 4° C with either the primary antibody rabbit anti-Neurogranin (1:2000, 07-425 Millipore) or rabbit anti-GAD65 (1:500, AB1511, Millipore). This was followed by a 2-hour incubation at room temperature with the secondary antibody Alexa 594 anti-rabbit (1:200, A-11062 Invitrogen). Slides were further stained for 4 min with 4',6-diamidino-2-phenylindole (DAPI; 1:1000, D1306, Invitrogen) in PB (0.1M) prior to mounting.

Confocal pictures were taken at wavelength 594 (Neurogranin or GAD65), wavelength 488 (GCaMP6m), and wavelength 390 (DAPI). This allowed us to compare the pictures for overlap of labeling (**Fig. 2.2a-d**). In addition, we used a reference brain atlas [64], [65] to determine the position of the cortical window (**Fig. 2.2a**). This approach consistently showed that all the animals had their cortical window over the SSp-bfd.



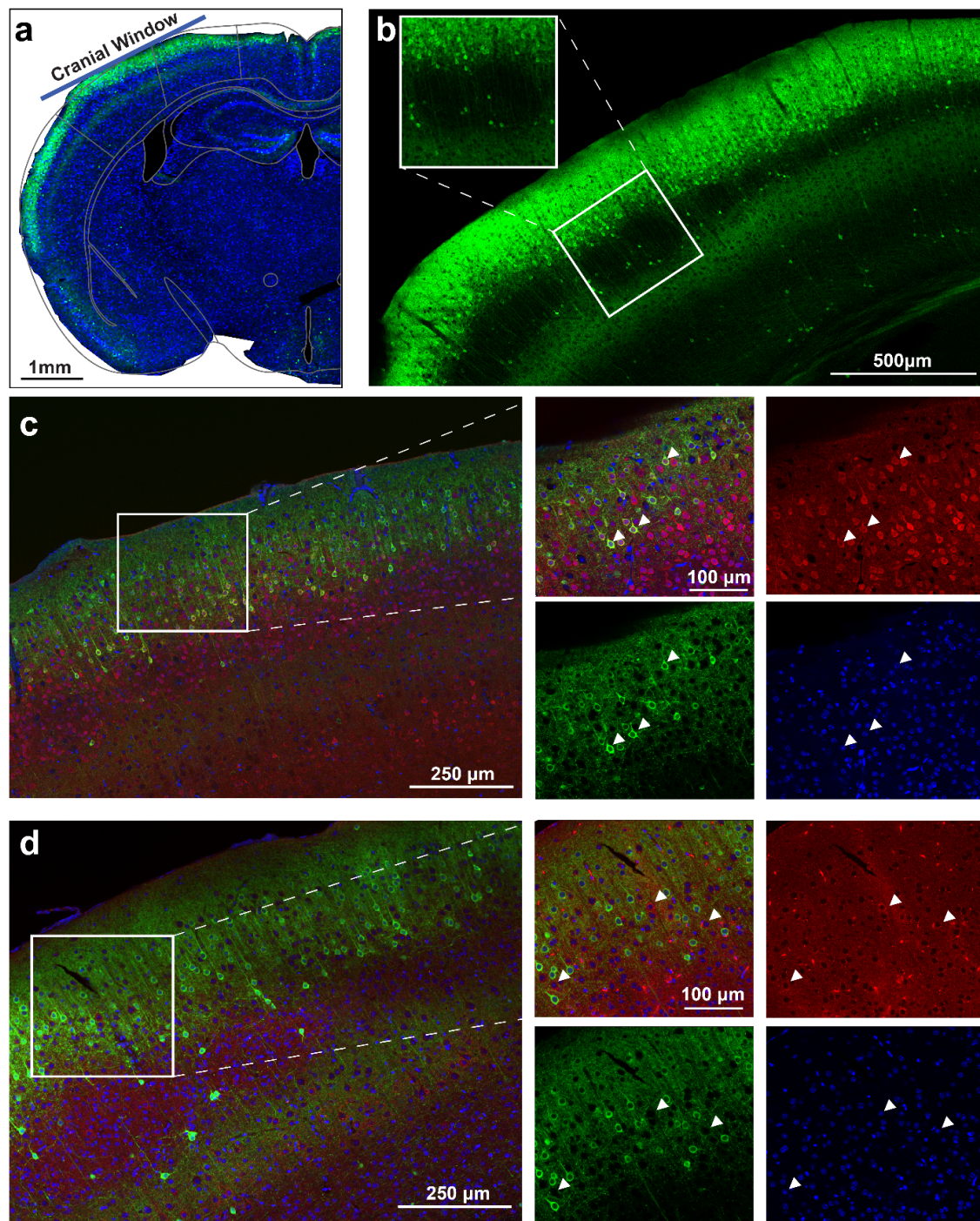


**Figure 2.2. Cell-type verification** | a) Coronal brain slice stained with DAPI (blue) and expression of GCaMP6m (green) in layer 2/3 of a *Rasgrf-2A-Cre* animal. The cranial window is shown as a blue line located above the SSp-bfd. b) Close-up of the same slice with a blow-up of the barrel fields. c) Immunohistological verification of different cell-types. Neurogranin positive cells are shown in red, GCaMP is shown in green, and DAPI in blue. d) Immunohistological verification of different cell-types. GAD65+67 positive cells are shown in red, GCaMP is shown in green, and DAPI in blue.

## 2.2 Imaging procedures and awake animal fMRI

### 2.2.1 Functional and structural MRI imaging parameters

All data presented in this thesis was acquired using a 7T/11 cm horizontal bore scanner (BioSpec 70/20 USR, BRUKER BioSpin MRI GmbH) equipped with a BGA 9SHP (90mm, max 750 mT/m gradient strength, slew rate 6840 T/m/s, BRUKER BioSpin MRI GmbH). The scanner was fitted with a RF RES 300 1H 089/072 QSN TR AD volume coil combined with an RF SUC 300 1H LNA AV3 surface coil to receive the radiofrequency signal (BRUKER BioSpin MRI GmbH). The surface coil had an inner diameter of 10 mm, which was used to accommodate the objective of the microscope.

For all experiments, we used a single-shot gradient-echo (GE) echo planar imaging (EPI) pulse sequence (TE/TR: 15/1500, BW: 250 kHz, FA: 60, FOV: 20/10, Image Size: 100/50, In Plane resolution: 0.2/0.2/0.8, Slices: 7, Slice Gap: 0.1) to acquire the BOLD fMRI signal. In addition, at the end of each session, a T2-weighted 3D TurboRARE was obtained (TE/TR: 21.86/2500, FOV: 20/10, Image Size: 180/120, In Plane resolution: 0.111/0.083/0.8, Slices: 7, Slice Gap: 0.1). This high resolution structural image was used for image registration as described in **section 2.4.1**, and quality control of the implant.

### 2.2.2 Calcium imaging parameters

During BOLD fMRI acquisition simultaneous calcium activity of a cell population in the SSp-bfd was recorded using a fully MR-compatible microscope (described in chapter 3). We acquired frames of 1280x960 pixels at 12 bit with a free running frame rate of 10 Hz using custom C++ code.

The optimal laser intensity was determined during the setup of each experiment. The optimal was defined as the minimal value which produced sufficiently bright images that still showed calcium transients. This value was dependent on the strength of the GCaMP6m expression, and we found that a laser intensity between 0.1-0.3 mW/mm<sup>2</sup> reliably gave calcium transients for all mice. In addition, previous studies showed that high light intensity from optical experiments can lead to increases in temperature of the imaged tissue, resulting in changes of the T1 and T2\* relaxation times [66]. To avoid any confounding factors due to tissue heating, we only activated the laser during the period between ten seconds before and ten seconds after the stimulus.

All recorded data was directly streamed and saved to the hard-drive of a desktop computer and synchronized with the recorded stimulus times and BOLD fMRI acquisition.

## 2.3 Behavioral setup for combined Microscopy-fMRI in awake animals

### 2.3.1 Habituation protocol

During the experiments outlined in this thesis, BOLD fMRI acquired a full brain image every 1.5 seconds. Due to this slow temporal readout of the BOLD fMRI signal, fast movements can cause signal displacement within one acquisition cycle. In addition, experimental findings have shown that neuromodulatory factors such as stress have a strong effect on the hemodynamics as measured with fMRI [67]–[69]. To minimize external confounders in our BOLD fMRI measurements, we implemented a rigorous habituation protocol.

Animals were allowed to recover for at least fourteen days after implantation of the head implant. During the recovery period, we handled the animal twice a day for a period of at least 3 minutes. This procedure increased the familiarity between the animal and the researcher, leading to less stress during interactions. After the animal had fully recovered from the surgery, and did not show significant tension during handling [70], the habituation period was initiated. The duration of the habituation period was dependent on the behavioral performance of each individual animal, and lasted a minimum of 10 days. During the first week, the animals were restrained in a mock MRI machine once a day for two or three days followed by one day of rest. The duration of the head fixation started at 10 minutes, and was increased by 5 minutes till the average duration of a full experiment was reached (30 minutes). MRI scanner sounds were introduced during the fourth day of habituation, and gradually increased till it reached the same sound pressure level as experienced during an MRI session (~95 dB). Finally, a blue ambient light was used to mimic the on-off cycles of the MR-compatible microscope excitation light.

Once the animal showed no discernible response to the head fixation, sound pressure level, and excitation light [70], [71], the habituation was continued inside the MRI machine. The habituation sessions consisted of a functional scan that included the full stimulation protocol (see **section 2.3.2**) and a structural scan. The temporal readout of the brain during functional scans allowed us to evaluate the behavioral performance of each animal (**Fig. 2.3a, b**). We calculated the framewise displacement (FWD) with respect to a reference frame as a set of rigid body transformations described in [72]. This yielded six motion parameters (x, y, z displacement and roll, pitch, yaw) for each timestep, that formed the FWD over time according to:

$$FWD_i = |\Delta x_i| + |\Delta y_i| + |\Delta z_i| + |\Delta \alpha_i| + |\Delta \beta_i| + |\Delta \gamma_i|$$

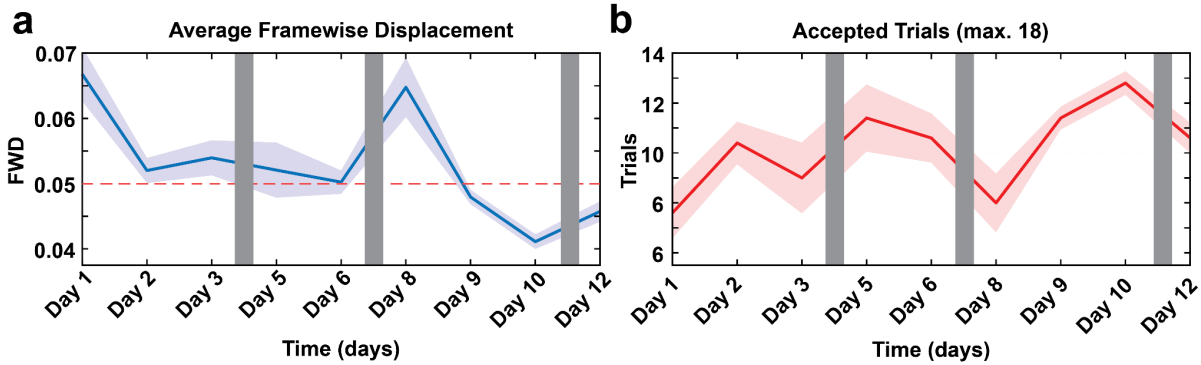


**Figure 2.3. Behavioral performance** | **a**) The average framewise displacement (FWD) over the whole session averaged for all pilot animals (mean  $\pm$  SEM). The red line indicates the inclusion threshold, and the gray bars denote the rest days. **b**) The number of accepted trials per session averaged over all pilot animals (mean  $\pm$  SEM). The red line indicates the inclusion threshold, and the gray bars indicate the rest days.

Where each parameter for  $p = [d_{ix} \ d_{iy} \ d_{iz} \ \alpha_i \ \beta_i \ \gamma_i]$  was calculated by,

$$\Delta p_i = p(i - 1) - p_i$$

Habituation was considered successful when the average FWD for a full session was below 0.05 mm, and at least 50% of trials showed no excessive motion (FWD spikes  $>$  0.075 mm). The values for the FWD thresholds were chosen based on the BOLD fMRI acquisition sequence, where FWD spikes should not exceed more than 50% of the voxel size due to spill over of the signal in nearby voxels.

To avoid accidental damage to the cortical window, the silicone protection layer was left in place during the full habituation period with the exception of an initial quality control session of the head implant. This resulted in a large artifact around the cortical window during BOLD fMRI recordings. To circumvent this issue we registered each functional volume to the first volume of the session, and corrected for temporal drift before calculating the motion parameters.

Note that the data in **Figure 2.3** comes from an initial behavioral pilot experiment meant to optimize the habituation protocol and the stimulation parameters. During the pilot study 18 trials were presented to each animal during each session. However, after 12 presentations the mice demonstrated high amounts of movement, leading us to limit the stimulus presentations to 12 for the remainder of our experiments.

### 2.3.2 Stimulation protocol

To assess the functionality of our combined microscope fMRI setup, we imaged the evoked BOLD fMRI and cellular calcium responses simultaneously within the same awake mouse. Due to the constraints of the magnetic environment we used a custom 3D-printed MR-compatible pneumatic actuator (described in **section 2.3.3**). The pneumatic device was used to stimulate the whisker pad contralateral to the implanted

cortical window for 10 seconds at 3 Hz (40 ms duty cycle). Each experiment consisted of 12 trials followed by an inter-trial interval of 40 seconds. The long duration between trials was necessary to allow the BOLD fMRI signal to stabilize after stimulation.

### 2.3.3 Behavioral apparatus

In this section, we will detail the behavioral apparatus used to safely restrain and stimulate the mouse within the MRI machine. In addition, we will describe the translational z-stage that facilitates the precise placement of the MR-compatible microscope. The behavioral apparatus was designed through 3D printing, and all materials were determined to be MRI compatible.

**Basic components.** A combination of custom build and commercially available hardware was used to create the MRI compatible cradle and stimulation equipment (**Fig. 2.4a**). The cradle was 3D printed out of MRI compatible material (**Fig. 2.4a, e, f**). A resin analogous to acrylic (VeroClear, StrataSys) combined with polyjet printing (PJ) was used for parts where high resolution was necessary (**Fig. 2.4c, e, f**), while white PETG was used for all other parts through Fused Deposition Modeling (FDM; **Fig. 2.4b, e, f**). The side rails of the cradle were constructed of PEEK and carbon fiber, and provided the structural integrity of the cradle. All parts were designed with a small spatial footprint due to the small circumference of the RF RES volume coil (**Fig. 2.4d**; 300 1H 089/072 QSN TR AD, BRUKER BioSpin MRI GmbH).

All experiments were controlled and synchronized through a PC running software written in Laboratory Virtual Instrument Engineering Workbench (LabVIEW; National Instruments). The PC was connected to the pneumatic actuators, behavioral camera, and MRI compatible microscope trigger system via a PCI card (PCIe-6323; National Instruments) and a data acquisition device (BNC-2090A; National Instruments).

**Whisker stimulation air blade.** Pneumatic actuators are capable of inducing whisker movement without causing BOLD fMRI signal degradation. Usually, whisker stimulation experiments in MRI environments use silicone tubes aimed at the whisker tips. However, there are two disadvantages associated with this approach. First, after the pressurized air is extruded from the tube, it disperses over a wide area. Due to the dispersion, it is possible that the air hits the other facial areas of the mouse, leading to an adverse reaction. Second, a large number of tubes is necessary to displace enough air to hit the full whisker set. For the experiments in this thesis we used a custom designed air blade to ensure that the pressurized air displaced a large amount of whiskers, while avoiding other parts of the mouse body (**Fig. 2.4c**).

**Translational z-stage for the MRI compatible microscope.** The manual translational stage enables the precise movement of the microscope along the z-axis, which allows us to precisely focus the microscope through vertical adjustments in small increments. Translational stages are typically constructed of steel and other high-strength materials

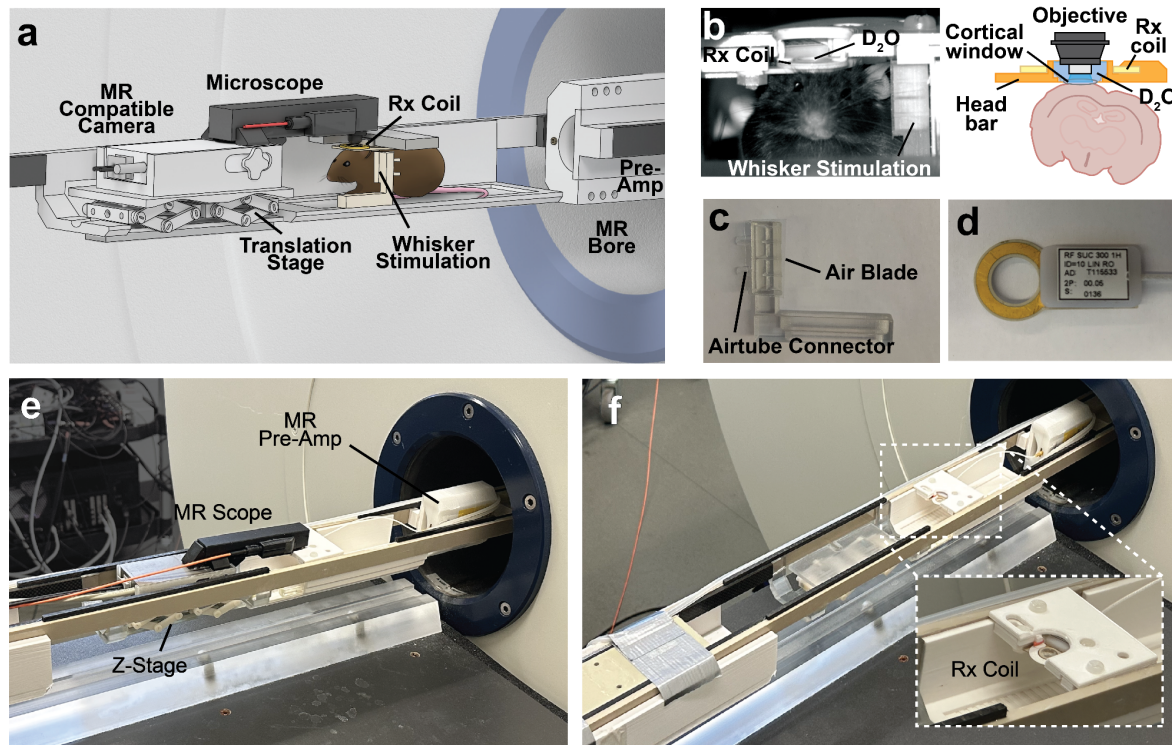
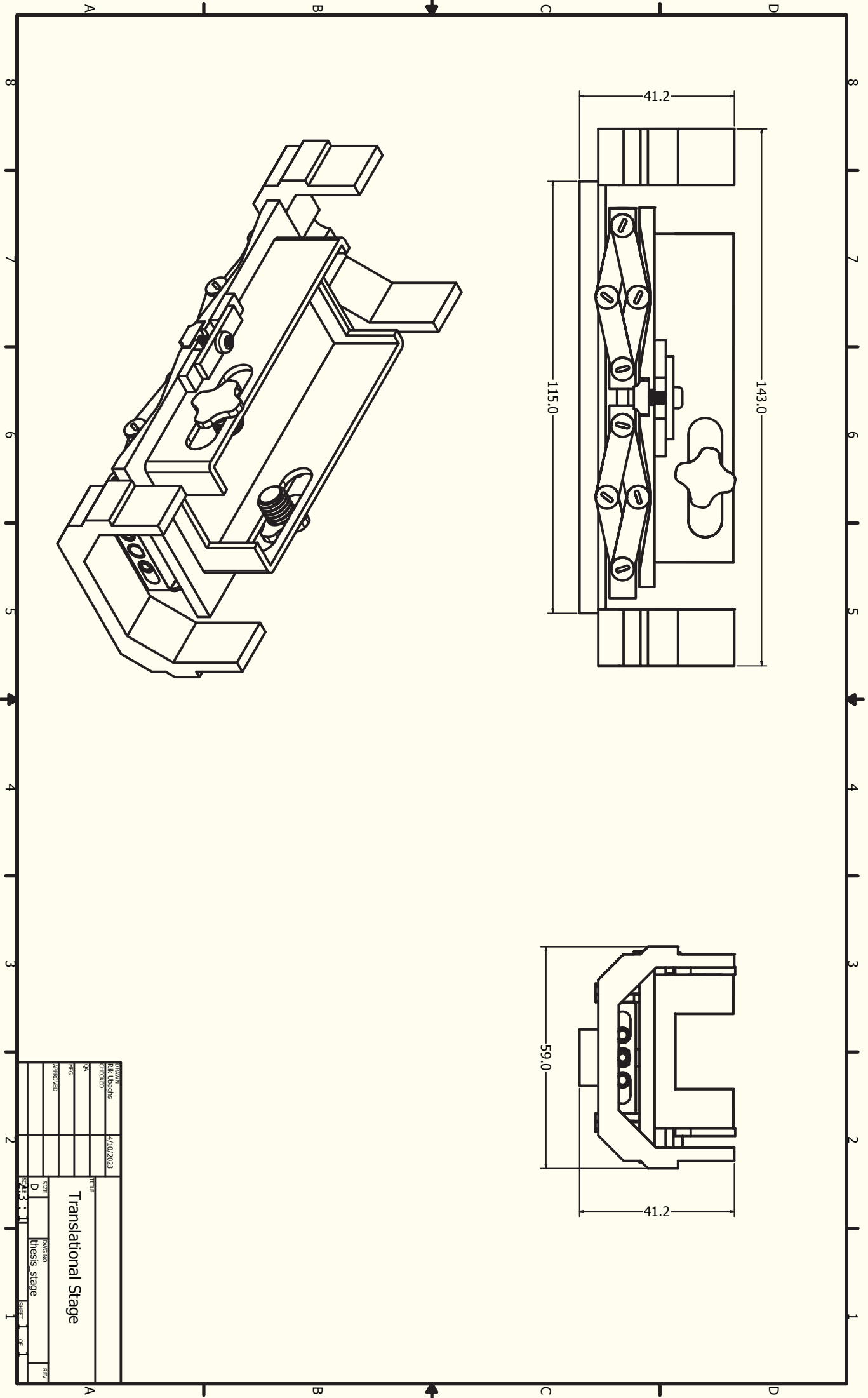
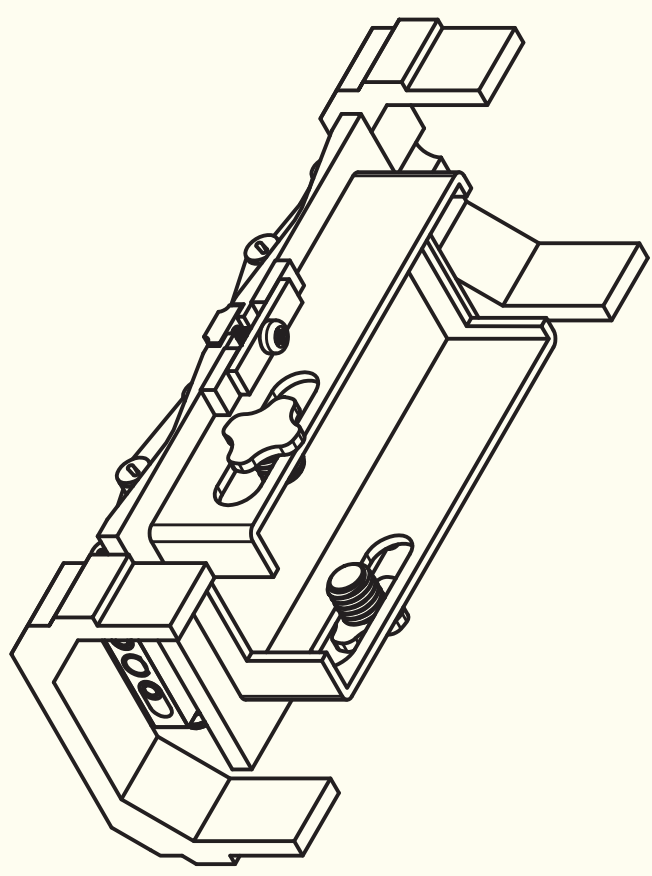
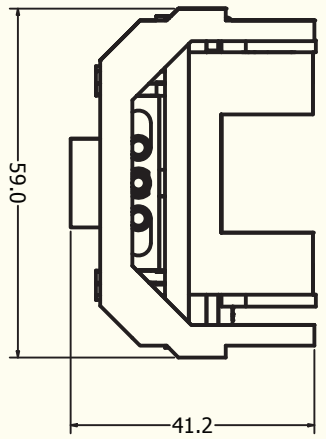
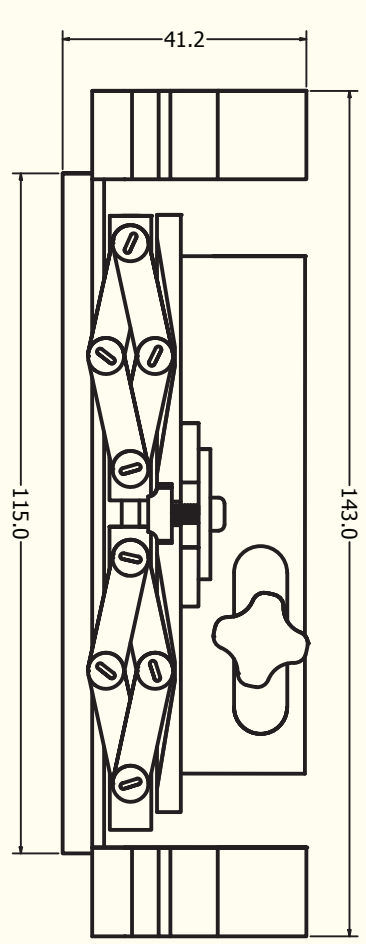


**Figure 2.4. Behavioral setup for simultaneous Microscopy-fMRI recordings** | a) Complete fMRI imaging setup including the microscope, a translational stage for focusing, the receiver (Rx) coil, the whisker stimulation apparatus, the head fixation stage, the pre-amplifier, and the MRI scanner. b) Close up of a head fixated mouse and a schematic of the head implant and microscope position. c) The custom whisker stimulation air-blade device. d) The 10 mm inner diameter surface RF coil used for collecting the BOLD fMRI signal. e) Image of the build MR cradle with the MR compatible microscope and the z-stage. f) Image of the build MR cradle without the MR compatible microscope. Inlay shows the placement of the RF coil with respect to the mouse head position.

to accommodate high loads. However, because the translational stage is positioned inside the MRI machine, the magnetic susceptibility of these materials would induce motion during travel through the magnetic field. Therefore we designed a custom z-stage out of MRI compatible plastics with a high tensile strength, combined with a minimal amount of metal parts with low magnetic susceptibility.

The main components of the z-stage were constructed through PolyJet 3D printing out of a resin analogous to acrylic (VeroClear, StrataSys). This resin showed minimal erosion during continuous friction and demonstrated a high tensile strength. The linear guides and precision screws designed to provide smooth and precise linear motion along the defined path were produced out of aluminum. The choice to produce these parts out of metal instead of plastic was due to the high amount of structural strain placed on these parts during microscope alignment. Aluminum is a non-ferromagnetic low-density metal, meaning it does not contain iron or other magnetic metals that could be manipulated by the magnetic field. We found that the use of these materials for the translational stage did not induce artifacts or degrade the BOLD fMRI signal quality, and performed well when used for translation of the microscope along the z-axis.



DESIGNED	K.R. Deshpande	DATE	24/10/2023
CHECKED			
DATE			
APPROVED			
TITLE		Translational Stage	
SCALE	D	DRAWING NO.	thesis_stage
REV		DATE	

### 2.4 Data preprocessing

#### 2.4.1 MRI data preprocessing

MRI data was collected in the proprietary Bruker ParaVision format, and consequently converted to BIDS through the Bruker-to-BIDS repositioning pipeline of the SAMRI package [73]. After the data was converted to the BIDS format, the Generic registration workflow was used to preprocess the data [74], [75]. Within this pipeline, the data was preprocessed by performing motion and slice timing corrections, bias field correction, registration to an atlas, and spatiotemporal smoothing.

**Motion and slice timing correction.** Motion and slice timing correction was done using the algorithm described in [76]. The algorithm consists of two stages: the first stage estimates motion parameters using a rigid-body registration algorithm, while the second stage estimates slice timing parameters by fitting a model to the data. The algorithm is designed to jointly estimate both types of parameters, which can improve the accuracy of motion correction by accounting for differences in slice acquisition times.

**Bias field correction and registration.** After all volumes are corrected for motion and slice timing differences, the temporal mean over the functional scan is calculated and corrected for the bias field using optimized spatial parameters adapted to small animal features (ANTs N4BiasFieldCorrection; [77]). The same operation is performed on the structural scan as well.

**Registration.** Next, the data was transformed to a stereotypically oriented standard space (DSURQEC template space, distributed in the Mouse Brain Atlases Package; [78]). First, the structural scan was registered to the reference template using the `antsRegistration` function (ANTs `antsRegistration`; [77]) with spatial parameters that were specifically adapted to anatomical brain features in small animals. Second, the temporal mean of the functional scans was registered to the anatomical scan using the same approach. Finally, the two transformation matrices were merged and applied to the whole functional scan.

**Smoothing.** Finally, we applied spatial smoothing in the coronal plane up to 200  $\mu\text{m}$  [79], and the data was low-pass filtered in the temporal domain with a period threshold of 100 seconds.

**Statistics.** After preprocessing, the volumetric data was modeled using FSL ([80]; version 6.0.4), through subject level regression. The six motion parameters and their first derivatives acquired from the motion correction were used as covariates in the model. Next, the subject level contrasts and variance estimates were used as input into the group level analysis through FSL's FLAMEO using a gaussian hemodynamic response function (phase = 0s, sigma = 2.8s, peak lag = 5s). Finally, the average time



series was extracted over all significantly activated voxels after cluster correction (z-score  $\geq 3.1$ , FWE  $P \leq 0.000001$ ) and re-expressed in units of relative change in the BOLD signal given by:

$$\Delta BOLD(t) = (BOLD(t) - BOLD_0) / BOLD_0$$

where  $BOLD_0$  is the median filtered value (window size of 180 seconds) at each timestep.

#### 2.4.2 Preprocessing of calcium imaging data

Calcium imaging frames of 1280x960 pixels at 12 bit were recorded with a free running frame rate of 10 Hz using custom C++ code. Due to the excitation light being turned off in between trials to minimize bleaching and unexpected vascular effects, not all frames had visible light. Frames that did not show excitation emission were removed before preprocessing steps and signal extraction.

**Motion correction and temporal downsampling.** To account for motion during recordings, we used an image registration method to account for spatial translations in the field of view (Turboreg; [81]). To improve the accuracy of the registration process, we enhanced constant structural features such as blood vessels by applying a spatial band-pass filter. For each dataset presented in this thesis we manually defined the cutoff range by visually inspecting the results of the filtering procedure. Next, a random frame was selected to which all remaining frames were registered to in pairwise fashion. Finally, pixels at the edge of the field of view that did not have numerical values due to motion induced spatial shifts were removed, and the data was downsampled to a frame rate of 5 Hz.

**Cell extraction.** We extracted both the cellular activity traces as well as the background activity from our calcium imaging recordings using CNMF-E [82]. CNMF-E uses a constrained matrix factorization approach that accurately classifies background activity in calcium imaging recordings, and subsequently demixes and denoises the neural signals.

Constrained matrix factorization is used to reduce the dimensionality of high-dimensional datasets. The main goal is to factorize a given matrix into two lower-dimensional matrices, one of which captures the essential features of the original data while the other describes how these features are combined to form the original data. CNMF-E assumes that the fluorescent calcium activity of each source can be expressed as a matrix given by the outer product of two vectors [83]. The first vector,  $a$ , represents the spatial filter of each source, and the second vector,  $c$ , represents the fluorescence. This can be represented as following:

$$F(w, t) = \sum_{i=1}^K a_i(x)c_i(t) + B(x, t)$$

$$Y(x, t) = F(x, t) + \varepsilon_{x,t}$$

In this notation,  $F(x, t)$  denotes the total fluorescence at a certain location and time, and  $B(x, t)$  describes the background fluorescence. The objective function can then be constrained using various biologically plausible constraints such as cell size or expected fluorescence dynamics.

One problem with single photon microscopy is that the excitation light is not confined to a small volume, which results in a larger area over which fluorescence is integrated. This means that scattered fluorescence from nearby processes (e.g. axons, dendrites, synaptic boutons) and background sources that are not in focus are blended in with the background fluorescence signal. One method to minimize pollution of the background signal by unwanted neural activity is to use specific targeting strategies. For example, in the current thesis, only layer 2/3 neurons are targeted, meaning that a considerable amount of fluorescence originates from neurons in these layers. An alternative method is to explicitly model the spatial and temporal structure of the background fluorescence. Consequently, this model can be used as part of the source extraction, meaning the variance in the data that is best described by the background model will not contaminate the cellular components. In the case of CNMF-E an autoregressive model was used to model the background at each spatial location as a linear combination of the values of the background in an annulus around the cells.

**Post-processing and validation.** After the extraction of the activity traces and spatial outlines of each neuron in the field of view, we manually annotated the cells for each subject to assess the accuracy of the extraction process. We used the neuron shape, stability of the neural trace, temporal evolution of identified events (calcium indicator dynamics), and the consistency of the identified events over the session to classify whether an extracted feature represented cellular activity. A total of 203 layer 2/3 SSp-bfd neurons ( $51 \pm 13$  per animal; mean  $\pm$  s.d.;  $N = 4$ ) were extracted from the MRI compatible microscope recordings. We were unable to extract cells from two animals due to problems with the preparation, leading us to exclude them from analysis that involved neural activity.

## Chapter 3

# MRI compatible fluorescence microscope

To investigate the interaction between neural dynamics and the BOLD fMRI signal we developed a novel paradigm that enables researchers to measure simultaneous single-cell calcium activity and BOLD fMRI in awake animals. For the development of an MRI compatible microscope, it is important that each component is designed such that it minimizes artifacts in the MRI acquisition, while optimizing the optical performance of the microscope. This excludes the use of certain materials and design principles that are commonly used in microscopy. In this chapter, we present an MRI compatible microscope that is capable of measuring simultaneous single-cell calcium activity during acquisition of whole-brain BOLD fMRI, and explain the rationale behind the tradeoffs that were made.

### 3.1 Optical design

The main components of the MRI compatible microscope include an MRI compatible CCD camera (MRC HighResolution, MRC Systems GmbH), fluorescence excitation and imaging optics, and a custom 3D printed microscope body (**Fig. 3.1a, b**). In this section, we describe the optical components of the MRI compatible microscope, as well as the quality of data acquired through both BOLD fMRI and microscopy.

**Excitation pathway.** Light is delivered to the tissue through the excitation pathway of the microscope (**Fig. 3.1c**). Within the excitation pathway, 488 nm light is carried from an off-site laser (OBIS LX/LS Series, Coherent) to the microscope over a 4 meter long 400  $\mu\text{m}$  optical fiber (FP400ERT, Thorlabs). By using a laser that is located outside the MRI machine, we avoid the use of non-compatible electronics and materials such as LEDs inside the magnetic field.

After the light is emitted from the fiber tip, it is collimated using a 5 mm double convex lens (63-594-ink, Edmund Optics), and passed through a diffuser with a scatter angle of 10 degrees (edc-10, Rochester). This results in homogeneous excitation light with a gaussian distribution, which is combined with the optical path through a dichroic mirror (ET Dualband beam splitter FITC/CY3, AHF) before it is projected onto the brain surface.

**Emission pathway.** After excitation, the emitted fluorescence is collected by a custom objective consisting of three small diameter acrylic aspheric lenses (**Fig. 3.1c, d**; 17-271, Edmund Optics; 36-629, Edmund Optics). To minimize the vertical footprint of

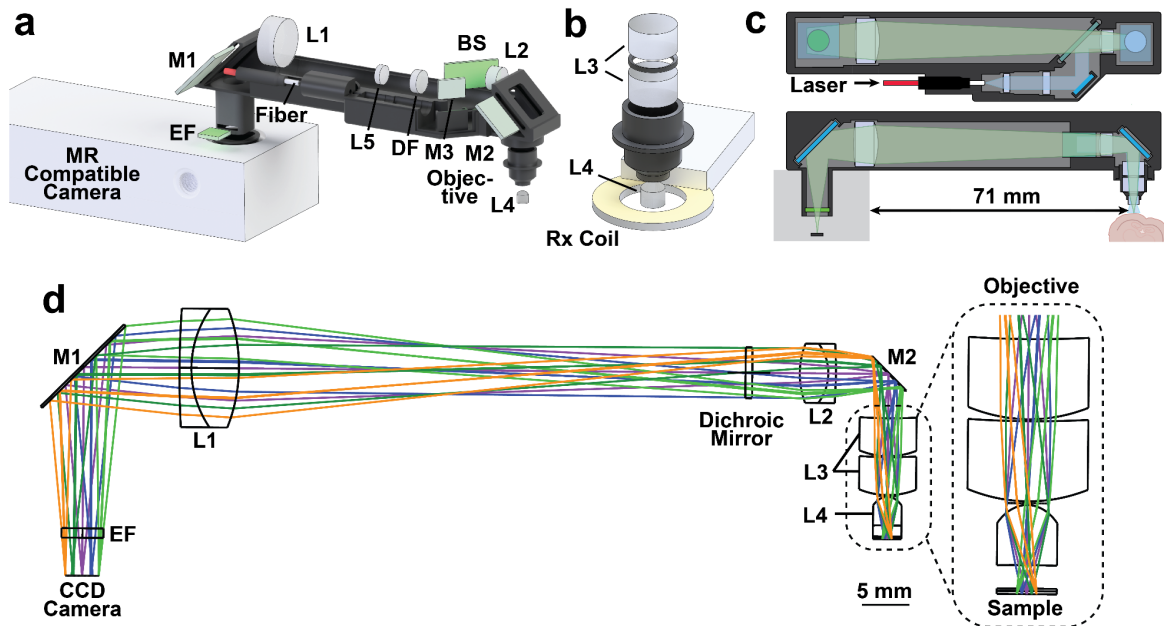


**Figure 3.1. Schematic of the MR compatible microscope** | a) CAD rendering of the MRI compatible microscope (left) and objective (right). Excitation light from an off-site laser is collimated with a double-convex lens (L5) and passed through a diffuser (DF). Fluorescent emission is collected by an objective consisting of three small diameter acrylic aspheric lenses (L3, L4). The collected light is relayed through two achromatic lenses (L1, L2), and projected onto the MRI compatible CCD camera through an emission filter (EF). b) Schematic of the excitation (blue) and emission (green) optical pathways. The distance between the CCD camera housing and the sample is 71.1 mm. c) BOLD EPI of a mouse brain (in situ) with and without optical components placed close to the Ca<sup>2+</sup> imaging site above the barrel cortex. From left to right: glass window only, acrylic lens, acrylic lens and HDT180 objective, BK7 objective lens, GRIN objective lens. d) Zemax simulation of the emission optical pathway. Fluorescent emission is collected by an objective consisting of three small diameter acrylic aspheric lenses (L3, L4). The collected light is relayed through two achromatic lenses (L1, L2), and projected onto the MRI compatible CCD camera through an emission filter (EF). BS = dichroic beamsplitter, DF = 10 degree scatter angle diffuser filter, EF = excitation filter, L1 = achromatic lens 1, L2 = achromatic lens 2, L3 = acrylic aspheric lenses, L4 = small diameter acrylic aspheric lens, L5 = 5 mm double convex lens, M1 = mirror 1, M2 = mirror 2.

the microscope, the optical path is diverted 90 degrees by a silver-plated mirror after the light passes through the objective (Fig. 3.1c, d; 350-700 nm imaging, AHF). Minimization of the vertical footprint was necessary due to the limited space of the MRI volume coil (70 mm diameter; RF RES 300 1H 089/072 QSN TR AD, BRUKER BioSpin MRI GmbH).

Along the horizontal axis, the lightpath is relayed by two achromatic lenses (47-690-INK, Edmund Optics; AC080.020, Thorlabs). A relay was essential to distance the camera from the gradient fields of the MRI machine due to the observed micron-sized shifts in camera position during gradient switching. The shifts resulted in the slow drift of the microscope with respect to the sample during MRI acquisition, and were caused by the susceptibility of the MRI compatible camera. To determine the optimal distance for the relay, we measured the minimal distance needed between the edge of the camera housing and the center of the gradient field (Fig. 3.2b). Results showed that a distance of  $d > 6$  cm was sufficient to avoid microscope displacement.

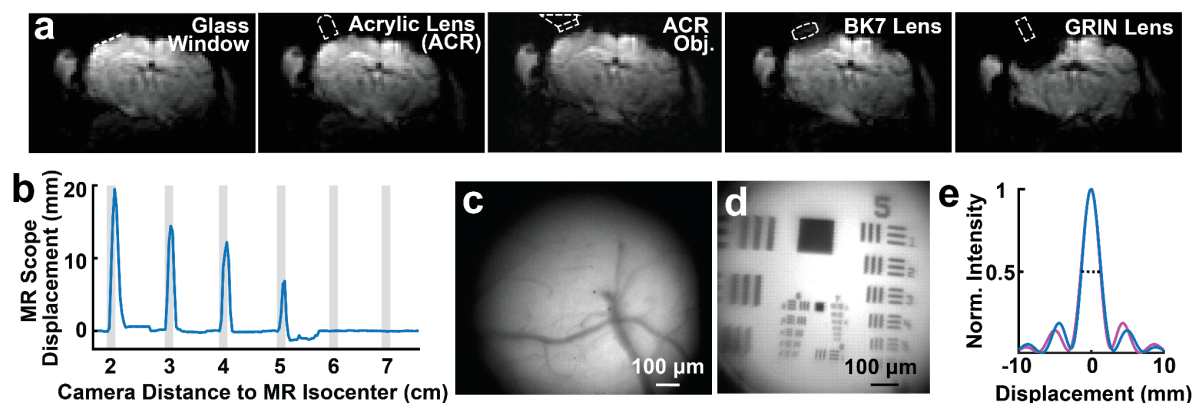


**Figure 3.2. Performance of the custom MR compatible objective | a)** BOLD EPI of a mouse brain (in situ) with and without optical components placed close to the Ca<sup>2+</sup> imaging site above the barrel cortex. From left to right: glass window only, acrylic lens, acrylic lens and HDT180 objective, BK7 objective lens, GRIN objective lens. **b)** Microscope displacement induced by RF excitation pulses with respect to the distance between the MRI compatible camera and the isocenter of the B<sub>0</sub> magnetic field. **c)** Example image of the cortex taken with the MR compatible microscope. **d)** Performance image taken with a resolution and distortion target (Thorlabs, R1L1S1P). **e)** Simulated optical resolution of the microscope with a full-width-half-maximum (FWHM, dashed line) of 2.5 micron.

After the relay, a second mirror was used to reflect the image downwards through an emission filter (ET Dualband Emitter FITC/CY3, AHF) onto the MRI compatible camera (MRC HighResolution, MRC Systems GmbH; 1280x960 pixels at 5.3 µm pitch).

**Custom MRI objective.** The main component responsible for possible distortions of the BOLD fMRI signal is the objective due to its spatial proximity to the tissue. To optimize the BOLD fMRI signal-to-noise ratio, we tested several objective designs to ensure homogeneity of the magnetic field and minimization of the magnetic susceptibility of the materials. The results showed that conventional borosilicate glass (BK7) and Gradient index (GRIN) lenses that are typically used in microscope objectives lead to artifacts in the BOLD fMRI signal, especially considering the large volume of the objective lenses used for our application (**Fig. 3.2a**; [84]). However, acrylic lenses showed no significant reduction in signal-to-noise ratio around the region of interest. By using acrylic lenses in the microscope objective (**Fig. 3.2a**; 17-271, Edmund Optics; 36-629, Edmund Optics), we were able to record microscopic fluorescent images with an acceptable resolution and field of view (**Fig. 3.2c-e**) inside the MRI scanner without compromising BOLD fMRI signal-to-noise ratio (**Fig. 3.2a**).

**Submersion.** The susceptibility border between air and tissue resulted in large signal void due to local field inhomogeneities around the implant. To resolve this issue, we added D<sub>2</sub>O as immersion media between the acrylic lens objective and the cortical window (**Fig. 3.2a, c**). D<sub>2</sub>O essentially increases the border between the brain and air, while not providing a signal during BOLD fMRI acquisition. The lack of signal stems from the fact that deuterium atoms have an additional neutron in the nucleus, which results in a different operating frequency for a given magnetic field strength. Because of the added D<sub>2</sub>O, the objective was redesigned as an immersion objective (**Fig. 3.1d**).

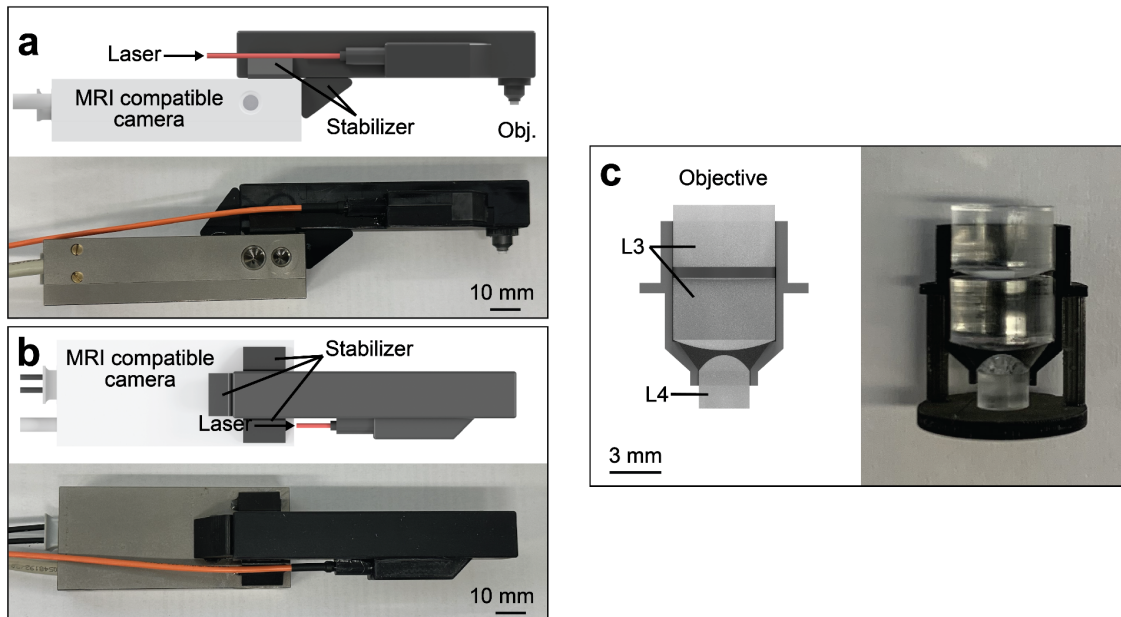


**Figure 3.3. Microscope dimensions and assembly** | a) Side view of the microscope. The stabilizers provided structural integrity along the long axis of the microscope. b) top view of the microscope. c) Cross-section of the microscope objective with acrylic lenses. L3 = acrylic aspheric lenses, L4 = small diameter acrylic aspheric lens.

**Cortical implant.** For the implant used in this thesis, the cortical window consists of a thin sheet of BK7 glass. Even though the previous results showed that BK7 has a magnetic susceptibility that does not match brain tissue, it is biocompatible, durable, and provides high optical clarity. To restrain the signal loss, we aligned the glass/brain interface with the B0 vector of the MRI scanner [54]. This results in the minimal artifact being restrained to only a few voxels close to the cortical window.

### 3.2 Mechanical design

Similar to the optical design, it is important that the materials used for the mechanical design of the microscope also avoid artifacts in the MRI acquisition. In this section we describe the structural design, manufacturing, and the material quality of the microscope body.

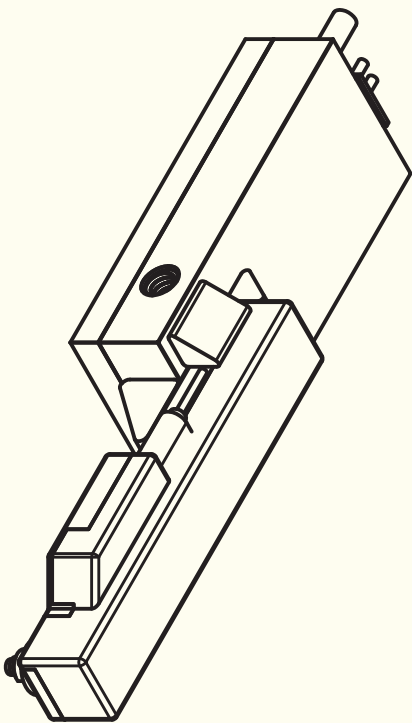
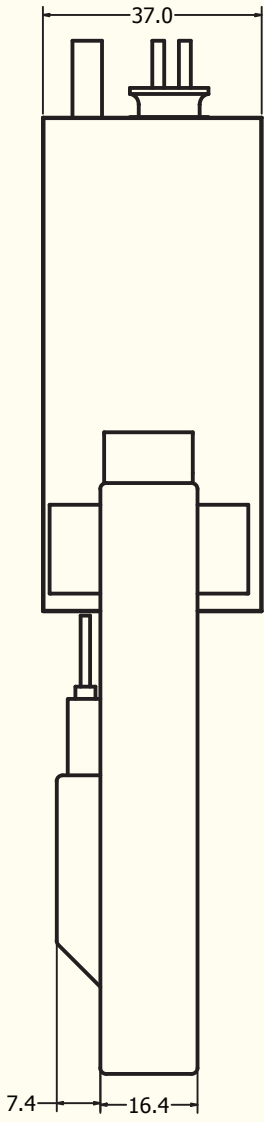
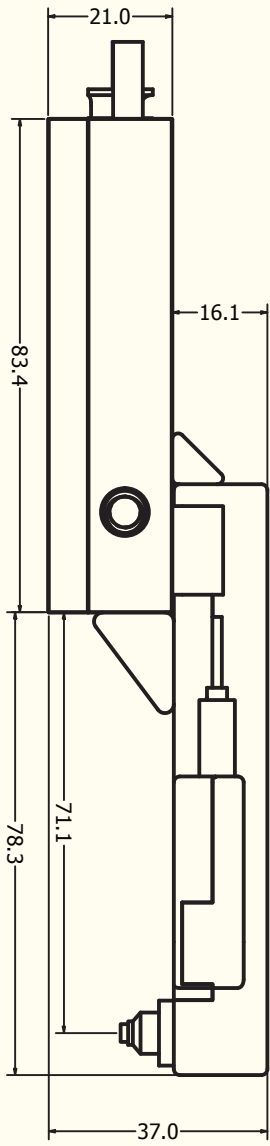
**3D printed microscope body.** All the optical elements were assembled in a custom 3D printed microscope housing (**Fig. 3.3a-c**). The emphasis of the design was on simplicity and modularity. The modular design allows for reparability, ease of use, and increases MRI precision of the production process as the complex geometry is broken down into multiple components.

To ensure a high signal-to-noise ratio of the BOLD fMRI signal, we conducted signal-to-noise ratio measurements using several 3D printed canisters produced from different materials (table 1). Results showed that a decrease in signal-to-noise ratio was mostly found in materials that had black additives. This is a common finding that

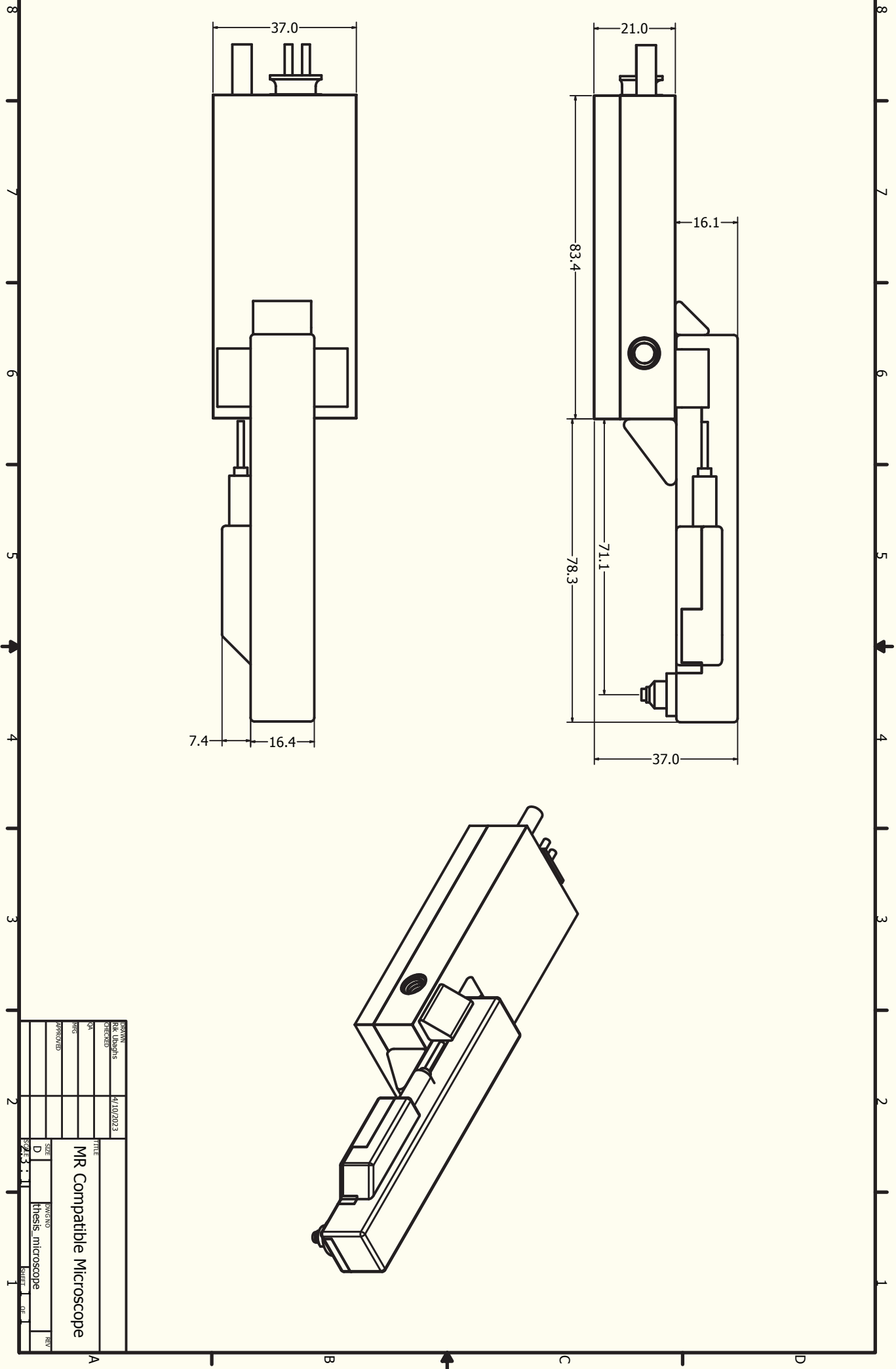
Material	Color	Additive Component	SNR	Artifact	Manufacturing procedure
PET	Transparent	No	11511	No	Fused Deposition Modeling
PEEK	Beige	No	10544	No	Fused Deposition Modeling
PETG	White	No	10526	No	Fused Deposition Modeling
PA12	White	No	10008	No	Selective Laser Sintering
PLA	White	No	9750	No	Fused Deposition Modeling
PEI	Beige	No	9539	No	Fused Deposition Modeling
PETG	Black	Black pigment	9407	No	Fused Deposition Modeling
HDT180	Black	Black pigment	9398	No	Digital Light Processing
Orthores	Transparent	No	9345	No	PolyJet
Veroclear	Transparent	No	9218	No	PolyJet
HDT60	Black	Black pigment	9140	No	Digital Light Processing

**Table 1** | Physical properties of the tested 3D printable materials.

stems from the magnetic susceptibility of the metallic black additives used in the resins. However, we were constrained in our alternatives due to the necessity of a black body to avoid the amount of stray light that enters the microscope. A second prerequisite of the resin was the temperature resistance to avoid warping due to the surface heating of the camera. Our tests showed that HDT180 provided the optimal tradeoff between signal-to-noise ratio, printer resolution, and heat-resistance (Table 1), and during experiments we found that HDT 180 performed well given our application. After production of the custom 3D printed housing (Table 1; Loctite 3D 3860 HDT180, Henkel; Objet 30 Pro, Stratasys; parts available at <https://github.com/rlemubaghs>), optics were assembled and fixed in place using low-staining optical glue (NOA61, Norland).



DRAWN	Rik Libarhis	4/10/2023	TITLE	MR Compatible Microscope
CHECKED			DATE	
QA			TEST	D
DATE			PROJECT	MR Compatible Microscope
APPROVED			SHEET	1
			REV	





---

## Chapter 4

### Combined microscope fMRI

To investigate the interaction between neural dynamics and the BOLD fMRI signal, we developed a novel paradigm that enabled us to measure simultaneous single-cell calcium activity and BOLD fMRI in awake animals. We used the MRI compatible microscope and behavioral setup described in previous chapters to measure calcium activity in layer 2/3 SSp-bfd neurons while simultaneously acquiring whole brain BOLD fMRI in awake mice. Measuring both sources of brain activity simultaneously allows us to explore the relationship between local neural activity and the vascular response, as well as the influence of brain-wide hemodynamics on the local neural activity.

In this chapter, we will first present results that establish our awake animal behavioral paradigm. Subsequently, we will demonstrate the strength of the combined microscope fMRI approach by exploring the brain across spatial scales. We will examine the interaction between individual cells in the SSp-bdf and the local BOLD fMRI response, as well as how the BOLD fMRI signal in different anatomical regions relates to the local neural activity in the SSp-bdf. Finally, we will show that the MRI compatible microscope can be used to measure genetically predefined inhibitory neural subpopulations, adding to the possible experimental questions that can be addressed with our combined microscope fMRI approach.

#### 4.1 Awake animal functional Magnetic Resonance Imaging

Awake animal MRI studies are accompanied by a variety of factors that complicate experimental procedures. These factors include animal movement, neuromodulatory factors, and animal stress levels. To avoid these confounding effects, animals used in this thesis were habituated using a rigorous behavioral protocol aimed at reducing stress levels in the animal. In this section we will first evaluate the performance of the habituation protocol used in this thesis. Subsequently, we will present findings that demonstrate the effectiveness of awake BOLD fMRI as a robust approach for investigating the hemodynamic activity across the brain.

**Animal habituation and behavioral performance.** Before the start of each experiment, animals were habituated using a rigorous behavioral protocol (for a detailed description of the habituation procedure, see **section 2.3.1**). To evaluate the effectiveness of the behavioral habituation, we evaluated the behavioral performance during each session by calculating the framewise displacement based on the six realignment parameters as described in **section 2.3.1**. Habituation was considered

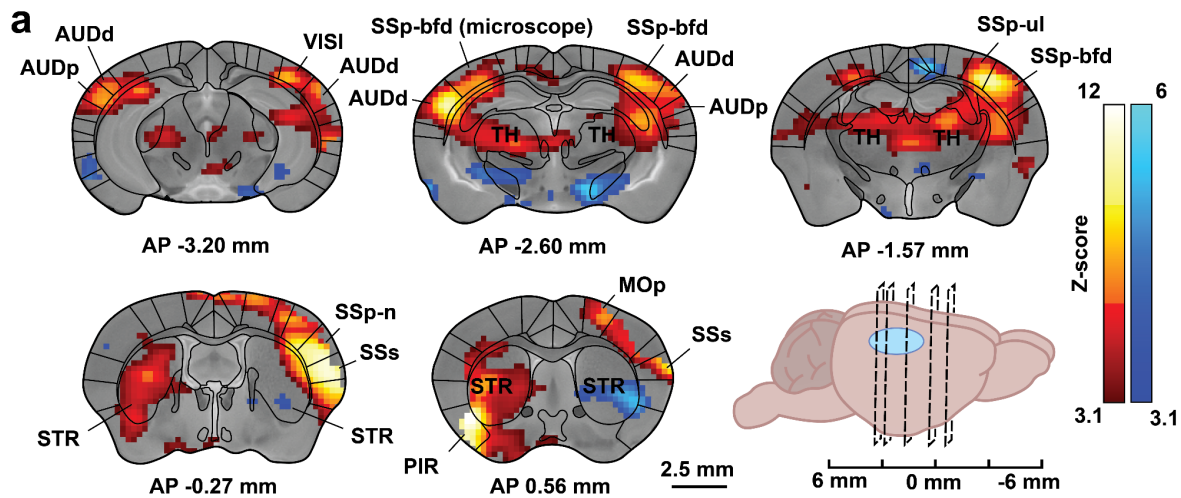


**Figure 4.1. General Linear Model based statistical map** | Statistical parametric map (Fixed effects, two-tailed t-test, z-score  $\geq 3.1$ , FWE  $P \leq 0.00001$ ,  $N = 6$ ) generated from the ge-EPI BOLD fMRI images acquired during contralateral whisker stimulation ( $N = 6$  subjects). Schematic (bottom right) shows the location of each frame relative to the cortical window. AUDd = dorsal auditory cortex, AUDp = primary auditory cortex, MOp = primary motor cortex, PIR = piriform cortex, SSp-bfd = somatosensory barrel fields, SSp-n = somatosensory orofacial domain, SSp-ul = somatosensory upper limb domain, SSs = secondary somatosensory area, STR = striatum, TH = thalamus, VISI = primary visual cortex.

successful when the average FWD for a full session was below 0.05 mm, and at least 50% of trials showed no excessive motion (FWD spikes  $> 0.075$  mm). Overall, the combination of the custom head constraint and habituation protocol resulted in low levels of head motion after habituation, and for the experimental sessions included in this thesis ( $0.0352 \pm 0.0106$  mm; mean  $\pm$  s.d.;  $N = 6$ ). Interestingly, most head movement occurred in the dorsal-ventral direction. This is most likely due to structural deficiencies in the design of the head constraint, with similar results being reported in other studies using awake animals [85].

**General Linear Model based statistical analysis.** Despite the general low levels of head motion, mice still displayed intermittent movement throughout the session. To control for unwanted variability in the functional scans, we used six motion realignment parameters (x, y, z displacement and roll, pitch, yaw) and the first derivatives as nuisance regressors in a conventional General Linear Model (GLM). The GLM based statistical analysis uncovered robust BOLD activations across cortical and subcortical structures in response to whisker stimulation (**Fig. 4.1**; z-score  $\geq 3.1$ , FWE  $P \leq 0.000001$ ,  $N = 6$ ). The main regions demonstrating BOLD activation included regions commonly involved in somatosensation such as the bilateral thalamus (TH), secondary somatosensory area (SSs), orofacial domains (SSp-n) and the whisker domains (SSp-bfd). The activated somatosensory areas have previously been implicated in natural whisking behavior and whisker stimulation using different experimental methods [86], confirming the validity of our findings in awake mice. In addition, we also observed activation of the striatum in response to whisker stimulation. Previous findings have proposed that the mouse striatum acts as a hub involved in the integration of different

sensory modalities [87], and is involved in the transformation of somatosensory information from the whiskers into motor activity [88].

Interestingly, our results also showed strong activation of auditory regions including the bilateral primary and dorsal auditory cortex (AUDp, AUDd). One possible explanation for the activation of the auditory regions is the noise generated by the pneumatic whisker stimulator. Even though the device was designed to avoid air displacement towards the mouse, the pressure of the compressed air in the pneumatic chamber caused an unavoidable audible sound during stimulation.

## 4.2 Combined microscopic calcium imaging and BOLD fMRI

In addition to BOLD fMRI, we simultaneously recorded the calcium activity of neurons in layer 2/3. Combining neuroimaging methods such as calcium imaging and BOLD fMRI can lead to better insights into brain functioning across spatial scales. In this section, we will demonstrate the feasibility of our combined microscope fMRI approach by providing experimental results about the interactions between brain activity across spatial scales. First, we will demonstrate the quality of the individual recording modalities by looking at the evoked potentials for both the neural and BOLD fMRI activity individually. Next, we will leverage the spatial component of the microscopic image to provide a novel interpretation about how the location of individual cells relative to the vasculature is related to the local hemodynamic response. Finally, we will demonstrate how the BOLD fMRI signal across different anatomically defined brain regions relates to the local neural activity in the SSp-bdf.

### 4.2.1 Neural and BOLD fMRI responses during whisker stimulation

To demonstrate the feasibility of the combined microscope fMRI approach, we will evaluate the signal quality and whisker stimulation evoked responses in the SSp-bdf from both recording methods. In this section, we will first examine the composition of recorded cells and their responsiveness to contralateral whisker stimulation. Subsequently, we will look at the evoked responses of the neural population and BOLD fMRI activity.

**Single cell calcium responses during whisker stimulation.** A total of 203 layer 2/3 SSp-bdf neurons ( $51 \pm 13$  per animal; mean  $\pm$  s.d.;  $N = 4$ ) were extracted from the MRI compatible microscope recordings. We were unable to extract cells from two animals leading us to exclude them from further analysis that involved neural activity. We first asked how the individual cells responded to stimulation of the contralateral whiskers (for example cells see **Fig. 4.2a, b**). To determine whether cells were responsive to the whisker stimulation, we averaged the individual trials to obtain the trial averaged whisker response ( $a(t)$ ). We then calculated the z-score over the full trial as:

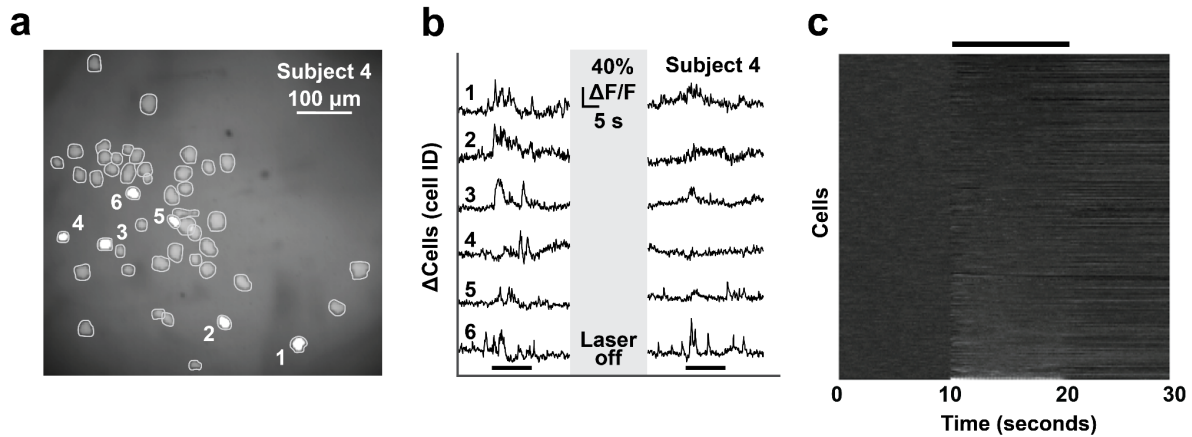


**Figure 4.2. Evoked responses of individual neurons** | a) Cell map showing 47 excitatory cells in layer 2/3 of the somatosensory barrel cortex (SSp-bfd). b) Example cell traces of the cells marked in a. c) Whisker stimulation evoked peri-stimulus time histogram (PSTH) for all extracted neurons in layer 2/3 of the SSp-bfd (4 animals; N = 203 cells). Results show that ~20% of cells have a positive response to contralateral whisker stimulation, while ~7% show a negative response.

$$z_{tone}(t) = \frac{a(t) - \mu_{bl}}{\sigma_{bl}}$$

where  $\mu_{bl}$  and  $\sigma_{bl}$  are the mean and standard deviation over the trial averaged baseline, defined as the 10 second period before whisker stimulation onset. A cell was deemed responsive to whisker stimulation when the average z-score during stimulation exceeded a threshold of 2 standard deviations or was below -2 standard deviations. We found that ~20% of cells responded positively to the contralateral whisker stimulation, while ~7% of cells showed a negative relationship (**Fig. 4.2c**). These results confirm the effectiveness of the used whisker stimulation paradigm, as well as provide evidence for the quality of the single cell neural responses measured with the MRI compatible microscope.

**Neural population and BOLD fMRI responses during whisker stimulation.** To evaluate the activity patterns of both modalities in response to whisker stimulation, we looked at the stimulus evoked potentials in the SSp-bfd. For the BOLD fMRI, we extracted the time series activity from voxels that showed significant activation during whisker stimulation within each animal (12 stimuli presentations, z-score  $\geq 3.1$ , FWE  $P \leq 0.000001$ , N = 6; **Suppl. Fig. 1**), and calculated the  $\Delta$ BOLD for each voxel as described in **section 2.4.1**. The  $\Delta$ BOLD time series for each voxel were then averaged, resulting in the SSp-bfd  $\Delta$ BOLD response for each animal. Results showed strong stimulus evoked potentials in the  $\Delta$ BOLD signal on both the individual and the group level (**Fig. 4.3a**). In addition, it became evident that the signal contains high amounts of variability between animals and trials. This variability is expected and can result from the quality of the surgical preparation, experimental setup tuning, residual variance due to motion, or animal mental state and attention [89]. Finally, the trial-averaged response showed a well defined hemodynamic response of ~4% signal change during

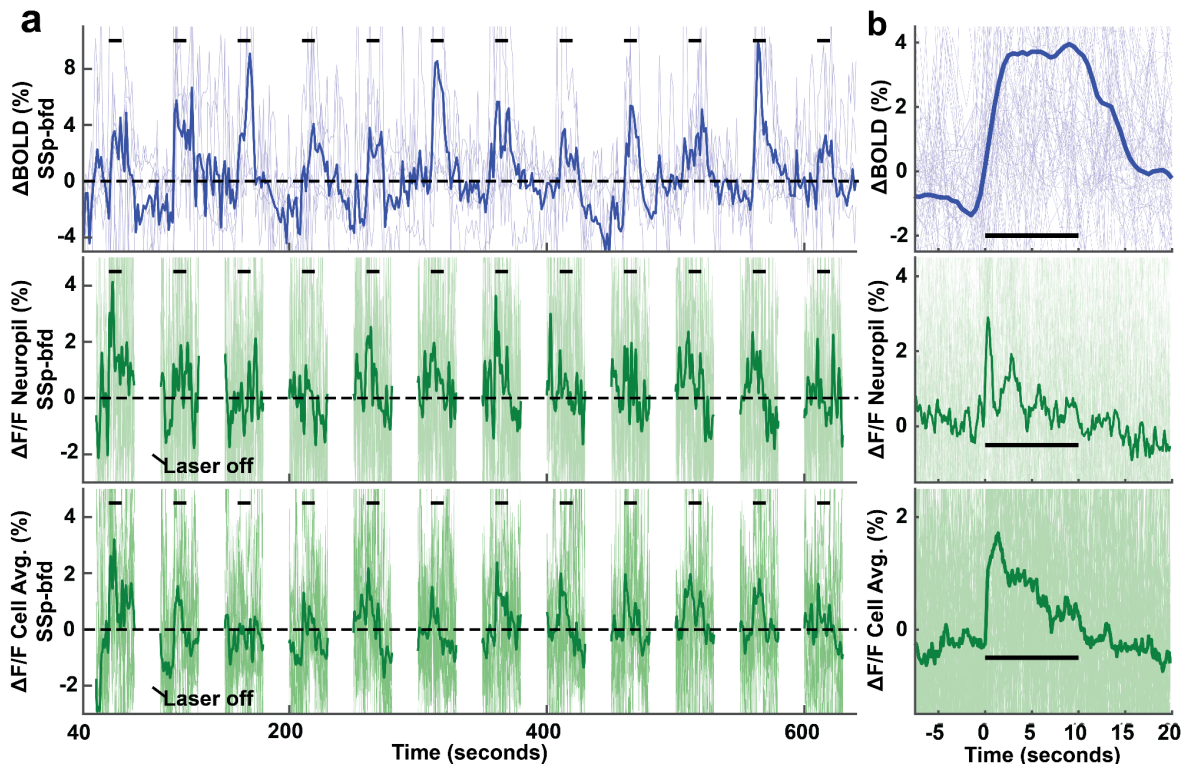


**Figure 4.3. Average stimulus evoked responses during a whisker stimulation task | a)** The  $\Delta$ BOLD fMRI whisker stimulation evoked time series in the contralateral SSp-bfd averaged over all significantly activated voxels (12 stimuli presentations; z-score  $\geq 3.1$ , FWE  $p < 0.000001$ ,  $N = 6$ ; left panel). The trial average within one animal is superimposed, with the average over all animals overlaid in thick blue. In addition, the average over all trials and animals is shown on the right. **b)** The  $\Delta$ F/F calcium activity time series in the contralateral SSp-bfd averaged over all cells within the imaged neural population (12 stimuli presentations;  $N = 4$ ; left panel). The trial average within one animal is superimposed, with the average over all animals overlaid in thick green. The average over all trials and animals is shown on the right. **b)** The  $\Delta$ F/F calcium activity time series in the contralateral SSp-bfd for the background activity (neuropil; 12 stimuli presentations;  $N = 4$ ; left panel). The trial average within one animal is superimposed, with the average over all animals overlaid in thick green. The average over all trials and animals is shown on the right.

contralateral whisker stimulation, which is in line with previous studies using a similar paradigm [54].

A similar methodology was used for the neural calcium activity. Here, we used CNMF-E [82] to extract both the  $\Delta$ F/F calcium activity for each individual cell, as well as the overall background signal (neuropil). For the individual cells, all time series were averaged resulting in one population activity vector per animal. For both the  $\Delta$ F/F population and neuropil signal we observed a strong stimulus evoked potential on the subject level and for the trial averaged time series (**Fig. 4.3b, c**;  $N = 4$ ). In contrast to the  $\Delta$ BOLD signal, the neural activity shows higher levels of noise around the average. This can be explained by the high sampling rate of calcium imaging, as well as certain measurement parameters of the MRI compatible camera (low quantum efficacy, high pixel-level quantum noise). In addition, the relatively high noise in the neuropil as compared to the cellular signal can result from the sparse expression of calcium indicators in our transgenic animal model [62]. This strategy is commonly used to

increase the signal-to-noise ratio of cellular recordings by decreasing background contamination. However, the lower calcium indicator levels in the peripheral neural tissue might also lead to the decrease in the neuropil signal in our results.

#### 4.2.2 Local interactions between SSp-bdf neurons and BOLD fMRI

The integration of microscopy and fMRI can lead to a deeper insight into the interactions between local neural activity and the BOLD fMRI response. One distinct advantage of microscopy is the possibility of including spatial information about the neural activity. Including a spatial component can add context to the local activity by providing information about neuron location, vasculature composition, and the spatial arrangement between both. In this section, we will look at how the local neural activity contributes to the formation of the BOLD fMRI response in the SSp-bdf. Subsequently, we will take advantage of the spatial component of our neural calcium recordings by investigating the relationship between neuron location and the local hemodynamic response.

**Contribution of neural activity to the local BOLD fMRI response.** We used a decoding approach based on support vector machines (SVMs) to quantify the predictive information of the local neural population with respect to the BOLD fMRI signal. For this purpose, we trained linear epsilon-insensitive SVM regression decoders for each individual mouse. Our predictive features consisted of the  $\Delta F/F$  calcium activity vectors of each individual neuron, while the average  $\Delta BOLD$  fMRI signal in the SSp-bdf constituted the dependent variable (**Fig. 4.4a**).

Due to the difference in temporal sampling rate between calcium imaging and BOLD fMRI, we used linear interpolation to increase the data points of the  $\Delta BOLD$  fMRI signal to match the 100 ms acquisition interval of the  $\Delta F/F$  calcium activity. In addition, certain periods of the calcium imaging recordings did not contain a fluorescent signal as a result of the excitation laser deactivation between stimulus presentations (**section 2.2.2**). To ensure the alignment, deactivation periods were removed from both the  $\Delta BOLD$  and  $\Delta F/F$  calcium imaging activity.

We then used the decoding performance as a measure of explained information by the local neural population. The decoding performance was quantified by the Root Mean Square Error (RMSE) according to:

$$RMSE = \sqrt{\frac{\sum_{i=1}^N (x_i - \hat{x}_i)^2}{N}}$$

where  $x_i$  is the observed  $\Delta BOLD$  fMRI time series and  $\hat{x}_i$  the estimated  $\Delta BOLD$  fMRI time series. Subsequently, the RMSE was normalized by the standard deviation ( $\sigma_x$ ) in order to compare error levels between animals:

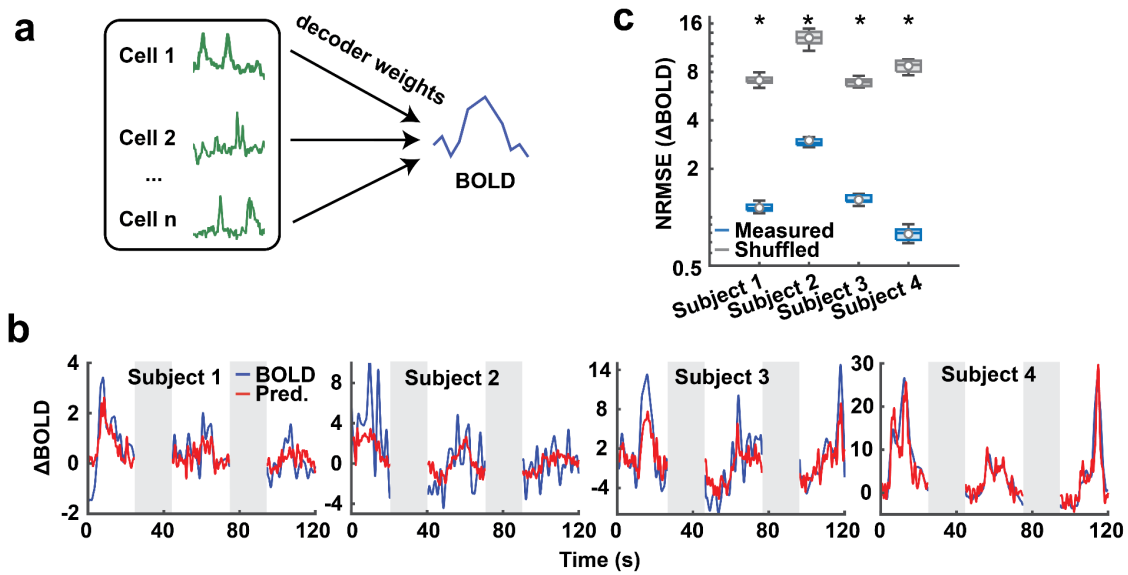


**Figure 4.4. Neural-BOLD decoding approach** | a) Schematic of the support vector machines (SVMs) decoding approach used to quantify the predictive information of the local neural population with respect to the BOLD fMRI signal. SVM regression models were trained for each individual mouse using the  $\Delta F/F$  calcium activity vectors of individual neurons as predictive features, and the average  $\Delta$ BOLD fMRI signal in the SSp-bfd as observed responses. b) Example predictions of the decoding approach for the  $\Delta$ BOLD fMRI signal in the SSp-bfd for each subject. Gray boxes indicate laser-off period. c) The normalized root mean square error (NRMSE) between the measured and predicted  $\Delta$ BOLD fMRI signal. Boxplots show the NRMSE of the ten times cross validated outcomes for each animal. The central line represents the median, the circle represents the mean. The minimum and maximum of the box extend to the 25th and 75th percentiles, whiskers extend to all data points. We tested the difference in performance between measured and shuffled data using a two-sample t-test ( $P \leq 0.0001$ ).

$$NRMSE = \frac{RMSE}{\sigma_x}$$

To estimate the baseline model for the collected data, we repeated the previous procedure with temporally permuted neural training data. This process was repeated ten times for each animal, and results showed that the NRMSE between the observed data and the prediction from the baseline model was similar across mice ( $8.9 \pm 2.3 \Delta$ BOLD).

Overall, the neural activity for all four mice predicted the local  $\Delta$ BOLD fMRI signal accurately, with the NRMSE of all predicted responses falling well below the baseline model (**Fig. 4.4b, c**). This demonstrates the validity of the decoding approach, and confirms that the local neural population activity contains information relevant to the local BOLD fMRI signal in all animals.

**Spatial organization of neurons and the hemodynamic response.** Next, we leveraged the spatial component of our neural calcium recordings to further disentangle the predictive relationship between the local neural activity and BOLD fMRI. The spatial component provides additional information about the neuron location, vasculature composition, and the spatial arrangement between both. In this section, we used the

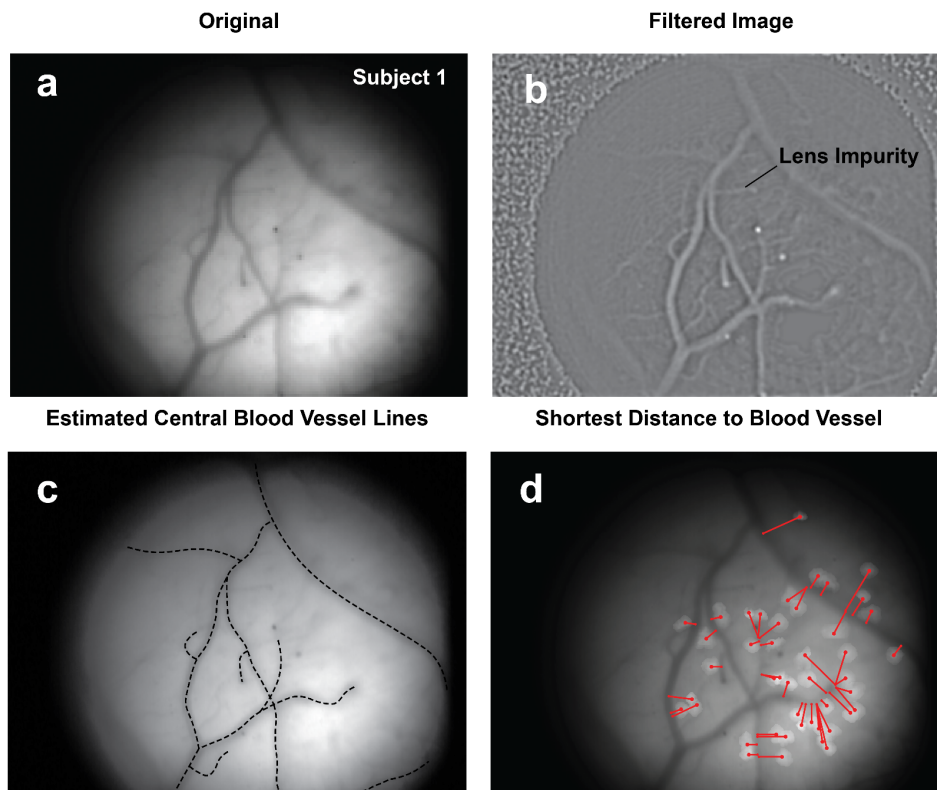


**Figure 4.5. Bloodvessel pattern estimation** | **a)** The average microscope image over the full experimental session. **b)** The band pass filtered (100-150 Hz) average microscope image used to improve the visibility of the vascular structures. Notice that the lens impurities are amplified by the filtering procedure. **c)** the annotated bloodvessel structure superimposed on the average microscope image. Special care was taken to exclude features that were not part of the bloodvessel formation. **d)** The estimated Euclidean distance between the center of the cell and the vascular structure for all cells in the field of view.

discrete distance between individual neurons and the local vasculature to explore the influence of neural-vascular proximity on the predictive power of each neuron.

To estimate the proximity of neurons to the vasculature, we manually annotated the bloodvessel patterns over the time averaged microscopic field for each animal (**Fig. 4.5**; for individual annotations, see **Suppl. Fig. 2**). In addition to the microscopic field, we used a band pass filter (100-150 Hz) to improve the visibility of the vascular structures. However, the filtered images also included exaggerated lens impurities that resembled blood vessels (**Fig. 4.5**). Special care was taken to exclude features that were not part of the blood vessel formation. All annotations were validated by two additional researchers.

Next, we estimated the Euclidean distance between the center of the cell and the vascular structure via:

$$d(p, q) = \sqrt{\sum_{i=1}^n (q_i - p_i)^2}$$



---

where  $p$  and  $q$  are two points in Euclidean  $n$ -space (**Fig. 4.5**). Note that this description of the Euclidean distance is restricted to a two dimensional field due to the limited capacity of single-photon microscopy to resolve depth. Finally, we used the minimal distance value for each individual neuron to determine the neuron-vascular proximity metric.

To investigate the effect of neuron location in predicting the local BOLD fMRI signal, we compared the orthogonal distance between each neuron and the vascular structure to the predictive power of each neuron. (**Fig. 4.6a**). In SVM regression, the  $\beta$ -weights represent the coefficients assigned to each feature during optimization, and can be used to create a linear function that maps the predictors to the observed target variable. The magnitude of the  $\beta$ -weights indicates the strength and direction of the relationship between the predicting features and the target variable. Larger absolute values of the  $\beta$ -weights indicate that the corresponding features have a stronger influence on the target variable, while smaller beta weights have a weaker influence. By combining the  $\beta$ -weights and the neuron-vascular proximity, we were able to evaluate the relative contribution of individual neurons to the  $\Delta$ BOLD fMRI signal based on their position with respect to the vasculature. To achieve this, we used SVM recurrent feature elimination (SVM-RFE) to rank each neuron based on their predictive information, and compared three ranking criteria: lowest absolute decoder weight elimination, lowest decoder weight elimination, and highest decoder weight elimination. SVM-RFE uses the weight magnitude as a ranking criteria to remove less important features recursively, providing a subset of features that achieve the highest performance. First, an SVM regression model is trained using all available features. The resulting  $\beta$ -weights are then ranked based on a predefined criterion. The feature with the lowest ranking is eliminated, and given the lowest remaining rank. This process is then repeated without the eliminated feature until all features have received a ranking.

Here, we use three criteria yielding three distinct rankings. 1) Lowest absolute decoder weight elimination. Weights are ranked based on the absolute  $\beta$ -weights, and the lowest value is iteratively removed. This procedure does not take into account the sign of the assigned  $\beta$ -weights, providing both positive and negative  $\beta$ -weights an equal chance at receiving a high ranking. 2) Lowest decoder weight elimination. Weights are ranked based on the magnitude of the  $\beta$ -weights, and the lowest value is iteratively removed. This procedure results in a higher chance for  $\beta$ -weights with a positive value to receive a high ranking. 3) Highest decoder weight elimination. Weights are ranked based on the magnitude of the  $\beta$ -weights, and the highest value is iteratively removed. This procedure results in a higher chance for  $\beta$ -weights with a negative value to receive a high ranking.

To assess the influence of the neuron-vascular proximity on  $\Delta$ BOLD fMRI prediction, we quantized the proximity values within each animal based on the ranking of the  $\beta$ -weights for each ranking criteria. We find no difference in spatial location as

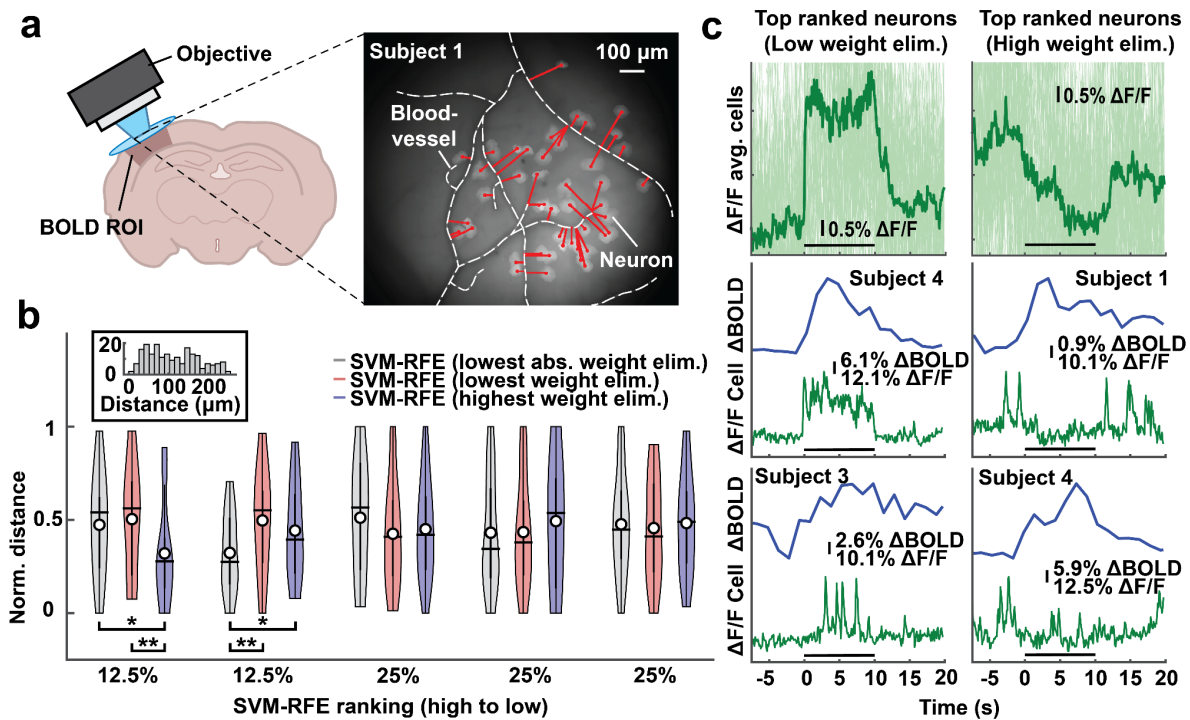


**Figure 4.6. Spatial organization of neurons influence the hemodynamic response** | a) Schematic of the experimental setting (left). Bloodvessel patterns (right) were manually annotated for each animal, and the neuron-vascular proximity was defined as the Euclidean 2-dimensional distance between the center of each neuron and the nearest point on the bloodvessel. b) The neuron-vascular proximity measures, quantized based on the SVM decoding procedure in a. Features were ranked using recurrent feature elimination (see methods) using three individual ranking criteria (highest weights elimination, lowest weights elimination, and lowest absolute weight elimination). The central line represents the median, the circle represents the mean. The bold whisker extends to the 25th and 75th percentiles, the fine whisker extends to all data points. The width of the plot is proportional to the number of data points with the corresponding value. We tested for the difference between the distance values within each quantile using a two-sample *t*-test (\*\* =  $P \leq 0.05$ ; \* =  $P \leq 0.1$ ). No correction for multiple comparisons was applied. Inset: distance histogram of all neurons. c) Trial average  $\Delta\text{F/F}$  Ca<sup>2+</sup> activity of the 12.5% highest ranked cells (top) for two ranking criteria (lowest weights elimination, left; highest weights elimination, right), and example  $\Delta\text{BOLD}$  fMRI and  $\Delta\text{F/F}$  single-cell Ca<sup>2+</sup> activity for both ranking criteria.

compared to the whole population when neurons were ranked using the magnitude of the decoder weight (lowest absolute decoder weight elimination; **Fig. 4.6b**). However, including the sign of the decoder weights in the ranking criteria revealed two distinct populations of cells that were different in their location and activity pattern (**Fig. 4.6c**). We found that neurons with a strong response to contralateral whisker stimulation were exclusively assigned positive decoder weights (lowest decoder weight elimination; **Fig. 4.6b**; left), and showed a heterogeneous pattern in their distance from the vasculature that did not differ from the overall distribution (**Fig. 4.6b**; two-tailed *t*-test,  $P = 0.363$ ). In contrast, a second subpopulation of neurons that was characterized by negative decoder weights (highest decoder weight elimination) showed a decreased response during whisker stimulation (**Fig. 4.6b**; right). Interestingly, this population was located significantly closer to the vascular structure as compared to the whole population (**Fig. 4.6b**; two-tailed *t*-test,  $P = 0.015$ ).

---

Together these findings demonstrate that layer 2/3 neurons located closer to the vasculature, have a different relationship to the BOLD fMRI signal as compared to other neurons in the field of view. In addition, by showing that neural-vascular proximity contributes to the BOLD fMRI signal, we demonstrated that adding spatial context in BOLD fMRI experiments can provide a more detailed explanation of the neural activity underlying the hemodynamic response.

### 4.2.3 The influence of global hemodynamics on the local neural response

Regions across the brain can influence local neural activity through direct and indirect afferent connections. To understand the complex interactions between different anatomical regions, it is important to measure activity with adequate spatial coverage. Combined microscope fMRI enables the simultaneous measuring of local neural activity at high spatiotemporal resolution and whole brain hemodynamic activity. This approach can provide a new perspective on neural processing by enabling the comparison between activity patterns across different spatial scales of the brain in a behaving animal. In this section, we will first evaluate whether the BOLD fMRI signal in the SSp-bfd contains predictive information about the simultaneously imaged local excitatory calcium activity. And second, we will extend this approach to include different anatomical regions involved in whisker stimulation.

**Predictive information in the SSp-bfd BOLD fMRI with respect to local neural activity.** To quantify the predictive information of the SSp-bfd  $\Delta$ BOLD fMRI activity with respect to the local neural activity, we used a similar decoding approach as described in **section 4.2.2**. The predictive features consisted of the first 13 components extracted through principal component analysis (PCA) over the significantly activated voxels in the SSp-bfd ( $z$ -score  $\geq 3.1$ , FWE  $P \leq 0.000001$ ). We used PCA to decrease the number of dimensions to avoid overfitting due to the high number of significantly activated voxels in the SSp-bfd, and found that the first 13 components were sufficient to explain  $\geq 90\%$  of the variance. The dependent variable was composed of the  $\Delta F/F$  neural population calcium activity lowpass filtered at 0.01 Hz (**Fig. 4.7a**). To estimate the baseline model for the collected data, we repeated the previous procedure with temporally permuted  $\Delta$ BOLD training data. This process was repeated and averaged over ten times for each animal, and results showed that the NRMSE of the baseline model was similar across mice ( $17.7 \pm 6.9 \Delta F/F$  cellular response). Note that the fMRI voxels of the SSp-bfd span a larger area than the imaged neural population, meaning that the information available for the decoding approach is not limited to the  $\Delta$ BOLD response local to the neural data.

Overall, our results show that the local  $\Delta$ BOLD fMRI signal is a good predictor of the neural population activity in the SSp-bfd, with the NRMSE of all predicted responses falling well below the temporally shuffled baseline model (**Fig. 4.7b**;  $P \leq 0.0001$ ). This

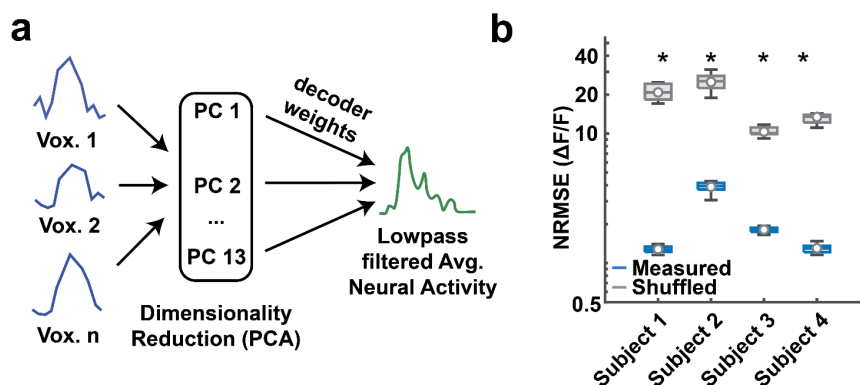


**Figure 4.7. BOLD-neural decoding approach** | a) Schematic of the SVM decoding approach to predict the BOLD fMRI signal of the barrel fields (SSp-bfd) from the local SSp-bfd Ca<sup>2+</sup> population activity. b) Normalized root mean square error (NRMSE) between the measured and predicted  $\Delta F/F$  population activity. Boxplots show the NRMSE of the ten times cross validated outcomes for each animal. The central line represents the median, the circle represents the mean. The minimum and maximum of the box extend to the 25th and 75th percentiles, whiskers extend to all data points. We tested for the difference between the measured and shuffled data using a two-sample t-test (\* =  $P \leq 0.0001$ ).

demonstrates the validity of the decoding approach, and confirms that the  $\Delta$ BOLD fMRI contains information relevant to the neural calcium signal at the single subject level.

**Regional BOLD fMRI across the brain contains predictive information about SSp-bfd neural activity.** Next, we applied the same approach to different anatomical regions implicated in the whisker stimulation paradigm by the GLM statistical analysis described in **section 4.1**. We used the first 13 principal components over the  $\Delta$ BOLD of significantly activated voxels ( $z$ -score  $\geq 3.1$ , FWE  $P \leq 0.000001$ ) in each anatomical region as training data to predict the average  $\Delta F/F$  neural response for the cell population activity. In addition, we included bidirectional time delayed  $\Delta$ BOLD activity traces (-1, 0.5, 0, 0.5, and 1 second) to ensure that vascular information from anatomically connected afferent and efferent regions was fairly represented within the training set.

The anatomical regions exhibited substantial variations in the amount of activated voxels due to heterogeneous region sizes and the extent of involvement in whisker stimulation. To avoid overestimation of the information contained within larger anatomical regions, we subsampled the voxels within each anatomical region by randomly selecting fifty voxels to include in the PCA-based feature extraction. We repeated this procedure ten times for each anatomical region and averaged the results to get the average performance for each mouse.

In addition to anatomical regions associated with whisker stimulation, we added the background and global  $\Delta$ BOLD fMRI signal. The background signal consisted of activity from voxels that did not contain brain related  $\Delta$ BOLD signals, and allowed us to determine the extent to which scanner noise and preprocessing artifacts contributed to the results from the decoding approach. In contrast, the global signal was composed through the same method as other anatomical brain regions, except the chosen voxels

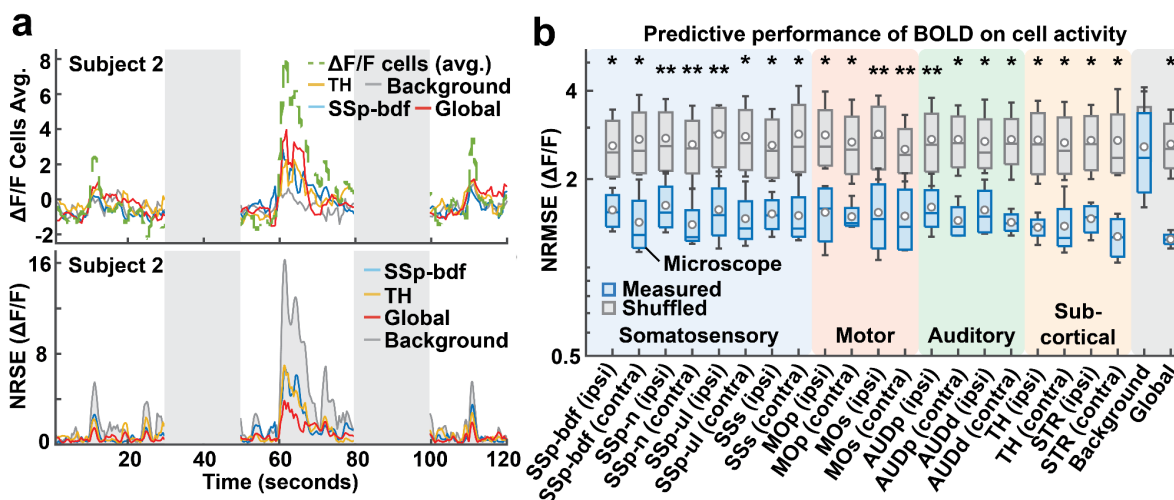


**Figure 4.8. BOLD-neural decoding approach for multiple anatomical regions | a)** Example predictions of the SSp-bfd  $\Delta F/F$  population activity (upper) and corresponding normalized root square error (below; NRSE) for different brain areas and background noise. Gray boxes indicate laser-off period. SSp-bfd = somatosensory barrel fields, TH = thalamus. **b)** NRMSE between the  $\Delta F/F$  and predicted  $\Delta F/F$  population activity for areas involved in whisker stimulation. Boxplots show the NRMSE from all animals. The minimum and maximum of the box extend to the 25th and 75th percentiles, whiskers extend to all data points. We tested the difference in performance between measured and shuffled data using a Wilcoxon rank-sum test (\* =  $P \leq 0.1$ ; \*\* =  $P \leq 0.05$ ). AUDd = dorsal auditory cortex, AUDp = primary auditory cortex, MOp = primary motor cortex, MOs = secondary motor cortex, SSp-bfd = somatosensory barrel fields, SSp-n = somatosensory orofacial domain, SSp-ul = somatosensory upper limb domain, SSs = secondary somatosensory area, STR = striatum, TH = thalamus. Contralateral and ipsilateral indicated with respect to the whisker stimulation.

were not limited to one region. The global signal can be interpreted as a measurement of the total amount of information contained within the brain about neural activity in the SSp-bfd. Finally, we estimated the baseline model for each anatomical region by repeating the decoding procedure with temporally permuted  $\Delta BOLD$  training data. This process was repeated ten times and averaged for each animal.

Our results show that the BOLD-neural decoding approach accurately predicts the local neural population activity from the  $\Delta BOLD$  signal of anatomically defined regions involved in whisker stimulation (**Fig. 4.8a, b**). As expected, the background performs worse than the  $\Delta BOLD$  from anatomical regions involved in whisker stimulation.

Next, we visualized the predictive information for the  $\Delta BOLD$  in relation to the neural population activity through a magnitude map based on the NRMSE (**Fig. 4.9**). As expected, we saw a strong laterality effect for anatomical regions involved in whisker stimulation, which is consistent with previous findings of the mouse whisker system [90], [91]. Interestingly, we found that the bilateral primary motor cortex (MOp) were good predictors of the neural population activity in the SSp-bfd. Connections between the SSp-bfd and MOp have previously been reported [90], and could play a role in whisking behavior because somatosensory input is often the result of self-generated movement, and conversely, is used to refine motor control. Finally, we observed a strong predictive relationship between the striatum (STR) and SSp-bfd  $\Delta F/F$  population

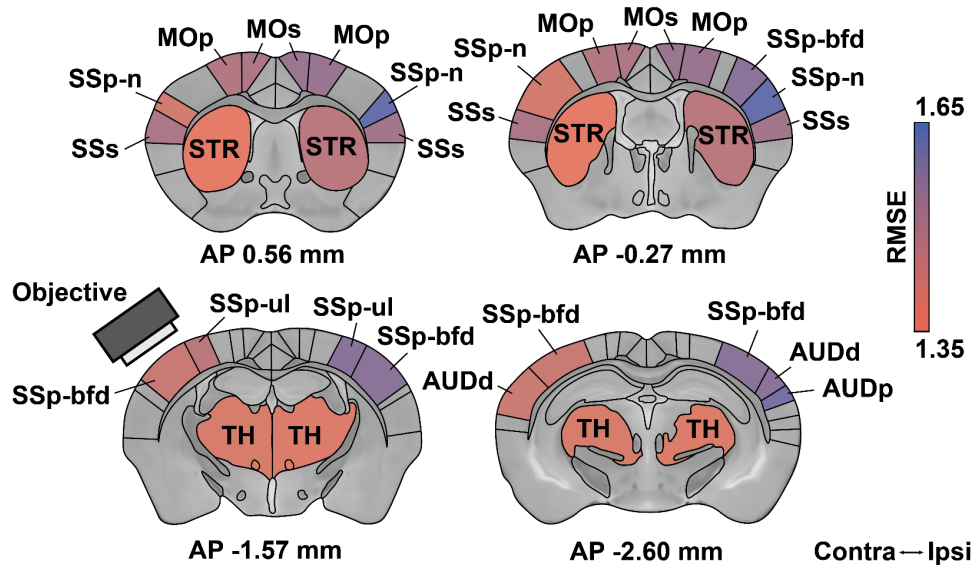


**Figure 4.9. NRMSE magnitude map for whisker stimulation** | Visualized representation of the predictive information of the  $\Delta$ BOLD in relation to the neural population activity through a magnitude map based on the NRMSE. We included the main areas involved in the whisker stimulation paradigm implicated by the GLM based statistical analysis described in section 4.1. Results show that properties such as laterality and connectivity, can be reconstructed through combined microscope fMRI. Contralateral  $\leftrightarrow$  ipsilateral indicated with respect to the whisker stimulation. MOp = primary motor cortex, PIR = piriform cortex, SSp-bfd = barrel fields, SSp-n = orofacial domain, SSp-ul = upper limb, SSs = secondary somatosensory area, STR = striatum, TH = thalamus.

activity. This was in agreement with the strong activation we found through GLM based statistical analysis (**section 4.1**). Previous findings have proposed that the mouse STR acts as a sensory hub involved in the sensory integration of different modalities [87], which receives projections directly from layer 2/3 neurons in the SSp-bfd [92]. This could explain the high predictive relationship between the  $\Delta$ BOLD signal and neural population activity in the SSp-bfd.

Together these results provide evidence for the use of combined microscope fMRI in exploring cross-scale brain activity. We demonstrated that different cortical and subcortical regions contain information that can be used to predict neural activity in the SSp-bfd. In addition, we showed that properties of the whisker system, such as laterality and connectivity, can be reconstructed through combined microscope fMRI.

### 4.3 Single neuron microscopy and cell specificity

Calcium imaging allows researchers to tag and record specific neural subtypes through genetic targeting strategies (**section 1.5.2**), allowing for a more comprehensive understanding of neural circuit activity. By combining calcium imaging with BOLD fMRI, researchers could take advantage of the same strategies to gain a better understanding of the role of heterogeneous neural population activity in shaping the hemodynamic response. Throughout this chapter we have demonstrated that combined microscope fMRI is possible in layer 2/3 excitatory neurons. Conversely, in this section

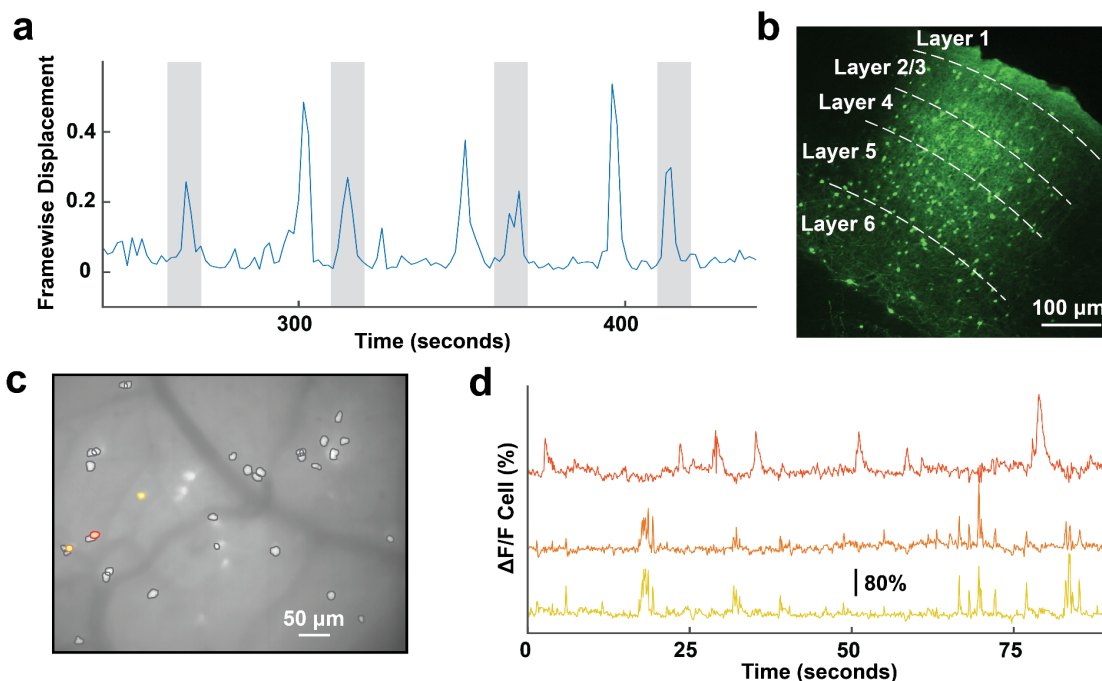


**Figure 4.10. Somatostatin positive imaging using microscope fMRI** | a) Example framewise displacement (FWD) of a Somatostatin-IRES-Cre mouse after habituation described in section 2.3 (average FWD = 0.0589 mm, N = 1). Note that most of the movement occurred during trials, resulting in BOLD fMRI data that did not meet the quality standards described in section 2.3.1. b) Anatomical brain slice of the somatosensory barrel cortex (SSp-bfd) showed that the distribution of the transfected cells spanned all layers of the cortex, with a large proportion residing in layer four and five. c) Cell map showing 33 inhibitory somatostatin positive cells in the SSp-bfd. d) Example cell traces of the cells marked in c.

we will demonstrate the feasibility of combined microscope fMRI studies using a genetically modified mouse strain that expresses a calcium indicator in Somatostatin positive inhibitory neurons.

**Animal habituation and behavioral performance.** Somatostatin-IRES-Cre mice were habituated using the same protocol described in **section 2.3.1**. Throughout the handling procedures, we observed no discernable signs of stress. However, animals exhibited high levels of motion during head restraint as compared to the layer 2/3 mice used previously (framewise displacement =  $0.0420 \pm 0.0147$  mm; mean  $\pm$  s.d.; N = 3). Although the average motion was below the recommended threshold for BOLD fMRI recordings, we noted that most of the movement occurred during trials, resulting in BOLD fMRI data that did not meet the quality standards described in **section 2.3.1** (**Fig. 4.10a**).

**Calcium dynamics of Somatostatin positive neurons.** To assess whether the signal-to-noise ratio of somatostatin positive neurons in the SSp-bfd was sufficient to extract cells from the MRI compatible microscope recordings, we imaged three somatostatin-IRES-Cre animals expressing GCaMP8s in somatostatin positive neurons during rest. From the recordings, we were able to extract a total of 48 somatostatin positive neurons in the SSp-bfd (**Fig. 4.10c, d**;  $16 \pm 14.6$  per animal; mean  $\pm$  s.d.; N =

3). The yield was noticeably lower than previous recordings in animals expressing GCaMP in layer 2/3 excitatory neurons. This finding is common due to the lower number of somatostatin positive cells present in the cortex [93], [94]. In addition, anatomical results showed that the distribution of the transfected cells spanned all layers of the cortex, with a large proportion residing in layer four and five (**Fig. 4.10b**) [94]. This could mean that the limited depth of focus of the MRI compatible microscope (for a detailed description, please refer to chapter 3) might not reach a large proportion of the targeted cells.

Even though somatostatin-IRES-Cre mice did not meet the behavioral criteria, the obtained results demonstrate the feasibility of using genetic strategies to target different neural subtypes in combined microscope fMRI studies. In the future, researchers could use combined microscope fMRI to improve our understanding of the specific functional contributions of genetically-defined cell populations in the hemodynamic response.



## Chapter 5

### General discussion

In this thesis we explored the relationship between neural activity and brain hemodynamics by investigating the relationship between single-neuron calcium dynamics and BOLD fMRI. To this end, we designed a novel MRI compatible microscope to record the calcium activity of layer 2/3 neurons in the SSp-bfd, while simultaneously measuring the whole brain BOLD fMRI response. These measurements allowed us to explore both the local relationship between neural activity and the hemodynamic response in the SSp-bfd, as well as the interaction between brain-wide hemodynamics and the neural activity in the SSp-bfd. In the following chapter, we will position the results outlined in the previous chapter within the broader context of neuroimaging research. Furthermore, we will evaluate the promises and limitations of combined microscope fMRI research, and provide an outlook for the future.

#### 5.1 Brain interactions across scales in awake animals

**Awake animal fMRI.** During BOLD fMRI experiments, animals are often anesthetized to prevent motion artifacts and stress [95]. However, the use of anesthetics affects both brain functioning and blood flow within the brain [96]. This can lead to issues in the interpretation of the results, and decreases the ecological validity and translatability of animal experiments [96], [97].

In recent years, researchers have started to transition to the use of awake animals in fMRI research [54], [85], [89], [98], [99]. However, awake animal MRI studies are accompanied by a variety of factors that complicate experimental procedures, including animal movement, neuromodulatory factors, and animal stress levels. To avoid these confounding effects, we used a rigorous behavioral protocol aimed at reducing animal stress levels (**section 2.3.1**). We found that the combination of our custom head constraint and habituation protocol resulted in overall low levels of head motion after habituation.

Next, we used a whisker stimulation task to determine whether our BOLD fMRI paradigm could be used to explore brain activity in an awake mouse. We found that the main regions demonstrating BOLD activation included regions commonly involved in whisker somatosensation and whisking, such as the bilateral thalamus (TH), secondary somatosensory area (SSs), orofacial domains (SSp-n) and the whisker domains (SSP-bfd) [86].

The main cortical region involved in whisker stimulation are the somatosensory barrel fields (SSp-bfd). To evaluate the quality of the BOLD fMRI signal for each mouse, we evaluated the stimulus evoked potentials in the SSp-bfd. Our results showed a strong response in the  $\Delta$ BOLD signal on both the individual and the group level. In addition, the trial-averaged response demonstrated a well defined hemodynamic response of ~4% signal change during contralateral whisker stimulation, which is in line with previous studies using a similar experimental paradigm [54]. These results form the foundation for the experiments described in this work, and confirm that our awake animal paradigm could be used to accurately determine the spatial location and temporal evolution of the hemodynamic response.

Finally, our results show that the BOLD fMRI signal contains high amounts of variability between animals and trials. This variability could result from the attention level and mental state of the animal [89], meaning that the variability is of interest when evaluating the relationship between neural activity patterns and the hemodynamic response. Importantly, the variability between trials cannot be evaluated using traditional experimental approaches that use sequential measurements of the neural and vascular activity. For this reason, we developed a new paradigm that allows researchers to simultaneously measure both the local neural activity through microscopic calcium imaging and whole brain BOLD fMRI.

**Simultaneous calcium recordings during awake animal fMRI.** During BOLD fMRI acquisition, we simultaneously measured the calcium activity of neurons in layer 2/3 of the SSp-bfd. We recorded a total of 203 neurons within 4 animals ( $51 \pm 13$  per animal; mean  $\pm$  s.d.) using the novel MRI compatible microscope. We found that ~20% of cells responded positively to the contralateral whisker stimulation, while ~7% of cells showed a negative relationship.

In addition, we evaluated the evoked calcium response in the SSp-bfd in response to contralateral whisker stimulation. For both the  $\Delta F/F$  neural population and neuropil signal we observed a strong stimulus evoked potential on the subject level, as well as for the trial averaged time series. The neural calcium activity demonstrated high levels of noise around the average, which can be explained by the high sampling rate of calcium imaging, as well as certain parameters of the MRI compatible camera (low quantum efficacy, high pixel-level quantum noise).

In addition, the relatively high noise in the neuropil as compared to the cellular signal can result from the sparse expression of calcium indicators in layer 2/3 of our transgenic animal model [62]. This strategy is commonly used to increase the signal-to-noise ratio of cells within a recording by decreasing the background contamination.

**Local interactions between SSp-bdf neurons and BOLD fMRI.** To gain a deeper understanding of the interactions between local neural activity and the BOLD fMRI

---

response, we used the combined microscope fMRI recordings to investigate the factors of the local neural activity that contribute to the formation of the BOLD fMRI response in the SSp-bfd.

First, we used a decoding approach based on support vector machines (SVMs) to quantify the predictive information of the local neural population with respect to the BOLD fMRI signal (**section 4.2.2**). We found that the neural activity for all individual mice predicted the local  $\Delta$ BOLD fMRI signal accurately, which confirmed that local neural population activity contains information relevant to the BOLD fMRI signal.

Next, we leveraged the spatial component of the microscope recordings to evaluate whether neuron-vascular proximity contributes to the relationship between the neural population and the hemodynamic response. Including a spatial component allowed us to add context to the local activity by providing information about neuron location, vasculature composition, and the spatial arrangement between neurons and the vasculature. To assess the influence of the neuron-vascular proximity on  $\Delta$ BOLD fMRI prediction, we quantized the proximity values within each animal based on the ranking of the  $\beta$ -weights determined by three ranking criteria (lowest absolute decoder weight elimination, lowest decoder weight elimination, and highest absolute decoder weight elimination). Our results showed that on average, neurons with a lower proximity (i.e. are located closer to the vascular structure) had more negative  $\beta$ -weights ascribed. This implies that neurons located closer to a vascular structure have a negative relationship with the  $\Delta$ BOLD fMRI signal, as identified through the neural-BOLD decoding approach. However, further experiments are needed to determine the exact nature of the relationship. Together these results demonstrate that the spatial context in microscope fMRI experiments can provide a more detailed explanation of the relationship between neural activity and the hemodynamic response, leading to a better understanding of the neural activity underlying BOLD fMRI.

**The influence of global hemodynamics on the local neural response.** Regions across the brain are widely interconnected, and can influence the neural activity of remote populations through direct and indirect afferent connections. To investigate the complex interactions between the different anatomical regions and the local neural activity, we can leverage the high spatial coverage and resolution of BOLD fMRI measurements.

We used a decoding approach based on support vector machines (SVMs) to quantify the predictive information of the BOLD fMRI signal in anatomically defined regions with respect to the local neural population activity in the SSp-bfd (described in **section 4.2.3**). Next, we represented the results through a NRMSE magnitude map to visualize which areas contained the most information about the local neural population activity in the SSp-bfd. We observed a strong laterality effect for anatomical regions involved in whisker stimulation, which is consistent with previous findings of the mouse whisker

system [90], [91]. In addition, anatomically connected areas such as the primary motor region (MOp) [90] and the striatum (STR) [87], [92] also contained a high amount of predictive information.

Together these results demonstrate that different cortical and subcortical regions contain information that can be used to predict neural activity in the SSP-bfd. In addition, the use of NRMSE magnitude maps can be used to reconstruct patterns of laterality and connectivity from microscope fMRI data. Interestingly, future studies could use the microscope fMRI paradigm to explore how different regions affect the activity in local neural populations through for example afferent neuromodulatory connections. In addition, the microscope fMRI approach could be used to map the flow of information throughout the brain, and determine how it affects the neural population activity in regions involved in cognition or disease [100], [101].

**Cell type specificity.** Through the use of genetic targeting methods, calcium imaging allows scientists to label and track specific types of neurons (**section 1.5.2**). In this thesis we explored the possibility of measuring animals expressing a GECI in both excitatory and inhibitory neurons. We found that the yield in animals expressing calcium indicators in inhibitory somatostatin neurons, was noticeably lower than recordings in animals expressing GCaMP in layer 2/3 excitatory neurons. Previous results show that this is a common finding due to the lower number of somatostatin positive cells in the cortex [93], [94]. In addition, our anatomical results showed that the distribution of the transfected cells were largely concentrated in layer four and five [94], which could mean that the limited depth of focus of the MRI compatible microscope might not reach a large proportion of the targeted cells (Chapter 3).

Another issue we faced during experiments with somatostatin-IRES-Cre mice concerned the behavioral protocol described in **section 2.3.1**. Even after rigorous habituation, animals exhibited high levels of movement during experiments. We found that although the average motion was below the recommended threshold for BOLD fMRI recordings, most of the movement occurred during trials. This means that the BOLD fMRI data did not meet our behavioral criteria for inclusion. In the future, more extensive habituation protocols are needed for experiments involving somatostatin-IRES-Cre animals.

## 5.2 The promise of combined microscopic calcium imaging and BOLD fMRI

Neuroimaging techniques are continually improving, and the complementary strengths of methods are being leveraged to mitigate the weaknesses of others. Indeed, combined experimental strategies play an important role in neuroscience research, and can lead to better insights about brain functioning across temporal and spatial scales. Microscopy allows us to investigate the activity of genetically defined neurons on the

---

single cell level in a small population of neurons. In contrast, BOLD fMRI measures the slow, mean-proxy of local neural activity [102] across the whole brain, and can be used in healthy humans without the need for invasive surgery. The combined strengths of both neuroimaging methods can lead to several advantages for studies into the fundamental aspects of brain functioning as well as translational research. To date, combined calcium imaging and BOLD fMRI studies have focused on using fiber based readout methods to extract neural activity. To speculate how a combined microscope fMRI approach could contribute to our understanding of the brain, we can look at how researchers are currently combining fiber-based optical methods with BOLD fMRI. In this section we will evaluate different areas of research that use combined fiber-optics and BOLD fMRI, and evaluate how microscope fMRI could add to these fields. In our discussion we will focus on genetic targeting, source specificity, spatial information, and simultaneous recordings across scales.

**Models of the hemodynamic response.** One objective of combined calcium imaging and BOLD fMRI research is to investigate the relationship between local neural activity and the BOLD response. Currently, most fMRI research uses a hemodynamic response function (HRF) to translate the acquired hemodynamic activity into an estimation of the underlying neural response. However, evidence has suggested that the HRF can vary across brain regions, species and even subjects [103]–[105]. Combined calcium imaging and BOLD fMRI can be used to estimate better mathematical models of the hemodynamic response, as well as to validate the empirical HRFs for various brain regions and species. For example, [104] calculated custom HRFs based on simultaneous fiber-based calcium imaging and resting state fMRI. The result was a narrower HRF with faster dynamics as compared to the canonical HRF normally used to estimate neural activity. Interestingly, when the model was later confirmed using a GLM analysis approach to fMRI data, the empirical HRFs showed better detection of the underlying neural activity.

Studies into the relationship between neural activity and the BOLD fMRI response provide valuable information about the interpretation and mathematical formulation of the HRF. However, the neural calcium activity in most studies is measured by means of fiber photometry, which integrates the neural calcium dynamics of both the neurons and processes. This means that the information can not distinguish between cellular calcium activity and other circuit dynamics. The integration of microscopy and fMRI overcomes this constraint by introducing a spatial dimension to the captured neural activity, allowing for the separation of calcium activity from individual neurons. In addition, including a spatial component can also add context to the local activity by providing information about the neuron location, vasculature composition, and the spatial arrangement between neurons and the vasculature. These advantages of microscope fMRI could contribute to a more accurate interpretation of the neural activity underlying the hemodynamic response, as well as lead to a better formulation of the HRF for BOLD fMRI research.

**Neurovascular complex.** The interpretation of the BOLD fMRI signal is often limited to the activity of excitatory neurons [27]. However, the hemodynamic response is the result of a complex interaction between a multitude of different cell types and processes. One useful framework about how neural signals regulates the nearby microvasculature is called the neurovascular unit [106]. The neurovascular unit refers to the close relationship between the neural and vascular cells, and describes the functional and structural relationship between neurons, glial cells, and blood vessels. The neurovascular unit consists of four main components. First, the neurons and synapses that generate the main need for nutrients and oxygen. Second, the astrocytes, a type of glial cell that provides structural support to neurons and regulates the concentration of ions, neurotransmitters, and other signaling molecules in the brain. Third, pericytes that wrap around the blood vessels and regulate the diameter, blood flow, and permeability. And finally, the endothelial cells, which line the interior surface of blood vessels and form a barrier between the bloodstream and the brain.

Several studies have investigated the relationship between different cell types of the neurovascular unit and the hemodynamic response by combining calcium imaging and BOLD fMRI. For example, [55] demonstrated that the BOLD fMRI signal corresponds to slow oscillating calcium waves associated with glial cells, and that glial activity was more pronounced during sustained BOLD fMRI activation. In addition, [58] showed that distinct evoked and intrinsic astrocytic calcium signals were coupled to both positive and negative BOLD fMRI responses. However, several recent publications have argued that the conceptual framework of the neurovascular unit does not account for the role of larger cerebral arteries and systemic vasoactive signals [107]. In addition, the molecular heterogeneity of cerebrovascular cells disagrees with the existence of a canonical vascular unit. Instead, researchers have argued for a neurovascular complex consisting of diverse functional modules that demonstrate coordinated behavior between the vasculature and the neural signals [107].

Further investigation into the relationship between different aspects of the neurovascular complex and the neural activity is necessary before we can fully understand how neural activity underlies the BOLD fMRI signal. Both microscopy and BOLD fMRI play an important role in the investigation of the neurovascular complex, but occur mostly in isolation or concurrently [54], [108], [109]. Although these studies provide valuable information about the coupling between the vasculature and neurons, they are limited by factors such as trial-to-trial variability, mental state of the animal, and differences in the experimental environments between sessions. Combined microscope fMRI could mitigate these shortcomings by providing a simultaneous readout of calcium activity and BOLD fMRI within the same animal and session. These simultaneous recordings could in turn be used to construct a more comprehensive formulation of the cellular functions underlying the neurovascular complex.

---

**Inhibitory neural activity and the hemodynamic response.** In the recent past, there has been significant interest in exploring the relationship between inhibitory neural activity and the hemodynamic response. One advantage of fluorescence calcium imaging is the availability of strategies to genetically tag specific neural subpopulations. This means that the activity of inhibitory neurons can be reliably isolated and measured through calcium imaging in microscope fMRI.

To investigate the contribution of inhibitory activity, [110] modulated the excitatory and inhibitory neural activity in the mouse somatosensory cortex using simultaneous optogenetic BOLD fMRI. As expected, activation of excitatory neurons induced a positive BOLD fMRI response. However, when inhibitory GABAergic neurons were stimulated, the BOLD fMRI signal showed an initial positive inflection, followed by a prolonged negative component. This biphasic response suggests that inhibitory GABAergic neurons indeed contribute to the BOLD fMRI response. However, upon further investigation into the precise mechanism behind this observation, researchers found contradictory results. For example, the optogenetic activation of inhibitory somatostatin and parvalbumin expressing neurons has been found to elicit a negative hemodynamic response in some cases [37], while the effect on the BOLD signal has been ambiguous, with studies reporting a positive [36], [37], [39], inverted [34] or delayed positive [36], [38] hemodynamic response. The reason for this ambiguity is not well understood, and several explanations have been proposed [36], [37], [110], [111] including the specificity of the vasoactive peptides being released [33], [35]–[37], [112]–[114], non-linear inhibitory-excitatory network effects [115], and region specific effects of neural processing on the vascular [105].

Combined, these studies show both the importance of inhibitory dynamics in neurovascular coupling, and the need for further investigation. Most studies of inhibitory activity during BOLD fMRI have focussed on driving inhibitory neural populations using optogenetics [39], [110], while very few measure inhibitory calcium activity directly. The microscope fMRI paradigm could provide complementary information to optogenetic fMRI studies by allowing the measurement of genetically targeted inhibitory neurons at cellular resolution with concurrent BOLD fMRI during natural behavior.

**Neuromodulatory effects on neurovascular coupling.** Large-scale, coherent fluctuations of the BOLD fMRI signal have long been shown to occur spontaneously in humans [116]. Even though the source of these fluctuations is not completely understood, experimental evidence points to partial involvement of neuromodulatory neural activity [58], [59], [117]–[122].

One interpretation of the origin of the spontaneous, synchronous fluctuations is through shared inputs from afferent (sub-)cortical regions [123]. The cortex receives inputs from several regions such as dopaminergic projections from the ventral tegmental area [124] and cholinergic projections from the basal forebrain [125]. These regions are known to

modify the activity of neurons across the brain through the release of neuromodulators that can either enhance or inhibit local neural signaling. Recently, researchers have argued that in addition to influencing local processing in neural circuits, neuromodulation can also induce state-dependent effects on local neurovascular coupling [126]. For example, [127] investigated the effect of neuromodulation on the neural and BOLD fMRI response by exposing the macaque brain to the neuromodulator dopamine. Their results showed that the systemic injection of dopamine increased the neural activity, as well as the CBF in the visual cortex. However, they found no significant effect when the dopamine was administered locally in the visual cortex through intracortical injection. This led the researchers to conclude that dopamine has a modulatory effect on the local activity in the macaque visual cortex that is driven by long-range afferent instead of local connections.

These results demonstrate the importance of neuromodulatory effects on brain processing and the corresponding hemodynamic response. Using calcium imaging, we can directly measure the outcome of neuromodulation effects on the local circuit activity. Conversely, whole brain BOLD fMRI allows us to monitor the activity of neuromodulatory systems distributed throughout the brain. Future research could use combined microscope fMRI to integrate the strengths of both modalities and provide a more comprehensive description of how the activity of global distributed neuromodulatory systems influence the neural processing in local circuits.

### **5.3 Limitations of combined microscopic calcium imaging and BOLD fMRI**

In this thesis we introduced a novel way of investigating neural and hemodynamic responses by combining microscopy and BOLD fMRI. The usefulness of this approach relies on how well both methods function individually, as well as in combination. In this section we will present the inherent limitations of both methods as stand alone neuroimaging techniques as well as the limitations of combining both methods.

**Calcium imaging as a marker for neural activity.** Calcium imaging measures changes in intracellular calcium levels through genetically encoded calcium indicators (GECIs; **section 1.5.2**). The changes in intracellular calcium levels as a response to neural activation is an indirect reflection of neuronal activity (**section 1.5.1**). While the influx of calcium occurs simultaneously with spiking activity, the time course is generally different from an electrical action potential. The rise time of calcium signals is typically tens to hundreds of milliseconds, whereas action potentials occur on the order of microseconds [46]. In addition, the slow exponential decay due to the calcium buffering expands the duration of the calcium response as compared to the action potential. The amplitude of calcium signals is also affected by the buffering capacity of the cell, which can vary between different neurons and under different conditions. In addition, it has also been shown that calcium indicators can act as calcium buffers, which reduces the



magnitude of the relative change in calcium during repeated spiking, resulting in proportional slowing of the rate of fluorescent change [128].

These shortcomings have to be taken into consideration when designing and interpreting experiments based on calcium indicators. In contrast, some researchers have suggested the use of low affinity dyes that possess weaker buffer qualities [128], [129], or the direct optical measurement of the membrane potential through voltage-sensitive dyes or genetically encoded voltage indicators [130]–[132].

**The limited temporal resolution of BOLD fMRI.** BOLD fMRI has a relatively low temporal resolution as compared to other non-invasive neuroimaging techniques such as electroencephalography (EEG) and magnetoencephalography (MEG). There are several reasons why the temporal resolution of BOLD fMRI is relatively low. First, the hemodynamic response is slow as compared to neural activity, resulting in a delay between neural activity and the BOLD response. Second, the scanning rate of acquiring an image of the whole brain is on the order of seconds, which limits the ability to measure rapid changes in neural activity. Third, the inherent low signal-to-noise ratio of functional MRI contrasts necessitates long acquisition times, limiting the design of faster sequences. However, efforts have been made to improve on the temporal resolution of BOLD fMRI through technical developments. These include the development of multiband imaging, decreased image acquisition times, compressed sensing, and the use of ultra-high field MRI machines [16], [133]–[135].

Another recent technological development increased the temporal resolution, as well as the source specificity, through the use of a different MRI contrast. [136] developed a two-dimensional gradient-echo imaging sequence that allowed millisecond temporal resolution without sacrificing spatial resolution. This increase in temporal resolution was achieved by swapping the repetition and phase encoding loops in the pulse sequence. To confirm the biological source of the contrast, the authors evoked brain activation using whisker stimulation. They observed an increase of 0.2% in the MRI signal, which occurred simultaneously to an increase in electrical potential measured by an electrode implant. In addition, the authors noted that the stimulus evoked change occurred with only a short delay, meaning the signal is likely related to some aspect of electrical neural firing. Advances in the design of novel MRI contrasts holds promise for future fMRI research, however more research and source validation is necessary.

**Geometrical limitations of combined microscope fMRI in mice.** During the experiments described in this thesis, the region of interest was the same for both the microscopy and fMRI. This introduced compatibility issues between the methods due to the required proximity of both the microscope objective and the RF receive coil to the region of interest. We resolved this issue by using a circular surface coil (RF SUC 300 1H LNA AV3 BRUKER BioSpin MRI GmbH) which allowed us to pass the objective through the center of the coil. However, surface coils suffer from limited coverage,

artifacts such as shading, and a decrease in signal-to-noise ratio proportional to the distance to the coil.

Other researchers have suggested the use of alternative RF coils, such as cryogenically cooled or custom geometry coils, to optimize the signal-to-noise ratio in BOLD fMRI animal experiments. The advantages of custom RF coils as compared to surface RF coils includes reduced susceptibility artifacts, improved RF transmission homogeneity, and an increased flexibility which can be used to geometrically conform the coil to the region of interest. However, in combined microscope fMRI experiments, the choice of RF coil geometry is constrained by the presence of the microscope objective, meaning that our experiments were limited to the use of a circular surface coil.

**Tissue heating during combined microscope fMRI experiments.** The high intensity of light used during optical experiments can lead to increases in temperature of the imaged tissue, which can result in changes of the T1 and T2\* relaxation times [66]. The change in relaxation times can be explained by several mechanisms. First, the thermal motion of molecules increases during tissue heating, leading to an increased chemical exchange between the tissue and its surroundings, and a decrease in T1 relaxation time. Second, the increase in thermal motion leads to an increase in magnetic field inhomogeneities due to the random motion of magnetic field gradients created by the surrounding tissue. The increased magnetic field inhomogeneities decrease the T2\* relaxation time due to the faster decay in transverse magnetization.

[137] found that the influence of tissue heating depends on the net energy deposited into the tissue as determined by the duration, intensity, and frequency of the light stimulation. They propose the use of control experiments where the same net energy is used without calcium indicators or neural manipulation methods such as optogenetics. Using this control will demonstrate the effect of the energy deposit on the BOLD fMRI signal, and can aid in choosing a parameter set that reduces confounding effects. In the current thesis we minimized the net energy deposit by reducing the intensity of the excitation light, and deactivating the laser in between trials.

**Awake mouse fMRI.** In the experiments described within this thesis, we performed all experiments in awake animals. This approach can lead to several experimental difficulties. One main problem with awake animal research is potential stress and motion artifacts in the BOLD fMRI signal [95]. However, as shown by previous studies, and our results described in **section 2.3.1**, a rigorous habituation and handling protocol can be used to reduce stress and motion levels in mice [98], [99], [138], [139]. A second problem of awake animal fMRI is the loud acoustic noise produced by fMRI scan sequences. Loud noises during BOLD fMRI acquisition complicate the habituation process due to the adverse reaction of the mouse to the sounds. In addition, constant repetitive sounds throughout the acquisition complicate the use of MRI imaging in

awake experiments investigating audition. Likewise, experiments that are not interested in audition have to take the repetitive sound pattern into consideration when interpreting results. However, this problem is effectively being addressed in both human and animal MRI imaging by attempts to decrease the sound pressure levels during acquisition. Solutions include wave phase reduction, altered pulse sequences, and hardware adjustments [140]–[143].

## 5.4 Future prospects of microscopic calcium imaging in BOLD fMRI research

In the previous sections we outlined several promises and limitations of combined microscope fMRI. However, the results in this thesis constitute a proof of concept, and further work can improve on several aspects of the microscope fMRI approach. In this section we will discuss future directions for combined microscope fMRI, and propose possible future developments.

**Combined microscopy and neural stimulation.** Contemporary stimulation methods use metal or MRI compatible glass electrodes to modulate local neural activity. For example, [144] demonstrated the existence of in vivo functional connectivity maps in the primate brain by measuring BOLD fMRI while applying electrical microstimulation through implanted electrodes. Despite its benefits, the use of electrical stimulation in neuroscience research has several limitations. Specifically, it lacks the precision to selectively target specific cell types and often leads to the stimulation of a large population of neurons with a wide spatial distribution around the electrode.

In contrast, optogenetic techniques provide real-time, optical manipulation of neural tissue with higher genetic, temporal and spatial precision [145]. The procedure behind the use of optogenetics is similar to that of calcium imaging (for a detailed description, see **section 1.5.1** and **1.5.2**). However, the difference lies in the expression of light-activated ion channels such as channelrhodopsin (ChR), halorhodopsin (Halo), or light-gated ionotropic glutamate receptors [146]. These ion channels can be activated or inhibited by light on a millisecond time scale, and the expression benefits from the same genetic tools used in calcium imaging.

Recently, researchers have combined optogenetics with fMRI to show the feasibility of examining the functional connectivity of genetically defined neurons at the whole brain level. For example, [39] performed one of the first combined opto-fMRI experiments and showed the involvement of excitatory neurons in both the local and global brain activity as measured by BOLD fMRI. They found that optogenetic stimulation in the primary motor cortex elicited not only a local response, but also in downstream regions such as the thalamus.

In the future, optogenetic manipulations could be implemented in combined microscope fMRI experiments through the addition of a secondary light source into the excitation path. The design of the microscope proposed in this thesis can be equipped with a different filter set that integrates an additional light source into the imaging path in the same manner as currently used for the excitation light. However, potential studies have to take into account the challenges of combined optogenetics and BOLD fMRI. First, the current design modulates the activity of the targeted neural population as a whole due to the homogeneous illumination. Previous studies have demonstrated methods to target individual neurons [147], however, these methods are currently incompatible with the microscope design presented in this thesis. Second, the expression of opsins can result in an alteration of the natural activation patterns of the targeted neurons due to the induced ion channels [148]. Finally, optogenetic stimulation requires high levels of laser power. As explained in **section 5.3**, this can lead to significant BOLD fMRI artifacts due to tissue heating.

**Large field of view microscopy.** Microscopes with a large field of view allow researchers to observe a vast number of cells, spanning multiple functionally and structurally defined regions. This enables researchers to make more accurate inferences related to neural activity patterns across the brain, and how they relate to the hemodynamic response.

Recent studies have demonstrated the importance of acquiring a large subset of neurons to achieve an appropriate representation of the local population activity. [149] used two-photon calcium imaging to measure the activity of  $\pm 60,000$  neurons over multiple sessions during a passive viewing paradigm in mice. They found that even though a subset of neurons could be described by classical models of cortical visual processing, an overwhelming segment of recorded neurons could not. These studies emphasize the importance of large-scale population recordings to achieve a holistic view of neural activity, and in extension the corresponding hemodynamic response. Advantages of large-scale recordings include the unbiased global exploration of cell responses, increased probability of finding and explaining outlier neural activity patterns, and a shift in focus towards population analysis of the neural activity underlying the hemodynamic response [3].

In addition, large field-of-view microscopy could also offer insights into multi-region interactions. For example, [61] used a multi-fiber bundle to record simultaneous calcium activity and BOLD fMRI across the whole cortex. Using this approach they showed that calcium activity is related to the BOLD fMRI signal across the cortex during both stimulus driven and spontaneous activity. Future approaches using combined microscope fMRI could add to these findings by increasing the spatial coverage to include single cell imaging of the whole cortex. Rich datasets like these will drive our understanding of multi-region neural activity and hemodynamics, and could lead to brain-wide models of neurovascular coupling.

## 5.5 Conclusions

In this thesis we presented a new paradigm that allows for the simultaneous measurement of local microscopic calcium activity and BOLD fMRI. By combining both experimental imaging techniques, we were able to observe the calcium activity of layer 2/3 neurons in the somatosensory barrel fields (SSp-bfd) during whisker stimulation, while concurrently acquiring the whole brain BOLD fMRI signal.

Next, we used the data from the microscope fMRI approach to explore the activity of the brain across spatial scales. First, we examined the interaction between individual cells in the SSp-bfd and the local BOLD fMRI response. We used the spatial component of the microscope recordings to determine the relative distance between the neurons and the vascular structure, and examined whether the proximity between neurons and the vasculature was related to the hemodynamic response. Using a linear regression based decoding approach, we found that neurons located closer to a vascular structure have a negative relationship with the BOLD fMRI signal.

Second, we leveraged the spatial coverage of whole brain BOLD fMRI to relate the activity from anatomically defined regions involved in whisking behavior to the local neural activity in the SSp-bfd. We used a linear regression based decoding approach to determine the degree of information contained within different brain regions about the local neural population. Our results demonstrate that different areas hold different levels of information relevant to the local neural activity in the SSp-bfd. In addition, we showed that properties of the whisker system, such as laterality and connectivity, could be reconstructed through the combined microscope fMRI approach.

Collectively, these results provide evidence for the application of combined microscope fMRI in probing cross-scale brain activity. In addition, the experiments presented in this thesis highlight the benefit of incorporating complementary neuroimaging methods to improve our understanding of brain functions across scales.

## Bibliography

- [1] E. D. Adrian and B. H. C. Matthews, "The interpretation of potential waves in the cortex," *J. Physiol.*, vol. 81, no. 4, p. 440, Jul. 1934.
- [2] A. C. Paulk *et al.*, "Large-scale neural recordings with single neuron resolution using Neuropixels probes in human cortex," *Nat. Neurosci.*, vol. 25, no. 2, Feb. 2022, doi: 10.1038/s41593-021-00997-0.
- [3] A. E. Urai, B. Doiron, A. M. Leifer, and A. K. Churchland, "Large-scale neural recordings call for new insights to link brain and behavior," *Nat. Neurosci.*, vol. 25, no. 1, Jan. 2022, doi: 10.1038/s41593-021-00980-9.
- [4] P. A. Bandettini, E. C. Wong, R. S. Hinks, R. S. Tikofsky, and J. S. Hyde, "Time course EPI of human brain function during task activation," *Magn. Reson. Med.*, vol. 25, no. 2, pp. 390–397, Jun. 1992.
- [5] S. Ogawa *et al.*, "Intrinsic signal changes accompanying sensory stimulation: functional brain mapping with magnetic resonance imaging," *Proc. Natl. Acad. Sci. U. S. A.*, vol. 89, no. 13, pp. 5951–5955, Jul. 1992.
- [6] J. M. Soares *et al.*, "A Hitchhiker's Guide to Functional Magnetic Resonance Imaging," *Front. Neurosci.*, vol. 10, Nov. 2016, doi: 10.3389/fnins.2016.00515.
- [7] T. L. Stackhouse and A. Mishra, "Neurovascular Coupling in Development and Disease: Focus on Astrocytes," *Front. Cell Dev. Biol.*, vol. 9, Jul. 2021, doi: 10.3389/fcell.2021.702832.
- [8] N. K. Logothetis, J. Pauls, M. Augath, T. Trinath, and A. Oeltermann, "Neurophysiological investigation of the basis of the fMRI signal," *Nature*, vol. 412, no. 6843, pp. 150–157, Jul. 2001.
- [9] N. K. Logothetis, "What we can do and what we cannot do with fMRI," *Nature*, vol. 453, no. 7197, pp. 869–878, Jun. 2008.
- [10] R. Mukamel, H. Gelbard, A. Arieli, U. Hasson, I. Fried, and R. Malach, "Coupling between neuronal firing, field potentials, and FMRI in human auditory cortex," *Science*, vol. 309, no. 5736, Aug. 2005, doi: 10.1126/science.1110913.
- [11] D. Chaimow, E. Yacoub, K. Ugurbil, and A. Shmuel, "Modeling and analysis of mechanisms underlying fMRI-based decoding of information conveyed in cortical columns," *Neuroimage*, vol. 56, no. 2, May 2011, doi: 10.1016/j.neuroimage.2010.09.037.
- [12] R. Ansorge and M. Graves, *The Physics and Mathematics of MRI*. Morgan & Claypool Publishers, 2016.
- [13] A.-M. Oros-Peusquens, R. Loução, Z. Abbas, V. Gras, M. Zimmermann, and N. J. Shah, "A Single-Scan, Rapid Whole-Brain Protocol for Quantitative Water Content Mapping With Neurobiological Implications," *Front. Neurol.*, vol. 10, Dec. 2019, doi: 10.3389/fneur.2019.01333.
- [14] R. J. van Geuns *et al.*, "Basic principles of magnetic resonance imaging," *Prog. Cardiovasc. Dis.*, vol. 42, no. 2, Sep. 1999, doi: 10.1016/s0033-0620(99)70014-9.
- [15] M. L. Winkler *et al.*, "Characteristics of partial flip angle and gradient reversal MR imaging," *Radiology*, vol. 166, no. 1 Pt 1, pp. 17–26, Jan. 1988.
- [16] Q. Shen, H. Ren, and T. Q. Duong, "CBF, BOLD, CBV, and CMRO(2) fMRI signal temporal dynamics at 500-msec resolution," *J. Magn. Reson. Imaging*, vol. 27, no. 3, Mar. 2008, doi: 10.1002/jmri.21203.
- [17] A. C. Silva, S. P. Lee, G. Yang, C. Iadecola, and S. G. Kim, "Simultaneous blood oxygenation level-dependent and cerebral blood flow functional magnetic resonance imaging during forepaw stimulation in the rat," *J. Cereb. Blood Flow Metab.*, vol. 19, no. 8, Aug. 1999, doi: 10.1097/00004647-199908000-00006.

- 
- [18] I. Kida, D. L. Rothman, and F. Hyder, "Dynamics of changes in blood flow, volume, and oxygenation: implications for dynamic functional magnetic resonance imaging calibration," *J. Cereb. Blood Flow Metab.*, vol. 27, no. 4, Apr. 2007, doi: 10.1038/sj.jcbfm.9600409.
- [19] A. R. Nippert, K. R. Biesecker, and E. A. Newman, "Mechanisms Mediating Functional Hyperemia in the Brain," *Neuroscientist*, vol. 24, no. 1, p. 73, Feb. 2018.
- [20] C. Bédard, H. Kröger, and A. Destexhe, "Modeling Extracellular Field Potentials and the Frequency-Filtering Properties of Extracellular Space," *Biophys. J.*, vol. 86, no. 3, p. 1829, Mar. 2004.
- [21] G. Northoff *et al.*, "GABA concentrations in the human anterior cingulate cortex predict negative BOLD responses in fMRI," *Nat. Neurosci.*, vol. 10, no. 12, Dec. 2007, doi: 10.1038/nn2001.
- [22] L. Boorman *et al.*, "Negative blood oxygen level dependence in the rat: a model for investigating the role of suppression in neurovascular coupling," *J. Neurosci.*, vol. 30, no. 12, Mar. 2010, doi: 10.1523/JNEUROSCI.6063-09.2010.
- [23] L. Boorman *et al.*, "Long-Latency Reductions in Gamma Power Predict Hemodynamic Changes That Underlie the Negative BOLD Signal," *J. Neurosci.*, vol. 35, no. 11, pp. 4641–4656, Mar. 2015.
- [24] A. Devor *et al.*, "Suppressed Neuronal Activity and Concurrent Arteriolar Vasoconstriction May Explain Negative Blood Oxygenation Level-Dependent Signal," *J. Neurosci.*, vol. 27, no. 16, p. 4452, Apr. 2007.
- [25] A. Kastrup *et al.*, "Behavioral correlates of negative BOLD signal changes in the primary somatosensory cortex," *Neuroimage*, vol. 41, no. 4, Jul. 2008, doi: 10.1016/j.neuroimage.2008.03.049.
- [26] N. Harel, S. P. Lee, T. Nagaoka, D. S. Kim, and S. G. Kim, "Origin of negative blood oxygenation level-dependent fMRI signals," *J. Cereb. Blood Flow Metab.*, vol. 22, no. 8, Aug. 2002, doi: 10.1097/00004647-200208000-00002.
- [27] C. Howarth, A. Mishra, and C. N. Hall, "More than just summed neuronal activity: how multiple cell types shape the BOLD response," *Philos. Trans. R. Soc. Lond. B Biol. Sci.*, vol. 376, no. 1815, p. 20190630, Jan. 2021.
- [28] A. Maier, M. Wilke, C. Aura, C. Zhu, F. Q. Ye, and D. A. Leopold, "Divergence of fMRI and neural signals in V1 during perceptual suppression in the awake monkey," *Nat. Neurosci.*, vol. 11, no. 10, p. 1193, Oct. 2008.
- [29] A. Ekstrom, "How and when the fMRI BOLD signal relates to underlying neural activity: The danger in dissociation," *Brain Res. Rev.*, vol. 62, no. 2, p. 233, Mar. 2010.
- [30] A. M. Mishra *et al.*, "Where fMRI and Electrophysiology Agree to Disagree: Corticothalamic and Striatal Activity Patterns in the WAG/Rij Rat," *J. Neurosci.*, vol. 31, no. 42, p. 15053, Oct. 2011.
- [31] C. R. Figley and P. W. Stroman, "The role(s) of astrocytes and astrocyte activity in neurometabolism, neurovascular coupling, and the production of functional neuroimaging signals," *Eur. J. Neurosci.*, vol. 33, no. 4, Feb. 2011, doi: 10.1111/j.1460-9568.2010.07584.x.
- [32] L. Tricoire and V. Tania, "Neuronal nitric oxide synthase expressing neurons: a journey from birth to neuronal circuits," *Front. Neural Circuits*, vol. 6, Dec. 2012, doi: 10.3389/fncir.2012.00082.
- [33] B. Cauli *et al.*, "Cortical GABA interneurons in neurovascular coupling: relays for subcortical vasoactive pathways," *J. Neurosci.*, vol. 24, no. 41, Oct. 2004, doi: 10.1523/JNEUROSCI.3065-04.2004.
- [34] J. Lee *et al.*, "Opposed hemodynamic responses following increased excitation and parvalbumin-based inhibition," *J. Cereb. Blood Flow Metab.*, vol. 41, no. 4, Apr. 2021, doi: 10.1177/0271678X20930831.
- [35] H. Uhlirova *et al.*, "Cell type specificity of neurovascular coupling in cerebral cortex," *Elife*, vol. 5, May 2016, doi: 10.7554/eLife.14315.

- [36] M. B. Krawchuk, C. F. Ruff, X. Yang, S. E. Ross, and A. L. Vazquez, "Optogenetic assessment of VIP, PV, SOM and NOS inhibitory neuron activity and cerebral blood flow regulation in mouse somato-sensory cortex," *J. Cereb. Blood Flow Metab.*, vol. 40, no. 7, Jul. 2020, doi: 10.1177/0271678X19870105.
- [37] L. Lee *et al.*, "Key Aspects of Neurovascular Control Mediated by Specific Populations of Inhibitory Cortical Interneurons," *Cereb. Cortex*, vol. 30, no. 4, Apr. 2020, doi: 10.1093/cercor/bhz251.
- [38] M. K. Dahlqvist, K. J. Thomsen, and M. J. Lauritzen, "Modification of oxygen consumption and blood flow in mouse somatosensory cortex by cell-type-specific neuronal activity," *J. Cereb. Blood Flow Metab.*, vol. 40, no. 10, Oct. 2020, doi: 10.1177/0271678X19882787.
- [39] J. H. Lee *et al.*, "Global and local fMRI signals driven by neurons defined optogenetically by type and wiring," *Nature*, vol. 465, no. 7299, Jun. 2010, doi: 10.1038/nature09108.
- [40] E. Anenberg, A. W. Chan, Y. Xie, J. M. LeDue, and T. H. Murphy, "Optogenetic stimulation of GABA neurons can decrease local neuronal activity while increasing cortical blood flow," *J. Cereb. Blood Flow Metab.*, vol. 35, no. 10, Oct. 2015, doi: 10.1038/jcbfm.2015.140.
- [41] E. R. Kandel, J. D. Koester, S. H. Mack, and S. A. Siegelbaum, *Principles of Neural Science, Sixth Edition*. McGraw Hill Professional, 2021.
- [42] M. J. Berridge, P. Lipp, and M. D. Bootman, "The versatility and universality of calcium signalling," *Nat. Rev. Mol. Cell Biol.*, vol. 1, no. 1, pp. 11–21, Oct. 2000.
- [43] F. Helmchen, K. Imoto, and B. Sakmann, "Ca<sup>2+</sup> buffering and action potential-evoked Ca<sup>2+</sup> signaling in dendrites of pyramidal neurons," *Biophys. J.*, vol. 70, no. 2, Feb. 1996, doi: 10.1016/S0006-3495(96)79653-4.
- [44] M. J. Berridge, Bootman, and H. L. Roderick, "Calcium signalling: dynamics, homeostasis and remodelling," *Nat. Rev. Mol. Cell Biol.*, vol. 4, no. 7, Jul. 2003, doi: 10.1038/nrm1155.
- [45] J. Nakai, M. Ohkura, and K. Imoto, "A high signal-to-noise Ca(2+) probe composed of a single green fluorescent protein," *Nat. Biotechnol.*, vol. 19, no. 2, Feb. 2001, doi: 10.1038/84397.
- [46] L. Huang *et al.*, "Relationship between simultaneously recorded spiking activity and fluorescence signal in GCaMP6 transgenic mice," Mar. 2021, doi: 10.7554/eLife.51675.
- [47] L. Tian *et al.*, "Imaging neural activity in worms, flies and mice with improved GCaMP calcium indicators," *Nat. Methods*, vol. 6, no. 12, pp. 875–881, Nov. 2009.
- [48] S. Navabpour, J. L. Kwapis, and T. J. Jarome, "A neuroscientist's guide to transgenic mice and other genetic tools," *Neurosci. Biobehav. Rev.*, vol. 108, Jan. 2020, doi: 10.1016/j.neubiorev.2019.12.013.
- [49] C. J. R. Sheppard, "Multiphoton microscopy: a personal historical review, with some future predictions," *J. Biomed. Opt.*, vol. 25, no. 1, Jan. 2020, doi: 10.1117/1.JBO.25.1.014511.
- [50] J. Lecoq, N. Orlova, and B. F. Grewe, "Wide. Fast. Deep: Recent Advances in Multiphoton Microscopy of In Vivo Neuronal Activity," *J. Neurosci.*, vol. 39, no. 46, pp. 9042–9052, Nov. 2019.
- [51] G. J. Goldey *et al.*, "Removable cranial windows for long-term imaging in awake mice," *Nat. Protoc.*, vol. 9, no. 11, Nov. 2014, doi: 10.1038/nprot.2014.165.
- [52] M. J. Levene, D. A. Dombeck, K. A. Kasischke, R. P. Molloy, and W. W. Webb, "In vivo multiphoton microscopy of deep brain tissue," *J. Neurophysiol.*, vol. 91, no. 4, Apr. 2004, doi: 10.1152/jn.01007.2003.
- [53] B. F. Grewe *et al.*, "Neural ensemble dynamics underlying a long-term associative memory," *Nature*, vol. 543, no. 7647, pp. 670–675, Mar. 2017.
- [54] M. Desjardins *et al.*, "Awake Mouse Imaging: From Two-Photon Microscopy to Blood Oxygen Level-Dependent Functional Magnetic Resonance Imaging," *Biological Psychiatry: Cognitive Neuroscience and Neuroimaging*, vol. 4, no. 6, pp. 533–542, Jun. 2019.
- [55] K. Schulz *et al.*, "Simultaneous BOLD fMRI and fiber-optic calcium recording in rat neocortex," *Nature Methods*, vol. 9, no. 6, pp. 597–602, 2012. doi: 10.1038/nmeth.2013.
- [56] F. Schlegel *et al.*, "Fiber-optic implant for simultaneous fluorescence-based calcium



- recordings and BOLD fMRI in mice,” *Nat. Protoc.*, vol. 13, no. 5, pp. 840–855, May 2018.
- [57] Z. Liang, Y. Ma, G. D. R. Watson, and N. Zhang, “Simultaneous GCaMP6-based fiber photometry and fMRI in rats,” *J. Neurosci. Methods*, vol. 289, pp. 31–38, Sep. 2017.
- [58] M. Wang, Y. He, T. J. Sejnowski, and X. Yu, “Brain-state dependent astrocytic Ca<sup>2+</sup> signals are coupled to both positive and negative BOLD-fMRI signals,” *Proc. Natl. Acad. Sci. U. S. A.*, vol. 115, no. 7, pp. E1647–E1656, Feb. 2018.
- [59] M. Schwalm *et al.*, “Cortex-wide BOLD fMRI activity reflects locally-recorded slow oscillation-associated calcium waves,” *Elife*, vol. 6, Sep. 2017, doi: 10.7554/eLife.27602.
- [60] C. Tong, J.-K. Dai, Y. Chen, K. Zhang, Y. Feng, and Z. Liang, “Differential coupling between subcortical calcium and BOLD signals during evoked and resting state through simultaneous calcium fiber photometry and fMRI,” *Neuroimage*, vol. 200, pp. 405–413, Oct. 2019.
- [61] E. M. R. Lake *et al.*, “Simultaneous cortex-wide fluorescence Ca<sup>2+</sup> imaging and whole-brain fMRI,” *Nat. Methods*, vol. 17, no. 12, pp. 1262–1271, Dec. 2020.
- [62] J. A. Harris *et al.*, “Anatomical characterization of Cre driver mice for neural circuit mapping and manipulation,” *Front. Neural Circuits*, vol. 8, Jul. 2014, doi: 10.3389/fncir.2014.00076.
- [63] T. W. Chen *et al.*, “Ultrasensitive fluorescent proteins for imaging neuronal activity,” *Nature*, vol. 499, no. 7458, Jul. 2013, doi: 10.1038/nature12354.
- [64] S. W. Oh *et al.*, “A mesoscale connectome of the mouse brain,” *Nature*, vol. 508, no. 7495, pp. 207–214, Apr. 2014.
- [65] J. A. Harris *et al.*, “Hierarchical organization of cortical and thalamic connectivity,” *Nature*, vol. 575, no. 7781, Nov. 2019, doi: 10.1038/s41586-019-1716-z.
- [66] I. N. Christie *et al.*, “fMRI response to blue light delivery in the naïve brain: implications for combined optogenetic fMRI studies,” *Neuroimage*, vol. 66, Feb. 2013, doi: 10.1016/j.neuroimage.2012.10.074.
- [67] A. L. Weldon *et al.*, “Stress response to the fMRI environment in healthy adults relates to degree of limbic reactivity during emotion processing,” *Neuropsychobiology*, vol. 71, no. 2, p. 85, 2015.
- [68] “Acute stress alters the ‘default’ brain processing,” *Neuroimage*, vol. 189, pp. 870–877, Apr. 2019.
- [69] “Acute stress alters neural patterns of value representation for others,” *Neuroimage*, vol. 209, p. 116497, Apr. 2020.
- [70] J. L. Hurst and R. S. West, “Taming anxiety in laboratory mice,” *Nat. Methods*, vol. 7, no. 10, Oct. 2010, doi: 10.1038/nmeth.1500.
- [71] K. Gouveia and J. L. Hurst, “Improving the practicality of using non-aversive handling methods to reduce background stress and anxiety in laboratory mice,” *Sci. Rep.*, vol. 9, no. 1, Dec. 2019, doi: 10.1038/s41598-019-56860-7.
- [72] J. D. Power, K. A. Barnes, A. Z. Snyder, B. L. Schlaggar, and S. E. Petersen, “Spurious but systematic correlations in functional connectivity MRI networks arise from subject motion,” *Neuroimage*, vol. 59, no. 3, p. 2142, Feb. 2012.
- [73] “GitHub - IBT-FMI/SAMRI: Small Animal Magnetic Resonance Imaging via Python,” *GitHub*. <https://github.com/IBT-FMI/SAMRI> (accessed Apr. 08, 2023).
- [74] H.-I. Ioanas, M. Marks, C. M. Garin, M. Dhenain, M. F. Yanik, and M. Rudin, “An Automated Open-Source Workflow for Standards-Compliant Integration of Small Animal Magnetic Resonance Imaging Data,” *Front. Neuroinform.*, vol. 14, Feb. 2020, doi: 10.3389/fninf.2020.00005.
- [75] H. I. Ioanas, M. Marks, V. Zerbi, M. F. Yanik, and M. Rudin, “An optimized registration workflow and standard geometric space for small animal brain imaging,” *Neuroimage*, vol. 241, Nov. 2021, doi: 10.1016/j.neuroimage.2021.118386.
- [76] A. Roche, “A four-dimensional registration algorithm with application to joint correction of motion and slice timing in fMRI,” *IEEE Trans. Med. Imaging*, vol. 30, no. 8, Aug. 2011, doi: 10.1109/TMI.2011.2131152.

- [77] B. B. Avants, N. J. Tustison, G. Song, P. A. Cook, A. Klein, and J. C. Gee, "A reproducible evaluation of ANTs similarity metric performance in brain image registration," *Neuroimage*, vol. 54, no. 3, Feb. 2011, doi: 10.1016/j.neuroimage.2010.09.025.
- [78] A. E. Dorr, J. P. Lerch, S. Spring, N. Kabani, and R. M. Henkelman, "High resolution three-dimensional brain atlas using an average magnetic resonance image of 40 adult C57Bl/6J mice," *Neuroimage*, vol. 42, no. 1, Aug. 2008, doi: 10.1016/j.neuroimage.2008.03.037.
- [79] R. W. Cox, "AFNI: software for analysis and visualization of functional magnetic resonance neuroimages," *Comput. Biomed. Res.*, vol. 29, no. 3, Jun. 1996, doi: 10.1006/cbmr.1996.0014.
- [80] M. Jenkinson, C. F. Beckmann, T. E. Behrens, M. W. Woolrich, and S. M. Smith, "FSL," *Neuroimage*, vol. 62, no. 2, Aug. 2012, doi: 10.1016/j.neuroimage.2011.09.015.
- [81] P. Thévenaz, U. E. Ruttimann, and M. Unser, "A pyramid approach to subpixel registration based on intensity," *IEEE Trans. Image Process.*, vol. 7, no. 1, 1998, doi: 10.1109/83.650848.
- [82] P. Zhou *et al.*, "Efficient and accurate extraction of in vivo calcium signals from microendoscopic video data," Feb. 2018, doi: 10.7554/eLife.28728.
- [83] E. A. Pnevmatikakis, "Analysis pipelines for calcium imaging data," *Curr. Opin. Neurobiol.*, vol. 55, Apr. 2019, doi: 10.1016/j.conb.2018.11.004.
- [84] M. C. Wapler, J. Leupold, I. Dragonu, D. von Elverfeld, M. Zaitsev, and U. Wallrabe, "Magnetic properties of materials for MR engineering, micro-MR and beyond," *J. Magn. Reson.*, vol. 242, May 2014, doi: 10.1016/j.jmr.2014.02.005.
- [85] X. Chen *et al.*, "Sensory evoked fMRI paradigms in awake mice," *Neuroimage*, vol. 204, Jan. 2020, doi: 10.1016/j.neuroimage.2019.116242.
- [86] V. Esmaeili, K. Tamura, G. Foustoukos, A. Oryshchuk, S. Crochet, and C. C. Petersen, "Cortical circuits for transforming whisker sensation into goal-directed licking," *Curr. Opin. Neurobiol.*, vol. 65, Dec. 2020, doi: 10.1016/j.conb.2020.08.003.
- [87] R. Reig and G. Silberberg, "Multisensory Integration in the Mouse Striatum," *Neuron*, vol. 83, no. 5, p. 1200, Sep. 2014.
- [88] B. Zareian, A. Lam, and E. Zagha, "Dorsolateral Striatum is a Bottleneck for Responding to Task-Relevant Stimuli in a Learned Whisker Detection Task in Mice," *J. Neurosci.*, vol. 43, no. 12, Mar. 2023, doi: 10.1523/JNEUROSCI.1506-22.2023.
- [89] H. Zeng, Y. Jiang, S. Beer-Hammer, and X. Yu, "Awake Mouse fMRI and Pupillary Recordings in the Ultra-High Magnetic Field," *Front. Neurosci.*, vol. 16, 2022, doi: 10.3389/fnins.2022.886709.
- [90] I. Ferezou, S. Bolea, and C. C. Petersen, "Visualizing the cortical representation of whisker touch: voltage-sensitive dye imaging in freely moving mice," *Neuron*, vol. 50, no. 4, May 2006, doi: 10.1016/j.neuron.2006.03.043.
- [91] R. Aronoff, F. Matyas, C. Mateo, C. Ciron, B. Schneider, and C. C. Petersen, "Long-range connectivity of mouse primary somatosensory barrel cortex," *Eur. J. Neurosci.*, vol. 31, no. 12, Jun. 2010, doi: 10.1111/j.1460-9568.2010.07264.x.
- [92] T. Yamashita *et al.*, "Diverse Long-Range Axonal Projections of Excitatory Layer 2/3 Neurons in Mouse Barrel Cortex," *Front. Neuroanat.*, vol. 12, 2018, doi: 10.3389/fnana.2018.00033.
- [93] Z. Almási, C. Dávid, M. Witte, and J. F. Staiger, "Distribution Patterns of Three Molecularly Defined Classes of GABAergic Neurons Across Columnar Compartments in Mouse Barrel Cortex," *Front. Neuroanat.*, vol. 13, Apr. 2019, doi: 10.3389/fnana.2019.00045.
- [94] M. J. Nigro, Y. Hashikawa-Yamasaki, and B. Rudy, "Diversity and Connectivity of Layer 5 Somatostatin-Expressing Interneurons in the Mouse Barrel Cortex," *J. Neurosci.*, vol. 38, no. 7, Feb. 2018, doi: 10.1523/JNEUROSCI.2415-17.2017.
- [95] C. F. Ferris, "Applications in Awake Animal Magnetic Resonance Imaging," *Front. Neurosci.*, vol. 16, 2022, doi: 10.3389/fnins.2022.854377.

- 
- [96] A. R. Steiner, F. Rousseau-Blass, A. Schroeter, S. Hartnack, and R. Bettschart-Wolfensberger, "Systematic Review: Anesthetic Protocols and Management as Confounders in Rodent Blood Oxygen Level Dependent Functional Magnetic Resonance Imaging (BOLD fMRI)—Part B: Effects of Anesthetic Agents, Doses and Timing," *Animals : an Open Access Journal from MDPI*, vol. 11, no. 1, Jan. 2021, doi: 10.3390/ani11010199.
- [97] Y. R. Gao *et al.*, "Time to wake up: Studying neurovascular coupling and brain-wide circuit function in the un-anesthetized animal," *Neuroimage*, vol. 153, Jun. 2017, doi: 10.1016/j.neuroimage.2016.11.069.
- [98] K. Yoshida *et al.*, "Physiological effects of a habituation procedure for functional MRI in awake mice using a cryogenic radiofrequency probe," *J. Neurosci. Methods*, vol. 274, Dec. 2016, doi: 10.1016/j.jneumeth.2016.09.013.
- [99] Z. Han *et al.*, "Awake and behaving mouse fMRI during Go/No-Go task," *Neuroimage*, vol. 188, Mar. 2019, doi: 10.1016/j.neuroimage.2019.01.002.
- [100] N. Xu *et al.*, "Functional Connectivity of the Brain Across Rodents and Humans," *Front. Neurosci.*, vol. 16, Mar. 2022, doi: 10.3389/fnins.2022.816331.
- [101] A. Van der Linden and M. Hoehn, "Monitoring Neuronal Network Disturbances of Brain Diseases: A Preclinical MRI Approach in the Rodent Brain," *Front. Cell. Neurosci.*, vol. 15, Jan. 2022, doi: 10.3389/fncel.2021.815552.
- [102] J. R. Polimeni and L. D. Lewis, "Imaging faster neural dynamics with fast fMRI: A need for updated models of the hemodynamic response," *Prog. Neurobiol.*, vol. 207, p. 102174, Dec. 2021.
- [103] L. Kosten, S. A. Emmi, S. Missault, and G. A. Keliris, "Combining magnetic resonance imaging with readout and/or perturbation of neural activity in animal models: Advantages and pitfalls," *Front. Neurosci.*, vol. 16, 2022, doi: 10.3389/fnins.2022.938665.
- [104] T. H. Chao, W. T. Zhang, L. M. Hsu, D. H. Cerri, T. W. Wang, and Y. I. Shih, "Computing hemodynamic response functions from concurrent spectral fiber-photometry and fMRI data," *Neurophotonic*s, vol. 9, no. 3, Jul. 2022, doi: 10.1117/1.NPh.9.3.032205.
- [105] D. A. Handwerker, J. M. Ollinger, and M. D'Esposito, "Variation of BOLD hemodynamic responses across subjects and brain regions and their effects on statistical analyses," *Neuroimage*, vol. 21, no. 4, Apr. 2004, doi: 10.1016/j.neuroimage.2003.11.029.
- [106] C. Iadecola, "The Neurovascular Unit Coming of Age: A Journey through Neurovascular Coupling in Health and Disease," *Neuron*, vol. 96, no. 1, Sep. 2017, doi: 10.1016/j.neuron.2017.07.030.
- [107] S. Schaeffer and C. Iadecola, "Revisiting the neurovascular unit," *Nat. Neurosci.*, vol. 24, no. 9, Sep. 2021, doi: 10.1038/s41593-021-00904-7.
- [108] C. H. Tran and G. R. Gordon, "Acute two-photon imaging of the neurovascular unit in the cortex of active mice," *Front. Cell. Neurosci.*, vol. 9, Feb. 2015, doi: 10.3389/fncel.2015.00011.
- [109] A. Urban *et al.*, "Understanding the neurovascular unit at multiple scales: Advantages and limitations of multi-photon and functional ultrasound imaging," *Adv. Drug Deliv. Rev.*, vol. 119, Sep. 2017, doi: 10.1016/j.addr.2017.07.018.
- [110] H. S. Moon, H. Jiang, T. T. Vo, W. B. Jung, A. L. Vazquez, and S.-G. Kim, "Contribution of Excitatory and Inhibitory Neuronal Activity to BOLD fMRI," *Cereb. Cortex*, vol. 31, no. 9, p. 4053, Sep. 2021.
- [111] K. H. Chuang, Z. Li, H. H. Huang, G. S. Khorasani, and D. Athwal, "Hemodynamic transient and functional connectivity follow structural connectivity and cell type over the brain hierarchy," *Proc. Natl. Acad. Sci. U. S. A.*, vol. 120, no. 5, Jan. 2023, doi: 10.1073/pnas.2202435120.
- [112] A. L. Vazquez, M. Fukuda, and S.-G. Kim, "Inhibitory Neuron Activity Contributions to Hemodynamic Responses and Metabolic Load Examined Using an Inhibitory Optogenetic Mouse Model," *Cereb. Cortex*, vol. 28, no. 11, p. 4105, Nov. 2018.
- [113] Q. Perrenoud *et al.*, "Characterization of Type I and Type II nNOS-Expressing

- Interneurons in the Barrel Cortex of Mouse,” *Front. Neural Circuits*, vol. 6, 2012, doi: 10.3389/fncir.2012.00036.
- [114] I. Yavorska and M. Wehr, “Somatostatin-Expressing Inhibitory Interneurons in Cortical Circuits,” *Front. Neural Circuits*, vol. 10, 2016, doi: 10.3389/fncir.2016.00076.
- [115] S. Sadeh and C. Clopath, “Inhibitory stabilization and cortical computation,” *Nat. Rev. Neurosci.*, vol. 22, no. 1, Jan. 2021, doi: 10.1038/s41583-020-00390-z.
- [116] D. A. Leopold and A. Maier, “Ongoing physiological processes in the cerebral cortex,” *Neuroimage*, vol. 62, no. 4, p. 2190, Oct. 2012.
- [117] A. Mitra *et al.*, “Spontaneous Infra-slow Brain Activity Has Unique Spatiotemporal Dynamics and Laminar Structure,” *Neuron*, vol. 98, no. 2, Apr. 2018, doi: 10.1016/j.neuron.2018.03.015.
- [118] C. Mateo, P. M. Knutsen, P. S. Tsai, A. Y. Shih, and D. Kleinfeld, “Entrainment of Arteriole Vasomotor Fluctuations by Neural Activity Is a Basis of Blood-Oxygenation-Level-Dependent ‘Resting-State’ Connectivity,” *Neuron*, vol. 96, no. 4, Nov. 2017, doi: 10.1016/j.neuron.2017.10.012.
- [119] Y. Ma *et al.*, “Resting-state hemodynamics are spatiotemporally coupled to synchronized and symmetric neural activity in excitatory neurons,” *Proc. Natl. Acad. Sci. U. S. A.*, vol. 113, no. 52, Dec. 2016, doi: 10.1073/pnas.1525369113.
- [120] S. Jaime *et al.*, “Delta Rhythm Orchestrates the Neural Activity Underlying the Resting State BOLD Signal via Phase-amplitude Coupling,” *Cereb. Cortex*, vol. 29, no. 1, Jan. 2019, doi: 10.1093/cercor/bhx310.
- [121] M. J. Brookes *et al.*, “Investigating the electrophysiological basis of resting state networks using magnetoencephalography,” *Proc. Natl. Acad. Sci. U. S. A.*, vol. 108, no. 40, Oct. 2011, doi: 10.1073/pnas.1112685108.
- [122] A. Kucyi, J. Schrouff, S. Bickel, B. L. Foster, J. M. Shine, and J. Parvizi, “Intracranial Electrophysiology Reveals Reproducible Intrinsic Functional Connectivity within Human Brain Networks,” *J. Neurosci.*, vol. 38, no. 17, Apr. 2018, doi: 10.1523/JNEUROSCI.0217-18.2018.
- [123] Y. Adachi *et al.*, “Functional connectivity between anatomically unconnected areas is shaped by collective network-level effects in the macaque cortex,” *Cereb. Cortex*, vol. 22, no. 7, Jul. 2012, doi: 10.1093/cercor/bhr234.
- [124] E. A. Ferenczi *et al.*, “Prefrontal cortical regulation of brainwide circuit dynamics and reward-related behavior,” *Science*, vol. 351, no. 6268, Jan. 2016, doi: 10.1126/science.aac9698.
- [125] J. Turchi *et al.*, “The Basal Forebrain Regulates Global Resting-State fMRI Fluctuations,” *Neuron*, vol. 97, no. 4, Feb. 2018, doi: 10.1016/j.neuron.2018.01.032.
- [126] P. Mächler *et al.*, “A Suite of Neurophotonic Tools to Underpin the Contribution of Internal Brain States in fMRI,” *Current opinion in biomedical engineering*, vol. 18, Jun. 2021, doi: 10.1016/j.cobme.2021.100273.
- [127] D. Zaldivar, A. Rauch, K. Whittingstall, N. K. Logothetis, and J. Goense, “Dopamine-induced dissociation of BOLD and neural activity in macaque visual cortex,” *Curr. Biol.*, vol. 24, no. 23, Dec. 2014, doi: 10.1016/j.cub.2014.10.006.
- [128] S. M. McMahon and M. B. Jackson, “An Inconvenient Truth: Calcium Sensors Are Calcium Buffers,” *Trends Neurosci.*, vol. 41, no. 12, p. 880, Dec. 2018.
- [129] D. Choquet, M. Sainlos, and J. B. Sibarita, “Advanced imaging and labelling methods to decipher brain cell organization and function,” *Nat. Rev. Neurosci.*, vol. 22, no. 4, Apr. 2021, doi: 10.1038/s41583-021-00441-z.
- [130] M. H. Zhu, J. Jang, M. M. Milosevic, and S. D. Antic, “Population imaging discrepancies between a genetically-encoded calcium indicator (GECI) versus a genetically-encoded voltage indicator (GEVI),” *Sci. Rep.*, vol. 11, no. 1, Mar. 2021, doi: 10.1038/s41598-021-84651-6.
- [131] H. H. Yang and F. St-Pierre, “Genetically Encoded Voltage Indicators: Opportunities and

- Challenges," *J. Neurosci.*, vol. 36, no. 39, p. 9977, Sep. 2016.
- [132] Y. Bando, M. Sakamoto, S. Kim, I. Ayzenshtat, and R. Yuste, "Comparative Evaluation of Genetically Encoded Voltage Indicators," *Cell Rep.*, vol. 26, no. 3, Jan. 2019, doi: 10.1016/j.celrep.2018.12.088.
- [133] S. Posse *et al.*, "Enhancement of temporal resolution and BOLD sensitivity in real-time fMRI using multi-slab echo-volumar imaging," *Neuroimage*, vol. 61, no. 1, May 2012, doi: 10.1016/j.neuroimage.2012.02.059.
- [134] L. Wittkuhn and N. W. Schuck, "Dynamics of fMRI patterns reflect sub-second activation sequences and reveal replay in human visual cortex," *Nat. Commun.*, vol. 12, no. 1, Mar. 2021, doi: 10.1038/s41467-021-21970-2.
- [135] H. L. Lee, Z. Li, E. J. Coulson, and K. H. Chuang, "Ultrafast fMRI of the rodent brain using simultaneous multi-slice EPI," *Neuroimage*, vol. 195, Jul. 2019, doi: 10.1016/j.neuroimage.2019.03.045.
- [136] P. T. Toi *et al.*, "In vivo direct imaging of neuronal activity at high temporospatial resolution," *Science*, vol. 378, no. 6616, Oct. 2022, doi: 10.1126/science.abh4340.
- [137] F. Schmid, L. Wachsmuth, F. Albers, M. Schwalm, A. Stroh, and C. Faber, "True and apparent optogenetic BOLD fMRI signals," *Magn. Reson. Med.*, vol. 77, no. 1, Jan. 2017, doi: 10.1002/mrm.26095.
- [138] D. Madularu *et al.*, "A chronic in situ coil system adapted for intracerebral stimulation during MRI in rats," *J. Neurosci. Methods*, vol. 284, Jun. 2017, doi: 10.1016/j.jneumeth.2017.04.018.
- [139] J. Almeida, F. Severo, and D. Nunes, "Impact of the Sound of Magnetic Resonance Imaging Pulse Sequences in Awake Mice," *J. Appl. Anim. Welf. Sci.*, vol. 25, no. 1, Jan. 2022, doi: 10.1080/10888705.2021.1941023.
- [140] J. Paasonen *et al.*, "Multi-band SWIFT enables quiet and artefact-free EEG-fMRI and awake fMRI studies in rat," *Neuroimage*, vol. 206, Feb. 2020, doi: 10.1016/j.neuroimage.2019.116338.
- [141] F. Hennel, "Fast spin echo and fast gradient echo MRI with low acoustic noise," *J. Magn. Reson. Imaging*, vol. 13, no. 6, Jun. 2001, doi: 10.1002/jmri.1138.
- [142] A. Katsunuma, H. Takamori, Y. Sakakura, Y. Hamamura, Y. Ogo, and R. Katayama, "Quiet MRI with novel acoustic noise reduction," *MAGMA*, vol. 13, no. 3, Jan. 2002, doi: 10.1007/BF02678588.
- [143] M. McJury, R. W. Stewart, D. Crawford, and E. Toma, "The use of active noise control (ANC) to reduce acoustic noise generated during MRI scanning: some initial results," *Magn. Reson. Imaging*, vol. 15, no. 3, 1997, doi: 10.1016/s0730-725x(96)00337-2.
- [144] A. S. Tolias *et al.*, "Mapping cortical activity elicited with electrical microstimulation using FMRI in the macaque," *Neuron*, vol. 48, no. 6, Dec. 2005, doi: 10.1016/j.neuron.2005.11.034.
- [145] F. Zhang, A. M. Aravanis, A. Adamantidis, L. de Lecea, and K. Deisseroth, "Circuit-breakers: optical technologies for probing neural signals and systems," *Nat. Rev. Neurosci.*, vol. 8, no. 8, Aug. 2007, doi: 10.1038/nrn2192.
- [146] J. Y. Lin, "A user's guide to channelrhodopsin variants: features, limitations and future developments," *Exp. Physiol.*, vol. 96, no. 1, Jan. 2011, doi: 10.1113/expphysiol.2009.051961.
- [147] W. Yang, L. Carrillo-Reid, Y. Bando, D. S. Peterka, and R. Yuste, "Simultaneous two-photon imaging and two-photon optogenetics of cortical circuits in three dimensions," *Elife*, vol. 7, Feb. 2018, doi: 10.7554/eLife.32671.
- [148] C. Lee, A. Lavoie, J. Liu, S. X. Chen, and B. H. Liu, "Light Up the Brain: The Application of Optogenetics in Cell-Type Specific Dissection of Mouse Brain Circuits," *Front. Neural Circuits*, vol. 14, Apr. 2020, doi: 10.3389/fncir.2020.00018.
- [149] S. E. J. de Vries *et al.*, "A large-scale standardized physiological survey reveals functional organization of the mouse visual cortex," *Nat. Neurosci.*, vol. 23, no. 1, Jan. 2020, doi:

## 70 Bibliography

---

10.1038/s41593-019-0550-9.

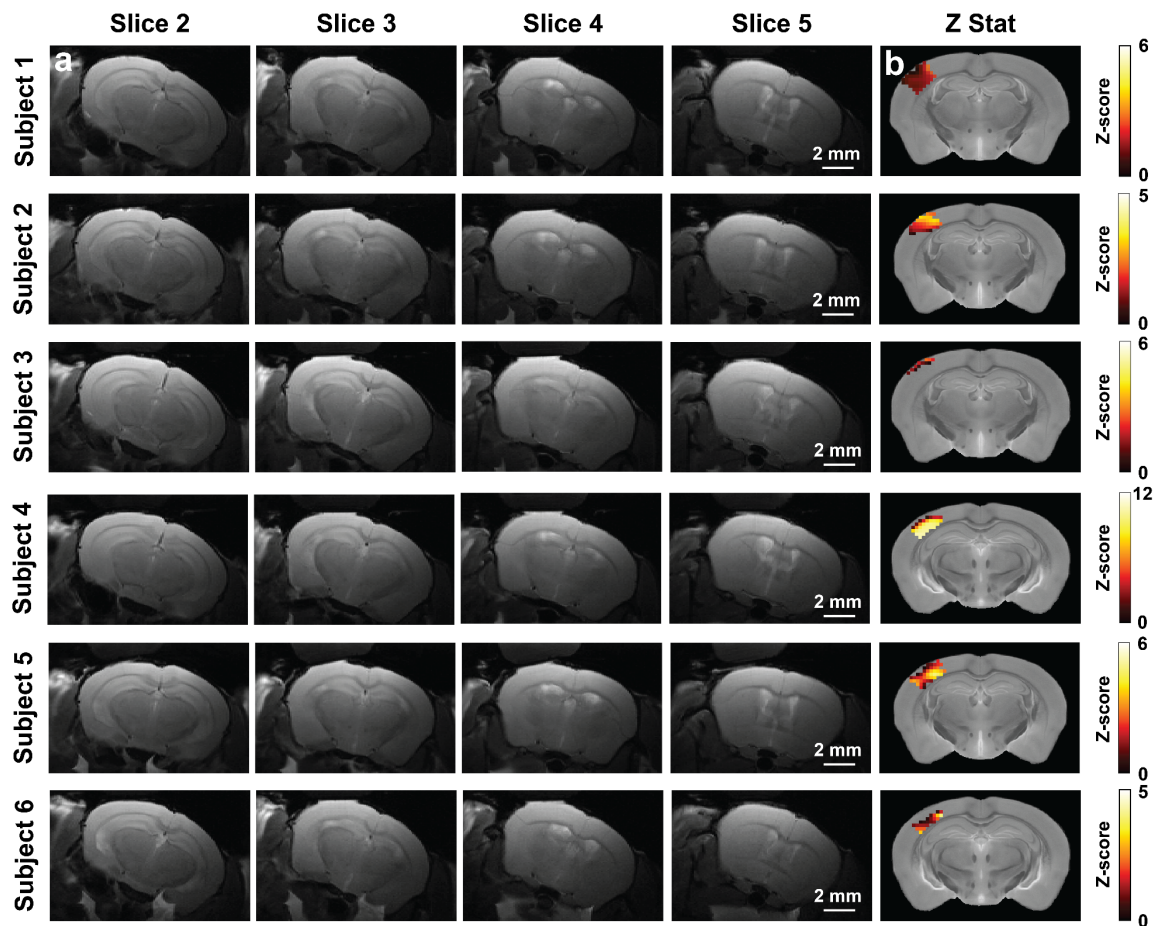


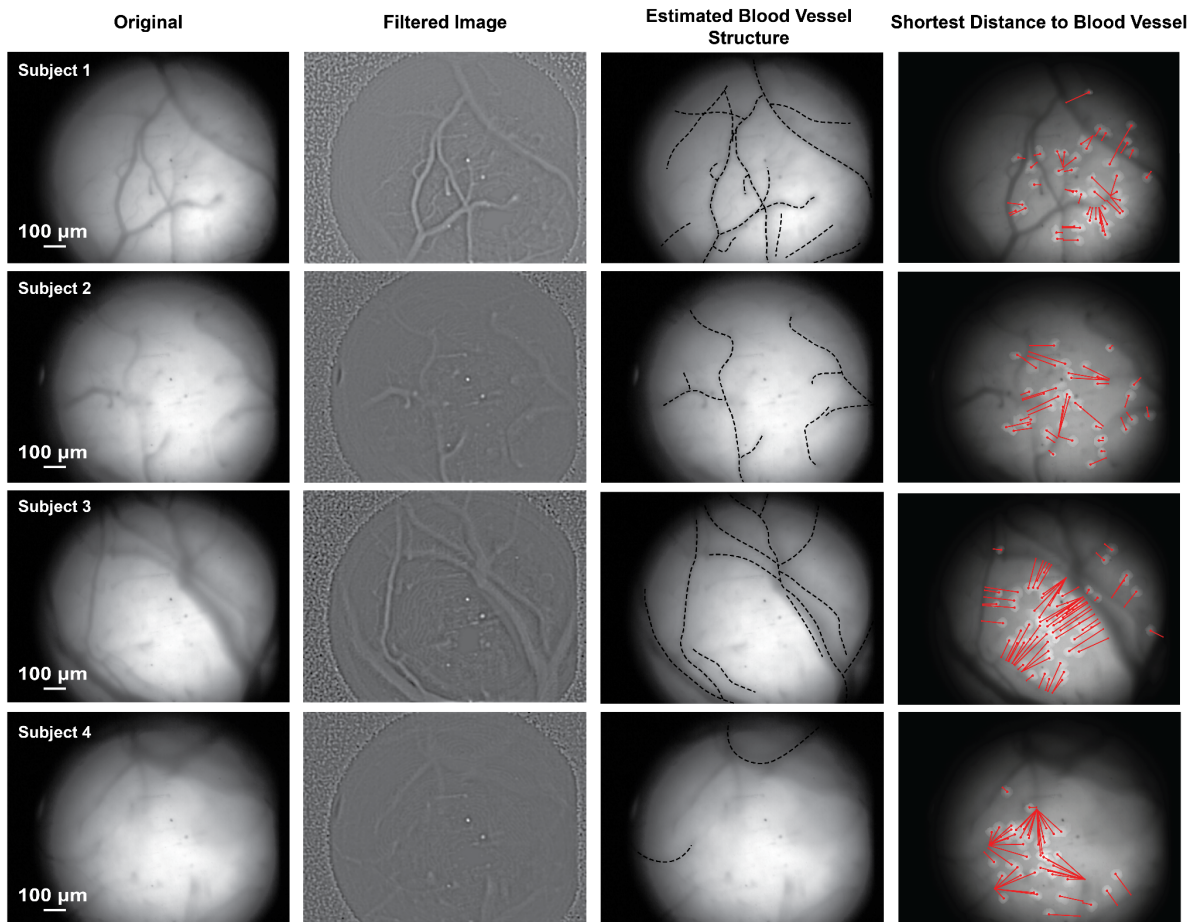
## Chapter 7

## Appendix









**Supplementary figure 2. Annotation of the bloodvessel patterns for individual animals** | The neural-vascular proximity was estimated based on the manual annotation of the vessel structure in the region of interest for each mouse. We used the time-averaged microscopic field (first column) and the band-passed filtered (100-150 Hz) microscopic field (second column) to accurately distinguish the vessel structure (third column). The neural-vascular proximity was calculated as the minimal Euclidean distance between the center of the cell and the vascular structure (fourth column).

# Contributions

## Study conceptualization

- Rik Ubaghs and Benjamin Grewe conceptualized the combined microscopy fMRI study.

## Microscope design

- Optical design was made by Helke Hesse and Rik Ubaghs.
- Camera acquisition code was written by Rik Ubaghs based on the code base from MRC Systems GmbH.
- Mechanical design was made by Rik Ubaghs.
- Parts for the microscope were produced by AMF BIOC, University of Zurich.

## Behavioral setup design

- The MRI cradle and whisker stimulation were designed by Rik Ubaghs.
- Parts for the behavioral setup were produced by D-ITET workshop, ETH Zurich and AMF BIOC, University of Zurich.

## Surgeries

- Surgeries for the behavioral pilot were performed by Rik Ubaghs.
- Surgeries for the combined experiment with L2/3 mice were performed by Rik Ubaghs.
- Surgeries and injections for the inhibitory pilot with Somatostatin positive mice were performed by Roman Boehringer.

## Habituation pilot

- Habituation pilot experiments performed by Rik Ubaghs with support from Roman Boehringer.

## Combined experiment

- Habituation for all experiments was performed by Rik Ubaghs and Roman Boehringer.
- Main experiments were performed by Rik Ubaghs and Roman Boehringer.

## Combined microscopy fMRI analysis

- All data preprocessing and analysis was performed by Rik Ubaghs, except for the calcium imaging preprocessing.
- Calcium imaging preprocessing was performed by Roman Boehringer.

# Curriculum Vitae

## Personal data

Name Rik Lodevicus Elizabeth Maria Ubaghs  
Date of Birth November 08, 1990  
Place of Birth Geleen, The Netherlands  
Citizenship Dutch

## Education

2017 - 2023 Institute of Neuroinformatics  
University of Zürich and ETH Zürich  
Zürich, Switzerland  
*Final degree:* Dr. sc. ETH Zürich

2016 Center for Neuroengineering, Duke University  
Durham, United States  
Visiting student

2015 Swammerdam Institute for Life Sciences  
Amsterdam, The Netherlands  
Internship

2014 - 2016 University of Amsterdam  
Amsterdam, The Netherlands  
*Final degree:* Research M.Sc. Brain and Cognitive Sciences, cum  
Laude  
*Focus:* Cognitive neuroscience, Neuroengineering

2013 Nova Scotia Early Psychosis Unit, Dalhousie University  
Halifax, Canada  
Internship

2011 - 2014 Maastricht University  
Maastricht, The Netherlands  
*Final degree:* B.Sc. Psychology, cum laude  
*Minor:* Neuroscience

## **Publications and conference presentations**

**R. L. E. M. Ubaghs**, R. Böhringer, M. F. Yanik, V. Zerbi, and B. F. Grewe, “Simultaneous single-cell calcium imaging of neuronal population activity and brain-wide BOLD fMRI.,” In prep, 2023.

**R. L. E. M. Ubaghs**, R. Böhringer, V. Zerbi, M. F. Yanik, and B. F. Grewe, “Combined single-cell calcium imaging and function MRI in awake animals,” Society for Neuroscience, 2022.

**R. L. E. M. Ubaghs**, R. Böhringer, M. Marks, M. F. Yanik, and B. F. Grewe, “The Effect of Somatostatin+ Interneurons on the Negative BOLD Response,” The International Society for Magnetic Resonance in Medicine, 2021.

**R. L. E. M. Ubaghs**, H. Dermutz, R. Böhringer, M. Marks, M. F. Yanik, and B. F. Grewe, “Shaping the BOLD signal through Excitatory and Inhibitory Interaction,” The International Society for Magnetic Resonance in Medicine, 2020.



Rik Lodevicus Elizabeth Maria Ubaghs: *Exploring neurovascular coupling through simultaneous functional Magnetic Resonance Imaging and microscopy*, © 2023

doi: 10.3929/ethz-b-000627509